


Università di Camerino, Italy

Università degli Studi di Napoli Federico II, Italy

Université d'Aix-Marseille, France

Faculté des Sciences de Luminy

Ecole doctorale de Physique et Sciences de la Matiére

Centre de Physique Théorique - UMR 7332

Doctoral Thesis

Defended by

**Elham FARAJI**

---

# Quantum transport phenomena in macromolecules

---

Defended on January 31st, 2022, before a jury composed of:

**Prof. Stefano MANCINI**, Scuola di Sceinze e Tecnologie, Università di Camerino, Camerino, Italy. **Thesis Co-Supervisor**

**Prof. Marco PETTINI**, Centre de Physique Théorique, Université d'Aix-Marseille, Marseille, France. **Thesis Co-Supervisor**

**Prof. Jack TUSZYNSKI**, Department of Physics and Department of Oncology, University of Alberta, Edmonton, Canada. **Referee**

**Prof. Philip KURIAN**, Quantum Biology Lab - Howard University, Washington, DC., USA. **Referee**

**Prof. Elena FLORIANI**, Centre de Physique Théorique, Université d'Aix-Marseille, France. **Examiner**

**Prof. Jeremie TORRES**, Institut d'Electronique et des Systmes, Université de Montpellier, France. **Examiner**

**Prof. Roberto PASSANTE**, Physics Department, Università di Palermo, Italy. **Examiner**

**Prof. Cosmo LUPO**, Politecnico di Bari, Italy. **Examiner**

# TABLE OF CONTENTS

# CHAPTER 1. Introduction

Noticeable developments in quantum technologies based on quantum science have been recently done, and these technologies are also expected to bring innovations in biological systems. However, such progress to life science is still in its early days needing more studies in the future [1]. A better understanding of how quantum effects are maintained in living organisms could help researchers to achieve the elusive goal of quantum computation [2]. In the search for relevant quantum effects in living matter, electrons are certainly good candidates for energy transfer, as is confirmed by the studies on the $\pi$-stacks of aromatic rings in proteins. To this end, there are many works studying entanglement, energy and information transmission efficiency such as delocalized electronic transport in photosynthetic process through quantum information processing [3, 4, 5, 6]. Some biological phenomena have also been already ascribed to quantum effects, like in bird orientation, and light response of opsins [7]. The possibility of charge transfer/transport along biomolecules can have relevant biological consequences and has thus motivated several studies [8, 9, 10, 11].

Within this broad field of investigation, this thesis focus on the electronic energy and information transfer along biomolecules and quantum phenomena of electronic currents. More specifically, the investigations reported in this manuscript are aimed to answer a central question concerning the brain/mind activity and molecular dynamics in biological systems that whether in the warm, wet and noisy environment of living matter there are some processes for which quantum phenomena can play a relevant role.

Quantum biophysical discussions arises from fundamental phenomena such as electronic transport and electron transfer described through the dynamics of electrons and phonons, involving bosonic and fermionic modes. There are several possible theoretical frameworks to model exciton propagation on a lattice, where the electron distribution belongs to this class of phenomena. The concept of polaron, a composite particle that consists of an electron and the cloud of phonons bound to it, is useful for understanding the effects of eletron-phonon interaction. According

to this concept, Fröhlich and Holstein systematically have described and studied the polaron in a lattice [12, 13, 14, 15]. In the biological system, as a possible mechanism for energy storage and transport in biomolecules, Davydov has proposed soliton formation and propagation where quantum units of peptide vibrational energy (in particular the amide-I or CO stretching vibration) might become "self-localized" through interactions with lattice phonons [16, 17, 18]. The mathematical techniques that are used to analyze Davydovs soliton are similar to electron-phonon interaction of the Fröhlich and Holstein models. This manuscript could in some senses be considered an attempt to revisit and extend these theoretical models in order to obtain a more realistic explanation of the energy and information transport processes in large molecules. Biological processes in any living organism are based on selective interactions between particular biomolecules. This selectivity of interactions among different biomolecules such as DNA, RNA and proteins maintain cell functions. This raises the question of what is the physical nature of these interactions bringing the various actors of complex biochemical processes in the right place, at the right time and in the right order so as to ensure the essential cellular functions. Since the end of the 60's, Herbert Fröhlich surmised theoretically that quantum electrodynamic long range interactions are possible in biochemical reactions; while other interactions (chemical bonds, hydrogen bonds, dispersive and Van der Waals interactions) are short range acting at a distance of the order of few Angstroms influenced by Debye screening. The possibility of long range electrodynamic interactions (EDIs) in a long distance only happens among resonant oscillators in the frequency range $0.1 - 1$ THz and out-of-thermal equilibrium situation known as Fröhlich condensation phenomenon [19, 20]. These results have been recently revisited within the framework of classical electrodynamics, too [21, 22].

The new mathematical approach Resonant Recognition Model (RRM) interprets protein sequence linear information based on the Fourier transform and physical characteristics of amino acids or nucleotides along an enzyme or a DNA, respectively. This physico-mathematical method of RRM act as a cross-spectral function of the spectra of electronic currents involved in the biochemical reactions and predict a selectivity of the interactions by a sharp peak frequency of the cross spectrum, but it is unable to explain the physical nature behind it.

We start this manuscript by studying quantum information transport in macromolecules. Quantum information and quantum communication are built upon the quantum bit, or qubit for short, and study the capabilities of transferring quantum states from one place to another. It

is very important to have physical systems, biomolecules in our work described by a spin chain which can serve as channels for quantum communication. The model we have used for the spin chain is the Davydov model in its elementary version (without environment/phonons) and we study it as a preliminary step. The state to be transmitted is placed on one spin of the chain and received later on a distant spin with some fidelity. The probability of perfectly transfer of a quantum state in such a spin chain is investigated. Then we move on a more realistic Davydov and Fölich-Holstein model including environment/phonons. In [23], we addressed the problem of the energy downconversion of the light absorbed by a protein into its internal vibrational modes (phonons). Starting with a generalization of the Davydov's model by considering a non-linear electron-electron coupling energy and phonon-phonon interacting parameter, we use the Time Dependent Variational Principle (TDVP) to work out the dynamical equations of the system. We considered the case in which the light receptors are fluorophores either naturally co-expressed with the protein or artificially covalently bound to some of its amino acids. In a recent work [21], it was experimentally found that by shining a laser light on the fluorophores attached to a protein the energy fed to it could be channeled into the normal mode of lowest frequency of vibration thus making the subunits of the protein coherently oscillate. Even if the phonon condensation phenomenon was theoretically explained, the first step - the energy transfer from electronic excitation into phonon excitation - has been left open. The work [23] is aimed at filling this gap.

In [24], we also studied the motion of an electron along a chain of heavy particles modeling a sequence of nucleotides proper to a DNA fragment. Supposing the site-dependent electron tunneling term and electron-phonon coupling constants whose sequence of values reflects the sequence of nucleotides. It could be found that, under the action of an external source of energy transferred to the electron, and according to the excitation site, the electron current can display either a broad frequency spectrum or a sharply peaked frequency spectrum. This sequence-dependent charge transfer phenomenology is suggestive of a potentially rich variety of electrodynamic interactions of DNA molecules under the action of electron excitation. This could imply the activation of interactions between DNA and transcription factors, or between DNA and external electromagnetic fields.

Finally, we described the electron current along a DNA and a protein, separately. The electrons move back and forth, and the associated currents have nontrivial frequency spectra. It turns out

that, for suitable excitation conditions, the cross spectra of the electron currents flowing along the EcoRI restriction enzyme [1] and along a DNA fragment- carrying the cleavage sequence for EcoRI - are sharply peaked. Independently, we obtained surprisingly a similar result by applying digital RRM of DNA and EcoRI sequences, though the RRM does not make any difference according to the initial electron excitation energy and position. Consequently, theses outcomes could active selective attractive forces between selected sites of a DNA sequence and a EcoRI enzyme and be a propaedeutic step to understanding how external EMFs can stop mitosis of the cancer cells.

**Organization of the manuscript**

- Chapter 2 is a review chapter where the main theoretical background of the ongoing research "electron-phonon interactions" is presented, in particular, Davydov's soliton is reviewed. Moreover, we introduce TDVP to derive the dynamical equations of a quantum Hamiltonian system.

- Chapter 3 Quantum maps and some classes of qubit channels are presented. Then Quantum information transfer through the simplified Davydov's Hamiltonian (without environment) for a spin network of, separately, two atoms and $N$ atoms is reported.

- Chapter 4 deals with the research concerning the long-range electrodynamic interactions among biomolecules by reviewing a theoretical background of Fröhlich condensation and derivation of its rate equations. We discuss also physico-mathematical RRM describing the selectivity of intermolecular interactions in biological systems.

- Chapter 5 reports energy transfer to the phonons of a macromolecule through light pumping. This finding provides a logic behind phonon condensation phenomenon in a macromolecule.

- Chapter 6 The possibility of creating a coherent or random electron sequence-dependent currents on a DNA Chain is presented. The outcome suggests rich variety of electrodynamic interactions between the DNA and specific targets.

[1] EcoRI (pronounced "eco R one") is a restriction endonuclease enzyme isolated from species E. coli. The "Eco" part of the enzyme's name originates from the species from which it was isolated- "E" denotes generic name which is "Escherichia" and "co" denotes species name, "coli" - while the R represents the particular strain and the I denotes that it was the first enzyme isolated from this strain.

- Chapter 7 The investigation of how the partners of the biochemical reaction can be put accelerated by co-resonance phenomenon already suggested by RRM is reported. This includes the study of interaction between DNA and EcoRI enzyme by using cross frequency spectrum of the site-dependent currents flowing on them.

The results discussed in this thesis led to the following publications:

- E. Faraji, R. Franzosi, S. Mancini and M. Pettini, *Energy transfer to the phonons of a macromolecule through light pumping*, Scientific Reports **11**, 1-14 (2021).
- E. Faraji, R. Franzosi, S. Mancini and M. Pettini, *Transition between random and periodic electron currents on a DNA chain*, Int. J. Mol. Sci. **22**, 7361 (2021).
- E. Faraji, S. Mancini, A. Nourmandipour, M. Pettini and R. Franzosi, *Quantum information transport on a biomolecule*, In preparation.
- E. Faraji, P. Kurian, R. Franzosi, S. Mancini, I. Cosic, D. Cosic and M. Pettini, *Electrodynamic forces driving DNA-enzyme interaction at a large distance*, In preparation.

# CHAPTER 2. Preliminaries

This chapter starts with the quantum preliminaries, then it goes through the main framework of this work by describing polaron quasiparticle and Davydov and Fröhlich-Holstein models introducing electron-phonon interactions. Moreover, the time dependent variational principle (TDVP) is introduced which is a new approach to derive the dynamical equations of a quantum Hamiltonian system.

## 2.1 Quantum formalism

The standard Dirac notation $|\rangle$ is introduced for vector states in quantum mechanics. Generic quantum states are described with an ensemble of state vectors which is written as $\{|x\rangle, p(x)\}$ or more generally by a density operator $\hat{\rho} = \sum_x p_x |\psi_x\rangle\langle\psi_x|$ with $|\psi_x\rangle$ in a Hilbert space $H$, $p_x > 0$, and $\sum_x p_x = 1$. The quantum density operator is Hermitian $\hat{\rho} = \hat{\rho}^\dagger$, non-negative $\hat{\rho} > 0$ and unit-trace $Tr(\hat{\rho}) = 1$. A quantum state is pure when it is perfectly known in a given quantum system or equivalently when $\hat{\rho} = \hat{\rho}^2$. Otherwise, it is called a mixed state. Let us suppose that at initial time $t_0 = 0$, the density operator is given by $\hat{\rho}(0) = \sum_x p_x(0)|\psi_x(0)\rangle\langle\psi_x(0)|$. If the quantum system is to be left undisturbed, the time evaluation of $\rho$ is given by

$$\frac{d}{dt}\hat{\rho}(t) = \mathcal{L}\hat{\rho}(t), \tag{2.1}$$

where

$$\mathcal{L}\hat{\rho} = -i[\hat{H}, \hat{\rho}]. \tag{2.2}$$

$\mathcal{L}$ is usually called Liouvillian superoperator, whose name comes from the fact that it acts on operators to give operators. Clearly, we can write

$$\hat{\rho}(t) = \hat{U}(t)\hat{\rho}(0)\hat{U}^\dagger(t), \tag{2.3}$$

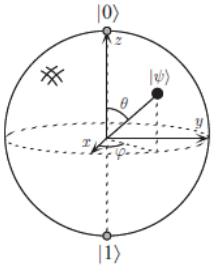


Figure 2.1 Bloch sphere representation of a qubit.

with the unitary evolution operator $\hat{U}(t) = e^{-i\hat{H}t}$.

### 2.1.1 Quantum bits

A Quantum bit or qubit is a two-state (or two-level) quantum-mechanical system, one of the simplest quantum systems displaying the peculiarity of quantum mechanics. Two possible states for a qubit are $|0\rangle$ and $|1\rangle$ as the most basic piece of information in quantum computation and quantum information. An example is the spin of the electron in which the two levels can be taken as spin up and spin down. The main distinction between classical and quantum bit is that the latter can be also in a linear combinations of the states $|0\rangle$ and $|1\rangle$ called superposition [25]:

$$|\psi\rangle = \alpha|0\rangle + \beta|1\rangle \tag{2.4}$$

where $\alpha$ and $\beta$ are complex numbers. The special states $|0\rangle$ and $|1\rangle$ are known as computational basis states, and form an orthonormal basis for the vector space $C^2$. Naturally, $|\alpha|^2+|\beta|^2 = 1$, since the probabilities must sum to one. Thus, in general a qubits state is a unit vector in a two-dimensional complex vector space and we may rewrite $|\psi\rangle$ as

$$|\psi\rangle = \cos\frac{\theta}{2}|0\rangle + e^{i\phi}\sin\frac{\theta}{2}|1\rangle \tag{2.5}$$

The numbers $\theta$ and $\phi$ define a point on the unit three-dimensional sphere, as shown in Fig. 6.7. This sphere is often called the Bloch sphere providing a useful means for visualizing the state of a single qubit, and often serves as an excellent testbed for ideas about quantum computation and quantum information.

If we have more than one qubit in our quantum system, we can express it in terms of product

states. For example, a two-qubit system has the basis states, $|00\rangle$, $|01\rangle$, $|10\rangle$, $|11\rangle$, which unlike classical bits, two or more qubits can interfere with one another, creating a macroscopically coherent superposition, of the form $C_{00}|00\rangle + C_{01}|01\rangle + C_{10}|10\rangle + C_{11}|11\rangle$. More generally, $n$ qubits will have $2^n$ product states or dimensions, in their Hilbert space forming the computational basis of an n-qubit quantum computer.

### 2.1.2 Quantum fidelity

fidelity is a measure of the "closeness" of two quantum states. It expresses the probability that one state will pass a test to identify as the other. Given two density operators $\rho$ and $\sigma$, the fidelity is generally defined as the quantity [25]

$$F(\rho,\sigma) = Tr\Big(\sqrt{\sqrt{\rho}\sigma\sqrt{\rho}}\Big). \tag{2.6}$$

Let us suppose $[\rho,\sigma] = 0$ which means they can be diagonalized in the same basis. Then considering $\rho = |\psi\rangle\langle\psi|$ as a pure state and $\sigma$ as an arbitrary state, the fidelity from Eq. (2.6) reads

$$\begin{aligned} F(|\psi\rangle\langle\psi|,\sigma) &= Tr\Big(\sqrt{(|\psi\rangle\langle\psi|)^{1/2}\sigma(|\psi\rangle\langle\psi|)^{1/2}}\Big) \\ &= \sqrt{\langle\psi|\sigma|\psi\rangle}Tr(|\psi\rangle\langle\psi|) = \sqrt{\langle\psi|\sigma|\psi\rangle}, \end{aligned} \tag{2.7}$$

where we used the fact that $(|\psi\rangle\langle\psi|)^{1/2} = |\psi\rangle\langle\psi|$ because $\rho$ is pure. If both $\rho$ and $\sigma$ are pure, $\sigma = |\phi\rangle\langle\phi|$, then Eq. (2.7) results in

$$F(\rho,\sigma) = \sqrt{\langle\psi|\phi\rangle\langle\phi|\psi\rangle} = |\langle\psi|\phi\rangle|. \tag{2.8}$$

So, the fidelity is equal to the overlap between $|\psi\rangle$ and $|\phi\rangle$.

## 2.2 Polaron mobility and Davydov's soliton

Excitation energy transfer phenomenon in biological systems are problems attracted a lot of attentions during the last years. In this context, understanding the mechanism of electron transfer (ET) in proteins is a long-standing interest. In fact, physiological conditions as well as the molecular dynamics simulations have predicted that the vibrational dynamics of proteins

may serve as the driving force of ET in proteins [26]. Lev Landau in 1933 [27] and Solomon Pekar in 1946 [28] proposed a concept of polaron as a quasiparticle to understand the interactions between electrons and atoms in a solid material. A polaron is an entity consisting of an electron and the cloud of phonons bound[1]. If phonon frequencies are sufficiently low, the local deformation of ions, caused by electron itself, creates a potential well which traps the electron. The different polaron types are needed to describe the effects of electron-phonon interaction in real materials in which band structure, as well as the strength and range of the interaction, can vary to a great degree. There are some similar mathematical techniques have been developed for the polaron effects suggested by Fröhlich [12, 13], Holstein [14, 15] and Davydov [16, 17, 18]. Here, we briefly pay our attention to the Fröhlich and Holstein models and then we go to the details of the Davydov's soliton.

### 2.2.1 Fröhlich and Holstein Hamiltonians

As we already mentioned, the displacement (vibrations) of atoms of a lattice from their equilibrium positions screen the charge of the electron moving along it. In the polar medium, according to the dielectric theory, a polaron may be formed at low temperature when the electron in motion induces polarization around itself and in turn it may become self-trapped by the field of induced polarization. Fröhlich is the first one who systematically described and studied the polaron. In his model, he used continuum approximation meaning that the free electron interacts with the dielectric polarizable continuum. In this case, the size of the self-trapped state is large compared with the lattice constant $a$ and the polaron extends over many constants so that the discreteness of the lattice is neglected. Therefore, the long range electron-phonon interaction is derived. The Hamiltonian of this model is

$$\hat{H}_{\text{Fröhlich}} = \frac{\mathbf{p}^2}{2m} + \sum_{\mathbf{k}}^{N} \hbar\omega_0 \hat{\zeta}_{\mathbf{k}}^{\dagger}\hat{\zeta}_{\mathbf{k}} + \sum_{\mathbf{k}}^{N} (V_{\mathbf{k}}\hat{\zeta}_{\mathbf{k}} e^{i\mathbf{k}.\mathbf{r}} + V_{\mathbf{k}}^{*}\hat{\zeta}_{\mathbf{k}}^{\dagger} e^{-i\mathbf{k}.\mathbf{r}}), \tag{2.9}$$

where

$$V_{\mathbf{k}} = -i\frac{\hbar\omega_0}{k}\left(\frac{4\pi\alpha}{V}\right)^{1/2}\left(\frac{\hbar}{2m\omega_0}\right)^{1/4} \tag{2.10}$$

[1] A phonon is referred to a quasiparticle which is an excited state of the vibrational modes for elastic structures of particles in a lattice. Classically, phonon or normal mode is the Fourier transform of the contribution of all the localized atoms or molecules in a lattice [29]

and

$$\alpha = \frac{e^2}{\hbar}\sqrt{\frac{m}{2\hbar\omega_0}}(\frac{1}{\epsilon_\infty} - \frac{1}{\epsilon_0}), \tag{2.11}$$

in which the zero-point energy $\sum_{\mathbf{k}} \hbar\omega_0/2$ is neglected. Here, $\mathbf{r}$ and $\mathbf{p}$ are the position and momentum operators of electron, $m$ is the effective mass of electron (as determined by its interaction with the periodic lattice potentials), $\mathbf{k}$ is the momentum operator of the $k$-th phonon, $\omega_0$ is the constant frequency of all $N$ longitudinal vibrational modes of the lattice (phonons), $\hat{\zeta}_{\mathbf{k}}$ and $\hat{\zeta}^\dagger_{\mathbf{k}}$ are the phonon annihilation and creation operators and $V$ is the volume of the medium. The $\alpha$ is the dimensionless electron-phonon coupling constant, while $\epsilon_0$ is the static and $\epsilon_\infty$ is the high-frequency dielectric constants of the material. It is obvious that the strength of the interaction in Fröhlich Hamiltonian is dependent on the measurable features of the medium such as the dielectric constants, phonon frequencies, and effective mass of electron. The strong coupling gives $\alpha \gg 1$.

Moreover, there is another form of polaron when the interaction of a single electron with molecular vibrations may be strong known well as Holstein model. It means that the electron coupled to the displacements of the lattice sites. In comparison with the Fröhlich model, Holstein Hamiltonian is generally an approximation for the short electron-phonon interaction ranges in (non-polar) materials. In this case, there may be small or large polarons, depending on the lattice constant $a$. Standard Holstein Hamiltonian is given by the tight-binding approximation [2] for the electron as

$$\hat{H}_{Holstein} = -J\sum_{i}^{N} \hat{\beta}_i^\dagger \hat{\beta}_{i+1} + \hbar\omega_0 \sum_{i}^{N}(\frac{1}{2} + \hat{\zeta}_i^\dagger \hat{\zeta}_i) - g\sum_{i}^{N} \hat{\beta}_i^\dagger \hat{\beta}_i(\hat{\zeta}_i^\dagger + \hat{\zeta}_i). \tag{2.12}$$

Here, $\hat{\beta}_i$ and $\hat{\beta}_i^\dagger$ are the destruction and creation operators for the electron at any site (molecule) $i(i = 1, 2, ..., N)$ and the constant $J$ is the nearest neighbor coupling energy of the electron tunneling across two neighboring molecules. $\hat{\zeta}_i$ and $\hat{\zeta}_i^\dagger$ are the phononic lowering and rising operators and $\omega_0$ is the constant frequency of phonons. Finally, $g$ is the electron-phonon coupling parameter. It is also common that the Holstein Hamiltonian to be written in terms of the phononic position and momentum operators $\hat{x}_i$ and $\hat{p}_i$ for longitudinal displacements of molecules at site

[2] The electrons are tightly bound to the atom to which they belong and they have limited interaction with states and potentials on surrounding atoms of the lattice.

$i$, such that

$$\begin{aligned}\hat{\zeta}_i &= \frac{1}{\sqrt{2}}\left[\left(\frac{M\omega_0}{\hbar}\right)^{1/2}\hat{x}_i + \mathrm{i}\left(\frac{1}{\hbar M\omega_0}\right)^{1/2}\hat{y}_i\right], \\ \hat{\zeta}_i^{\dagger} &= \frac{1}{\sqrt{2}}\left[\left(\frac{M\omega_0}{\hbar}\right)^{1/2}\hat{x}_i - \mathrm{i}\left(\frac{1}{\hbar M\omega_0}\right)^{1/2}\hat{y}_i\right]. \end{aligned} \tag{2.13}$$

Here $M$ is the mass of molecule vibrating with the frequency $\omega_0$ and $n_i = \hat{\beta}_i^{\dagger}\hat{\beta}_i$ is the electron density. Clearly, $[\hat{\zeta}_i, \hat{\zeta}_j^{\dagger}] = \delta_{ij}$. Then

$$\begin{aligned}\hat{H}_{Holstein} &= -J\sum_i^N(\hat{\beta}_i^{\dagger}\hat{\beta}_{i+1} + H.c) \\ &+ \sum_i^N \frac{1}{2}(M\omega_0^2\hat{x}_i^2 + \frac{\hat{p}_i^2}{M}) - \chi\sum_i^N \hat{n}_i\hat{x}_i, \end{aligned} \tag{2.14}$$

where $\chi = \left(\frac{2M\omega_0 g^2}{\hbar}\right)^{1/2}$.

### 2.2.2 Davydov's soliton

In 1973, Davydov applied the concept of molecular solitons in order to explain the mechanism of muscle contraction in animals [30]. He proposed a mechanism for the localization and transport of vibrational energy in protein $\alpha$-helix represented as a system of three one-dimensional chains of springs coupled with each other . Each chain is composed by two types of harmonic oscillators, hydrogen bonds and the backbone $C = O$ group [17, 18]. See Figs. (2.2) and (2.3).

Generally, the term polaron has been used to denote a wide variety of excitations (called excitons) that are self-localized through interactions with lattice phonons. A polaron can be also seen in an alpha-helix when the electron oscillation energy of the double bound $CO$ stretching (or Amide-I) localized on the helix interacts with the lattice phonons in order to distort the structure of the helix. In a reaction, the helical distortion again through phonon coupling traps the Amide-I vibrational energy and avoids its dispersion. This phenomenon is self-localizing or self-trapping [17, 31].

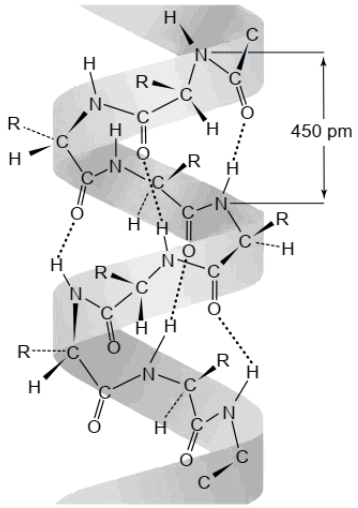


Figure 2.2 Molecular structure of an $\alpha$-helix which is a secondary structure of protein (one of the four distinct aspects of a protein's structure) in which every backbone $N-H$ group couples to the double bound backbone $C=O$ group of the amino acid by the hydrogen bonds. Hydrogen bonds are represented by dashed lines. Figure adapted by [32].

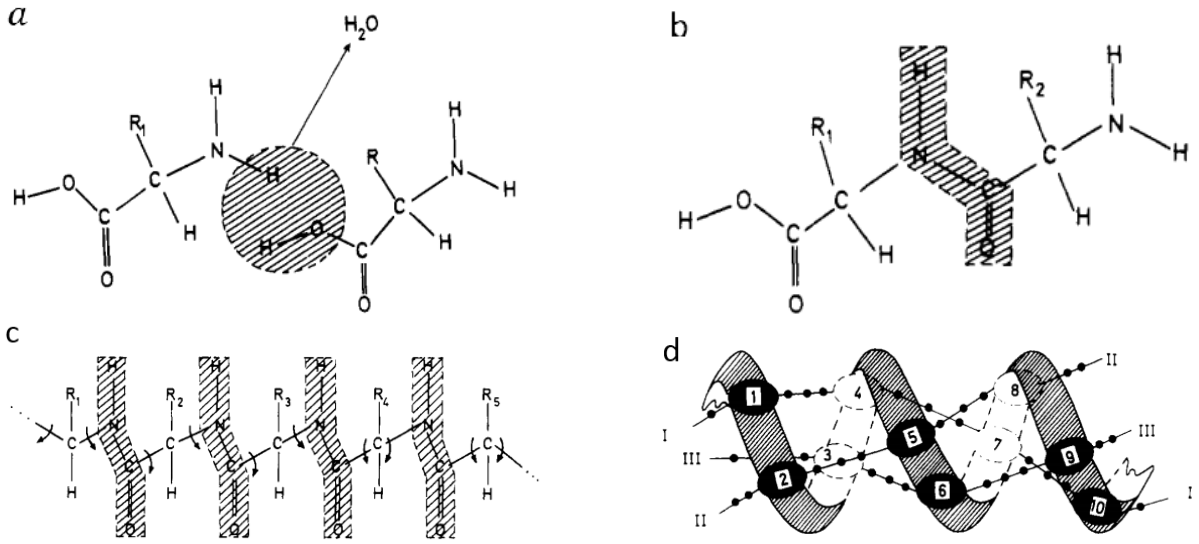


Figure 2.3 Proteins comprise one or more long chains of amino acid residues called polypeptide(s). A protein contains at least one long polypeptide. Amino acids are organic compounds containing amino ($NH_3^+$) and carboxylate ($CO_2^-$) functional groups, along with a side chain ($R$ group) specific to each amino acid. a) The formation of the peptide bonding between two amino acids, b) the dimer which is formed from two amino acid molecules, c) the repeated peptide groups in a protein molecule, and d) three chains of peptide groups (I,II,III) in a protein molecule; the peptide groups are specified by the numbers $1, 2, ..., 10$ which are linked by the hydrogen bonds denoted by three dots. Figure adapted by [17].

A soliton or solitary wave is a self-reinforcing wave packet maintaining its shape while it is propagating at a constant velocity. Davydov's soliton is a type of a large acoustic polaron at low temperature and in the continuum approximation [3] where the self-localization is created from coupling with the acoustic modes of the lattice ( the long-wavelength phonons give rise to sound). Also, in the Davydov model the anharmonic coupling energy is considered small compared with the phonon bandwidth. Referring to the chain structure of each $\alpha$-helix spine in Fig. (2.4), $J = 9.67 \times 10^{-4}$ eV is the interaction energy between two consecutive $C = O$ groups, and $\chi = 35 - 62$ pN is the nonlinear coupling between the excited $C = O$ group and the distortion of the adjacent hydrogen bonds [18].

[3] The size of the self-trapped state is large compared with the lattice constant $a$ and the polaron extends over many constants so that the discreteness of the lattice is neglected.

Hamiltonian for the Davydovs model is given by [18]

$$\hat{H} = \hat{H}_{ex} + \hat{H}_{ph} + \hat{H}_{int}, \tag{2.15}$$

where the first term $\hat{H}_{ex}$ is the exciton energy operator

$$\begin{aligned} \hat{H}_{ex} &= \sum_{n=1}^{N}\sum_{\alpha=1}^{3}\Big[E_0\hat{B}^{\dagger}_{n,\alpha}\hat{B}_{n,\alpha} - J\left(\hat{B}^{\dagger}_{n,\alpha}\hat{B}_{n+1,\alpha} + \hat{B}^{\dagger}_{n,\alpha}\hat{B}_{n-1,\alpha}\right) \\ &+ L\left(\hat{B}^{\dagger}_{n,\alpha}\hat{B}_{n,\alpha+1} + \hat{B}^{\dagger}_{n,\alpha}\hat{B}_{n,\alpha-1}\right)\Big]. \end{aligned} \tag{2.16}$$

Here, $E_0 = 0.2$ eV is the energy of the amide-I vibration (CO stretching) and $\hat{B}_{n,\alpha}$ and $\hat{B}^{\dagger}_{n,\alpha}$ are the annihilation and creation operators for the stretching $C = O$ oscillators. The subscript $n$ labels the molecule along a chain $n = 1, 2, ..., N$, while the subscript $\alpha(= 1, 2, 3)$ specifies a particular channel. Thus the pair $(n, \alpha)$ chooses an individual amino acid. Furthermore, $L = 1.53 \times 10^{-3}$ eV is the nearest neighbor dipole-dipole coupling energy between channels.

$$\cdots H - N - C \underbrace{= O \cdots H - N - C}_{J} = \underbrace{O \cdots H}_{\chi} - N - C = O \cdots$$

Figure 2.4 The structure of three channels running along the $\alpha$-helix.

The second term $\hat{H}_{ph}$ in (2.15) is the phonon energy operator

$$\hat{H}_{ph} = \frac{1}{2}\sum_{n,\alpha}\Big[\frac{\hat{p}^2_{n,\alpha}}{M} + \Omega(\hat{u}_{n+1,\alpha} - \hat{u}_{n,\alpha})^2\Big], \tag{2.17}$$

where $\hat{p}_{n,\alpha}$ and $\hat{u}_{n,\alpha}$ are momentum and position operators for longitudinal displacements of amino acids at site $n$, respectively with mass $M$ and $\Omega = 13 - 19.5$ N/m is the spring constants of hydrogen bonds (two nerboring amino acids), respectively. Finally, the third term $\hat{H}_{int}$ in (2.15) is the exciton-phonon interaction operator

$$\hat{H}_{int} = \sum_{n,\alpha}\chi(\hat{u}_{n+1,\alpha} - \hat{u}_{n,\alpha})\hat{B}^{\dagger}_{n,\alpha}\hat{B}_{n,\alpha}. \tag{2.18}$$

Davydovs analysis of the model Hamiltonian (2.15) is based on factorizing for the state vector of the system as

$$|\psi\rangle = |\Psi\rangle|\Phi\rangle \tag{2.19}$$

in which $|\Psi\rangle$ describes a single quantum excitation of exciton

$$|\Psi(t)\rangle = \sum_{n,\alpha} C_{n,\alpha}(t)\hat{B}^{\dagger}_{n,\alpha}|0\rangle_{ex}, \tag{2.20}$$

where $|0\rangle_{ex}$ is the vacuum state of the $C = O$ oscillators, and $|\Phi\rangle$ is a coherent phonon state. Then the expectation values for $\hat{u}_n$ and $\hat{p}_n$ are found to be

$$\begin{aligned} \langle\Phi|\hat{u}_{n,\alpha}|\Phi\rangle &= \beta_{n,\alpha}(t), \\ \langle\Phi|\hat{p}_{n,\alpha}|\Phi\rangle &= \pi_{n,\alpha}(t), \end{aligned} \tag{2.21}$$

where $\beta_{n,\alpha}(t)$ and $\pi_{n,\alpha}(t)$ are the average values of the longitudinal displacement and momentum of an amino acid, respectively.

The equations of motion by calculating

$$\langle\psi(t)|\hat{H}|\psi(t)\rangle = H(C_{n,\alpha}, C^{*}_{n,\alpha}, \beta_{n,\alpha}, \pi_{n,\alpha}) \tag{2.22}$$

and solving Shrödinger equation are given by

$$\begin{aligned} i\hbar\dot{C}_{n,\alpha} &= \Big(E_0 + W + \chi(\beta_{n+1,\alpha} - \beta_{n,\alpha})\Big)C_{n,\alpha} \\ &- J(C_{n+1,,\alpha} + C_{n-1,,\alpha}) + L(C_{n,\alpha+1} + C_{n,\alpha-1}), \\ M\ddot{\beta}_{n,\alpha} &= \Omega(\beta_{n+1,\alpha} - 2\beta_{n,\alpha} + \beta_{n-1,\alpha}) + \chi\Big(|C_{n,\alpha}|^2 - |C_{n-1,\alpha}|^2\Big) \end{aligned} \tag{2.23}$$

where

$$W = \frac{1}{2}\sum_{n,\alpha}\Big[M\dot{\beta}^2_{n,\alpha} + \Omega(\beta_{n+1,\alpha} - \beta_{n,\alpha})^2\Big] \tag{2.24}$$

is the total phonon energy. According to the normalization condition $\langle\psi|\psi\rangle = \sum_{n,\alpha}|C_{n,\alpha}| = 1$, and by assuming the situation in which $C_{n,1} = C_{n,2} = C_{n,3}$ for the Amid-I oscillators, it is convenient to consider $C_n = \sqrt{3}C_{n,\alpha}$ and $\beta_{n,\alpha} = \beta_n$ so that the equations (2.23) and (2.24) are

written as

$$\begin{aligned} i\hbar\dot{C}_n &= \Big(E_0 + W + \chi(\beta_{n+1} - \beta_n) + 2L\Big)C_n \\ &- J(C_{n+1} + C_{n-1,}), \\ 3M\ddot{\beta}_n &= 3\Omega(\beta_{n+1} - 2\beta_n + \beta_{n-1}) + \chi\Big(|C_n|^2 - |C_{n-1}|^2\Big), \end{aligned} \tag{2.25}$$

where

$$W = \frac{1}{2}\sum_n \Big[3M\dot{\beta}_n^2 + 3\Omega(\beta_{n+1} - \beta_n)^2\Big]. \tag{2.26}$$

By considering a gauge transformation

$$C_n = \phi_n \exp(-it(E_0 + W + 2L - 2J)/\hbar), \tag{2.27}$$

the equations (2.25) leads to the form

$$\begin{aligned} i\hbar\dot{\phi}_n &= \chi(\beta_{n+1} - \beta_n)\phi_n - J(\phi_{n+1} - 2\phi_n + \phi_{n-1,}), \\ 3M\ddot{\beta}_n &= 3\Omega(\beta_{n+1} - 2\beta_n + \beta_{n-1}) + \chi\Big(|\phi_n|^2 - |\phi_{n-1}|^2\Big). \end{aligned} \tag{2.28}$$

Assuming a stationary solution $\dot{\beta}_n = 0$, firstly, gives

$$\beta_{n+1} - \beta_n = -(\chi/3\Omega)|\phi_n|^2, \tag{2.29}$$

then following nonlinear Shrödinger equation is obtained

$$i(\hbar/J)\dot{\phi}_n + (\phi_{n+1} - 2\phi_n + \phi_{n-1}) + \sigma_0^{-1}|\phi_n|^2\phi_n = 0, \tag{2.30}$$

where $\sigma_0 = 3\Omega J/\chi^2$. Consequently, regarding to gauge transformation (2.27) an approximate stationary solution located at $n = n_0$ for (2.28) for the equations for $\sigma_0 \gg 1$ and $N \gg 1$ is

$$|\phi_n|^2 = \frac{1}{8\sigma_0}\mathrm{sech}^2\left(\frac{n - n_0}{4\sigma_0}\right). \tag{2.31}$$

Here, $\sigma_0$ is the size of stationary soliton solution in the units of the distance $a = 4.5\ A^\circ$.

However, in order to study the solitonic solution moving with the velocity $v$, it is convenient to use the model Hamiltonian (2.15) by eliminating bending and twisting of the alpha-helix i.e. $\alpha = 1$; and so only longitudinal waves are assumed as bellow

$$\hat{H}_{ex} = \sum_{n=1}^{N} \Big[ E_0 \hat{B}_n^{\dagger} \hat{B}_n - J \left( \hat{B}_n^{\dagger} \hat{B}_{n+1} + \hat{B}_n^{\dagger} \hat{B}_{n-1} \right) \Big] \tag{2.32}$$

$$\hat{H}_{ph} = \frac{1}{2} \sum_{n} \Big[ \frac{\hat{p}_n^2}{\tilde{M}} + \tilde{\Omega} (\hat{u}_{n+1} - \hat{u}_n)^2 \Big], \tag{2.33}$$

$$\hat{H}_{int} = \sum_{n} \chi (\hat{u}_{n+1} - \hat{u}_n) \hat{B}_n^{\dagger} \hat{B}_n. \tag{2.34}$$

In this model $\tilde{\Omega} = 3\Omega$ and $\tilde{M} = 3M$ and the soliton wave functions approximately are described by the same product (2.19) of the same exciton state vector (2.20) but with the different phonon state

$$|\Phi(t)\rangle = e^{-\frac{i}{\hbar} \sum [\beta_n(t) \hat{p}_n - \pi_n(t) \hat{u}_n]} |0\rangle_{ph}. \tag{2.35}$$

where by using of the Hadamard lemma [32], it is found

$$\begin{aligned} \langle \Phi | \hat{u}_n | \Phi \rangle &= \beta_n(t), \\ \langle \Phi | \hat{p}_n | \Phi \rangle &= \pi_n(t). \end{aligned} \tag{2.36}$$

According to the generalized Ehrenfest theorem following directly from the Schrödinger equation [32], the time dynamics of the expectation values (2.36) are

$$\frac{d}{dt} \beta_n(t) = \frac{1}{i\hbar} \langle \Big[ \hat{u}_n, \hat{H} \Big] \rangle; \qquad \frac{d}{dt} \pi_n(t) = \frac{1}{i\hbar} \langle \Big[ \hat{p}_n, \hat{H} \Big] \rangle, \tag{2.37}$$

where

$$\begin{aligned} \langle \Big[ \hat{u}_n, \hat{H} \Big] \rangle &= i\hbar \frac{\hat{p}_n}{M} \\ \langle \Big[ \hat{p}_n, \hat{H} \Big] \rangle &= i\hbar\Omega \left( \hat{u}_{n+1} - 2\hat{u}_n + \hat{u}_{n-1} \right) \\ &+ i\hbar\chi (\hat{B}_{n+1}^{\dagger} \hat{B}_{n+1} - \hat{B}_n^{\dagger} \hat{B}_n). \end{aligned} \tag{2.38}$$

From (2.37) and (2.38) it is obtained

$$\frac{d}{dt}\beta_n(t) = \frac{\pi_n}{M}; \qquad \frac{d}{dt}\pi_n(t) = M\frac{d^2}{dt^2}\beta_n, \tag{2.39}$$

Now, from (2.36), (2.37), (2.38) and (2.39) the temporal evaluation of phonon has the form

$$M\ddot{\beta}_n \;=\; \Omega(\beta_{n+1} - 2\beta_n + \beta_{n-1}) + \chi\Big(|C_n|^2 - |C_{n-1}|^2\Big) \tag{2.40}$$

Also, the temporal evaluation of electron is obtained by using Schrödinger equation,

$$i\hbar\frac{d}{dt}|\psi\rangle = \hat{H}|\psi\rangle, \tag{2.41}$$

where from Eqs. (2.19), (2.20), and (2.35) it is found

$$\partial_t|\psi\rangle = \left(\partial_t|\Psi\rangle\right)|\Phi\rangle + |\Psi\rangle\left(\partial_t|\Phi\rangle\right), \tag{2.42}$$

and then

$$\begin{aligned} i\hbar\frac{d}{dt}|\psi\rangle \;&=\; i\hbar\sum_n \frac{dC_n}{dt}\hat{B}_n^\dagger|0\rangle_{ex}|\Phi\rangle + |\Psi\rangle \\ &\times\; \sum_n\left(\frac{d\beta_n}{dt}\hat{p}_n - \frac{d\pi_n}{dt}\hat{u}_n + \frac{1}{2}\left(\beta_n\frac{d\pi_n}{dt} - \frac{d\beta_n}{dt}\pi_n\right)\right)|\Phi\rangle. \end{aligned} \tag{2.43}$$

The right-hand side of Schrödinger equation is calculated as

$$\begin{aligned} \hat{H}|\psi\rangle \;&=\; \sum_n\left(E_0C_n - J(C_{n+1} - C_{n-1})\right)\hat{B}_n^\dagger|0\rangle_{ex}|\Phi\rangle \\ &+\; \hat{H}_{ph}\hat{B}_n^\dagger|0\rangle_{ex}|\Phi\rangle + \chi\sum_n C_n(\hat{u}_{n+1} - \hat{u}_n)\hat{B}_n^\dagger|0\rangle_{ex}|\Phi\rangle. \end{aligned} \tag{2.44}$$

By combining of (2.43) and (2.44) and after taking the inner product with $\langle\Phi|_{ex}\langle 0|\hat{B}_n$, it is found

$$\begin{aligned} i\hbar\frac{dC_n}{dt} \;&=\; \Big(E_0 + W(t) - \frac{1}{2}\sum_n[\frac{d\beta_n}{dt}\pi_n - \beta_n\frac{d\pi_n}{dt}] \\ &+\; \chi(\beta_{n+1} - \beta_n)\Big)C_n - J(C_{n+1} + C_{n-1}). \end{aligned} \tag{2.45}$$

where $W(t) = \langle\psi|\hat{H}_{ph}|\psi\rangle$. For all $C_n$, setting

$$\gamma(t) = W(t) - \frac{1}{2}\sum_n [\frac{d\beta_n}{dt}\pi_n - \beta_n\frac{d\pi_n}{dt}] \tag{2.46}$$

is global because it is real and considering $C_n \to \bar{C}_n e^{-i/\hbar\int\gamma(t)dt}$ does not change the quantum probability amplitude $|C_n|^2 = |\bar{C}_n|^2$. Substituting this transformation in (2.45) and then re-labeling $C_n$ to $\bar{C}_n$, the system of Davydov equations becomes

$$\begin{aligned} i\hbar\dot{C}_n &= \Big(E_0 + \chi(\beta_{n+1} - \beta_n)\Big)C_n - J(C_{n+1} + C_{n-1}), \\ M\ddot{\beta}_n &= \Omega(\beta_{n+1} - 2\beta_n + \beta_{n-1}) + \chi\Big(|C_n|^2 - |C_{n-1}|^2\Big), \end{aligned} \tag{2.47}$$

An approximate solitonic solution of (2.47) is presented as

$$C_n(t) = \frac{e^{(i/\hbar)(m^* va(n-n_0)-Et)}}{\sqrt{8\sigma_0(1 - v^2/V_0^2)}}\text{sech}\left(\frac{a(n-n_0) - vt}{4a\sigma_0(1 - v^2/V_0^2)}\right) \tag{2.48}$$

where

$$\beta_{n+1} - \beta_n = -(\chi/\tilde{\Omega})\frac{|C_n|^2}{(1 - v^2/V_0^2)}, \tag{2.49}$$

in which $m^*$ is the effective mass of exciton and $V_0 = a(\tilde{\Omega}/\tilde{M})^{1/2}$ is the speed sound. Davydov's soliton travels with the initial velocity $v$ centered at molecule $n = n_0$ at time $t = 0$. Moreover,

$$E = E_0 - 2J - E_{BD} + \frac{1}{2}M_{sol}v^2 + O(v^4), \tag{2.50}$$

and

$$E_{BD} = \chi^4/24\tilde{\Omega}^2 J \tag{2.51}$$

is the soliton binding energy, and

$$M_{sol} = m^*(1 + \frac{1}{3}\tilde{M}\chi^4/\tilde{\Omega}^3\hbar^2) \tag{2.52}$$

is the effective mass of soliton. Clearly, setting $v = 0$ in the amplitude (2.48) results in the stationary solitonic amplitude (2.31) using the gauge (2.27).

## 2.3 Time dependent variational principle (TDVP)

The time-dependent variational principle or TDVP associates to a Hamiltonian quantum system mapping into a classical system whose equations of motion are yielded by the expectation value of quantum Hamiltonian. The Schrödinger equation is obtained by requiring that the action functional be stationary under free variation of the time-dependent state. This consists in the evaluation of the time-dependent operator action on coherent states of quantum harmonic oscillators. The scalar parameters describing the coherent states become generalized coordinates of a classical dynamical system whose equations of motion can be derived from a variational principle.

For a quantum system with Hamiltonian $\hat{H}$ and a state space $|\psi(x,t)\rangle$, the equations of motion can be derived using the following variational principle (equivalent to the least action principle)

$$\begin{aligned} |\psi\rangle = |\psi(x,t)\rangle; \quad \delta S = 0, \quad S &= \int_{t_1}^{t_2} L(\psi,\bar{\psi})dt, \\ L(\psi,\bar{\psi}) &= \frac{i}{2}\frac{\langle\psi|\dot{\psi}\rangle - \langle\dot{\psi}|\psi\rangle}{\langle\psi|\psi\rangle} - \frac{\langle\psi|\hat{H}|\psi\rangle}{\langle\psi|\psi\rangle} \end{aligned} \tag{2.53}$$

which can be worked out in the framework of classical Hamiltonian dynamics.

Regarding to the above definition, TDVP is a formulation of the time-dependent Schrdinger equation through variation of an action functional [33]. A TDVP approximation can be also done for the quantum state $|\psi(t)\rangle$ and quantum Hamiltonian $\hat{H}$ based on two assumptions:

- A new wave function $|\phi(t)\rangle$ is written in terms of $|\psi(t)\rangle$ by defining a time dependent phase factor $S(t) \in R$ so that

$$|\phi(t)\rangle = e^{iS(t)/\hbar}|\psi(t)\rangle, \tag{2.54}$$

  in which $S(t)$ will be determined in a self-consistent manner and the normalization condition $\langle\phi(t)|\phi(t)\rangle = 1$ is satisfied.

- $|\phi(t)\rangle$ satisfies the weaker form of the Schrödinger equation

$$i\hbar\langle\phi(t)|\partial_t|\phi(t)\rangle = \langle\phi(t)|\hat{H}|\phi(t)\rangle. \tag{2.55}$$

Then theses two assumptions give

$$-\dot{S}(t) + i\hbar\langle\psi(t)|\partial_t|\psi(t)\rangle = \langle\psi(t)|\hat{H}|\psi(t)\rangle. \tag{2.56}$$

Integrating, it is found

$$S(t) = \int_0^t \Big[i\hbar\langle\psi(t)|\partial_t|\psi(t)\rangle - \langle\psi(t)|\hat{H}|\psi(t)\rangle\Big]dt. \tag{2.57}$$

and the equations of motion is derived by requiring that the action with the Lagrangian

$$L = i\hbar\langle\psi(t)|\partial_t|\psi(t)\rangle - \langle\psi(t)|\hat{H}|\psi(t)\rangle \ , \tag{2.58}$$

to be stationary

$$\delta S(t) = \delta \int L dt = 0. \tag{2.59}$$

It is worth noting that the TDVP applies generically to any quantum system and its effectiveness depends on a reasonable choice of the initial ansatz for the state vector.

# CHAPTER 3. Quantum state transfer through Davydov model

In this chapter quantum maps (channels) are introduced and then the operator sum representation and some classes of qubit channels are reported which are useful for studying information transfer fidelity (ITF) in qubit networks. The aim of this chapter is to study ITF in a simplified Davydov's model (2.2.2) (without environment/phonons) as an elementary step to subsequent chapters. To this end, we investigate transmission fidelity in a chain of two molecules and, independently, in a biomolecule with N molecules.

## 3.1 Quantum maps

Transmitting a quantum state from one place to another is an important task in quantum information theory. These kinds of communications are described mostly by quantum channels which are linear transformation mapping density operators to density operators. More formally, $\mathcal{D}(H)$ denotes the space of linear operators acting on the Hilbert space $H$, i.e. $\rho_A \in \mathcal{D}(H_A)$ and $\rho_B \in \mathcal{D}(H_B)$, where the density operator $\rho$ introduced in section (2.1). Therefore, a quantum maps is introduced by

$$\Phi : \mathcal{D}(H_A) \to \mathcal{D}(H_B) \tag{3.1}$$

where $H_A = span\{|\psi_x\rangle\}_{x\in A}$ and $H_B = span\{|\psi_x\rangle\}_{x\in B}$. Each quantum channel is called a completely positive trace preserving (CPTP) map enjoying the properties [25]:

- Linearity:

$$\Phi(\lambda_1\rho_1 + \lambda_2\rho_2) = \lambda_1\Phi(\rho_1) + \lambda_2\Phi(\rho_2) \tag{3.2}$$

  when $\rho_1, \rho_2 \in \mathcal{D}(H_A)$ and $\lambda_1, \lambda_2$ are real.

- Trace presevation:

$$Tr(\Phi(\rho)) = 1 \tag{3.3}$$

when $\rho \in \mathcal{D}(H_A)$.

- Positivity:

  This property means that $\Phi$ maps positive operators to positive operators. Note that any density matrix $\rho$ must be positive, then we must have also $\Phi(\rho) > 0$, when $\rho \in \mathcal{D}(H_A)$.

- Complete positivity:

  Stronger than positivity, $\Phi$ must be complete positivity. If $(\Phi \otimes \mathcal{I}_R)(\rho) \geq 0$ for any $\rho \in \mathcal{D}(H_A \otimes H_R)$, then $\Phi$ is a complete positive (CP) map, where $\mathcal{I}_R$ denotes the identity (super-)operator on an ancillary (reference) Hilbert space $H_R$.

### 3.1.1 The operator sum representation (OSR)

We consider a system $S$ and bath $B$ with a joint unitary evolution $U(t) = e^{-iHt}$. The initial state is $\rho(0) = \rho_S(0) \otimes \rho_B(0)$. Then, the time evaluation $\rho(t)$ by (2.3) gives [34]

$$\rho(t) = U(t)\rho(0)U^\dagger(t) = U(t)\rho_S(0) \otimes \rho_B(0)U^\dagger(t). \tag{3.4}$$

As the density operator of the bath is positive and normalized, it has a spectral decomposition in an orthonormal basis with non-negative eigenvalues

$$\rho_B(0) = \sum_\nu \lambda_\nu |\nu\rangle\langle\nu|, \tag{3.5}$$

where $\lambda_\nu$ are the eigenvalues and $|\nu\rangle$ are the corresponding orthonormal eigenvectors. Taking a partial trace over the bath ON (3.4) gives us the time evaluation of the system

$$\rho_S(t) = Tr_B[\rho(t)] = \sum_\mu \langle\mu|U(t)\rho_S(0) \otimes \rho_B(0)U^\dagger(t)|\mu\rangle, \tag{3.6}$$

which leads to

$$\begin{aligned}\rho_S(t) &= \sum_{\mu}\langle\mu|U(t)\rho_S(0)\otimes\sum_{\nu}\lambda_\nu|\nu\rangle\langle\nu|U^\dagger(t)|\mu\rangle \\ &= \sqrt{\lambda_\nu}\langle\mu|U(t)|\nu\rangle_B\rho_S(0)\sqrt{\lambda_\mu}\langle\nu|U^\dagger(t)|\mu\rangle_B \\ &= \sum_{\mu\nu}K_{\mu\nu}(t)\rho_S(0)K^\dagger_{\mu\nu}(t), \end{aligned} \tag{3.7}$$

where the operators $K_{\mu\nu}(t)$ are called the Kraus operators and are given by

$$K_{\mu\nu}(t) = \sqrt{\lambda_\nu}\langle\mu|U(t)|\nu\rangle. \tag{3.8}$$

The partial matrix element, leaving us with an operator acting on the system. The equation (3.7) defining the evolution of the system in terms of Kraus operator is called the Kraus OSR. From (3.4), the evolution of the state $\rho_S$ of an open quantum system can be expressed as unitary evolution of the composite system+bath, followed by a partial trace, which leads to the Kraus OSR:

$$\Phi(\rho) = Tr_B[U(t)(\rho_S\otimes\rho_B)U(t)] = \sum_{\alpha}K_\alpha(t)\rho_S(0)K^\dagger_\alpha(t) \tag{3.9}$$

where $\alpha = \mu\nu$ and $\rho_S(t)\to\Phi(\rho)$. From now, we drop the $S$ subscript since we will focus on the system alone.

The Kraus operators satisfy an important constraint known as the completeness relation arising from the analogous requirement $Tr(\rho(t)) = 1$ as

$$\begin{aligned} Tr[\rho(t)] &= 1 = Tr\Big(\sum_{\alpha}K_\alpha(t)\rho(0)K^\dagger_\alpha(t)\Big) \\ &= Tr\Big(\sum_{\alpha}K^\dagger_\alpha(t)K_\alpha(t)\rho(0)\Big) = 1, \end{aligned} \tag{3.10}$$

where it follows that we must have

$$\sum_{\alpha}K^\dagger_\alpha(t)K_\alpha(t) = 1. \tag{3.11}$$

OSR representation can capture the measurement postulate. By the measurement operators $\{M_k\}$, the state $\rho$ maps to

$$\rho \to \rho_k = \frac{M_k \rho M_k^\dagger}{Tr[M_k \rho M_k^\dagger]}, \tag{3.12}$$

with probability $p_k = Tr[M_k \rho M_k^\dagger]$. The measurement operators satisfy the completeness equation

$$\sum_k M_k^\dagger M_k = I. \tag{3.13}$$

Consider the case where we perform the measurement (3.12) but do not learn the outcome $k$. Then the non-selective measurement is given by

$$\rho \to \langle \rho \rangle = \sum_k p_k \rho_k = \sum_k M_k \rho M_k^\dagger. \tag{3.14}$$

This form is in the Kraus operator-sum representation with the Kraus operators $\{M_k\}$. The set $\{M_k\}$ is a probability operator value measure (POVM).
Since both dynamics (3.9) and measurements (3.14) are explained completely by the OSR, this confirm that the OSR is truly fundamental.

### 3.1.2 Qubit channels

The density matrix of a qubit may be written as $\rho = \frac{1}{2}(I + \vec{v}.\vec{\sigma})$ where $\vec{\sigma} = (\sigma_x, \sigma_y, \sigma_z)$ and $\vec{v} = \{v_x, v_y, v_z\} \in \mathbb{R}^3$ is the Bloch vector. In this way, a single-qubit state may be thought of as a point in or on the unit sphere in $\mathbb{R}^3$- the Bloch sphere [34]. States with $|\vec{v}| = 1$ lie on the surface of the sphere and correspond to pure states of the form $\rho = |\psi\rangle\langle\psi|$. Points on the interior of the sphere correspond to mixed states with purity $Tr(\rho^2) < 1$. $\Phi$ as a map of the density matrix acts on a single qubit $\rho \to \rho'$. At the same time $\rho'$ must be expressible in terms of a new Bloch vector $\vec{v'}$, where $\rho' = \frac{1}{2}(I + \vec{v'}.\vec{\sigma})$. $\rho \to \rho'$ is equivalent to mapping the Bloch vector

$$v \to \vec{v'} = M\vec{v} + \vec{c} \tag{3.15}$$

for some real $3 \times 3$ matrix $M$ and a vector $\vec{c} \in \mathbb{R}^3$.

To prove eq. (3.15) we plug the Bloch vector representation of $\rho$ into the quantum map (3.9)

$$\begin{aligned} \rho' &= \sum_\alpha K_\alpha \rho K_\alpha^\dagger = \frac{1}{2}\sum_\alpha K_\alpha (I + \vec{v}.\vec{\sigma}) K_\alpha^\dagger \\ &= \frac{1}{2}(\sum_\alpha K_\alpha K_\alpha^\dagger + \sum_{\alpha j} v_j K_\alpha \sigma j K_\alpha^\dagger) \end{aligned} \tag{3.16}$$

To isolate the components of $v'$ we multiply both sides by $\sigma_i$ and take the trace, while we know that the Pauli matrices are all traceless and satisfy $Tr(\sigma_k \sigma_l) = 2\delta_{kl}$. So,

$$Tr(\rho' \sigma_i) = \frac{1}{2}[\sum_\alpha Tr(K_\alpha K_\alpha^\dagger \sigma i) + \sum_{\alpha j} v_j Tr(K_\alpha \sigma j K_\alpha^\dagger \sigma i)] \tag{3.17}$$

On the other hand, using $\rho' = \frac{1}{2}(I + \vec{v'}.\vec{\sigma})$ again

$$Tr(\rho' \sigma_i) = \frac{1}{2}[Tr(\sigma_i) + \sum_j v_j' Tr(\sigma_j \sigma_i)] = 0 + v_i' \tag{3.18}$$

Equating eqs. (3.17) and (3.18) we thus have

$$v_i' = c_i + \sum_j M_{ij} v_j \tag{3.19}$$

where

$$M_{ij} = \frac{1}{2}\sum_{\alpha j} Tr(K_\alpha \sigma_j K_\alpha^\dagger \sigma_i), \tag{3.20}$$

$$c_i = \frac{1}{2}\sum_\alpha Tr(\sigma_i K_\alpha K_\alpha^\dagger) \tag{3.21}$$

where both $M_{ij}$ and $c_i$ are real. This proves eq. (3.15).

A quantum map is said to be unital if it maps the identity operator to itself; $\Phi$ is unital if $\Phi(I) = I$, otherwise it is non-unital. From eq. (3.20), if $\Phi$ is unital then from (3.11) we have

$$c_i = \frac{1}{2}\sum_\alpha Tr(\sigma_i K_\alpha K_\alpha^\dagger) = Tr(\sigma_i) = 0 \tag{3.22}$$

Conversely, if $\Phi$ is non-unital, then $c_i \neq 0$.

**Phase damping map (phase flip map)**

The phase damping map is:

$$\Phi(\rho) = p\rho + (1-p)Z\rho Z \tag{3.23}$$

where the Kraus operatirs are $K_1 = \sqrt{p}I$ and $K_2 = \sqrt{1-p}Z$, where $Z \equiv \sigma_z$ the $z$ component of the Pauli operator.

$$\rho \to \rho' = \begin{cases} \rho & \text{prob. p} \\ Z\rho Z & \text{prob. 1-p} \end{cases} \tag{3.24}$$

The map is unital

$$c_i = \frac{1}{2}\sum_{\alpha} Tr(\sigma_i K_\alpha K_\alpha^\dagger) = \frac{1}{2}[pTr(\sigma_i) + (1-p)Tr(\sigma_i)] = 0 \tag{3.25}$$

and

$$\begin{aligned} M_{ij} &= \frac{1}{2}\sum_{\alpha_j} Tr(K_\alpha \sigma_j K_\alpha^\dagger \sigma_i) = \frac{1}{2}[pTr(\sigma_i\sigma_j) + (1-p)Tr(\sigma_i Z\sigma_j Z)] \\ &= diag(2p-1, 2p-1, 1) \end{aligned} \tag{3.26}$$

and from (3.15) we arrive

$$\vec{v'} = M\vec{v} = ((2p-1)v_x, (2p-1)v_y, v_z), \tag{3.27}$$

Where the phase flip map leaves the $v_z$ axis alone and shrinks the Bloch sphere in the $(v_x, v_y)$ plane. Also

$$\begin{aligned} Tr[(\rho')^2] &= \frac{1}{2}(1 + |v'|^2) \\ &= \frac{1}{2}[1 + (2p-1)^2(v_x^2 + v_y^2) + v_z^2] \leq Tr[(\rho)^2] \end{aligned} \tag{3.28}$$

Thus the purity always decreases under the phase flip channel, except for the states $\vec{v} = (0, 0, v_z)$ whose purity is invariant.

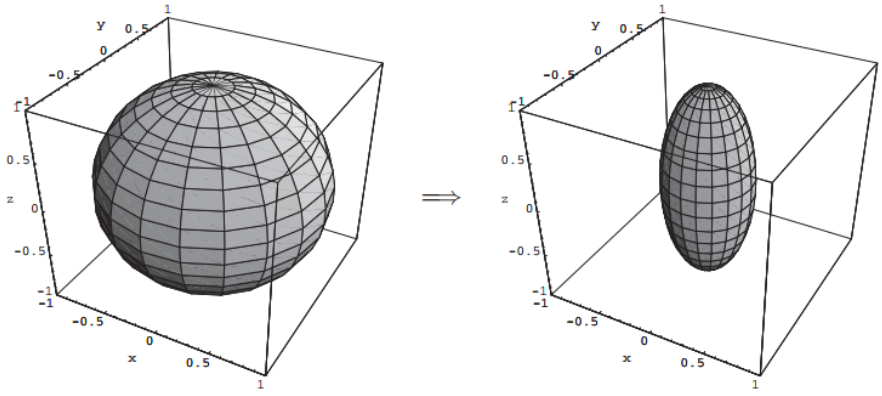

Figure 3.1 Adapted by [25]. The effect of the phase flip channel on the Bloch sphere. Note that the $v_z$ is left fixed, while the $v_x$ and $v_y$ are uniformly contracted by a factor of $1-2p$.

**Bit flip map**

The bit flip map is:

$$\Phi(\rho) = p\rho + (1-p)X\rho X \tag{3.29}$$

where

$$\rho \to \rho' = \begin{cases} \rho & \text{prob. p} \\ X\rho X & \text{prob. 1-p.} \end{cases} \tag{3.30}$$

Using $\rho = \frac{1}{2}(I + \vec{v}.\vec{\sigma})$ and (3.29) we have:

$$\rho \to \rho' = \frac{1}{2}(I + p\vec{v}.\vec{\sigma} + (1-p)X\vec{v}.\vec{\sigma}X) \tag{3.31}$$

in which

$$X(\vec{v}.\vec{\sigma})X = X(v_xX + v_yY + v_zZ)X = v_xX - v_yY - v_zZ. \tag{3.32}$$

Then (3.31) becomes

$$\rho' = \frac{1}{2}(I + v_xX + (2p-1)v_yY + (2p-1)v_zZ) = \frac{1}{2}(I + \vec{v'}.\vec{\sigma}). \tag{3.33}$$

Thus the bit flip map leaves $v_x$ axis alone and shrinks the Bloch sphere in the $(v_y, v_z)$ plane. Moreover

$$\vec{v'} = (v_x, (2p-1)v_y, (2p-1)v_z) = M\vec{v}, \tag{3.34}$$

in which from (3.15) we see $\vec{c} = 0$ which means the bit flip map is unital. If we replace X with Y in Eq. (3.29) we have the "bit-phase flip channel," where the roles of the $v_x$ and $v_y$ axes is interchanged.

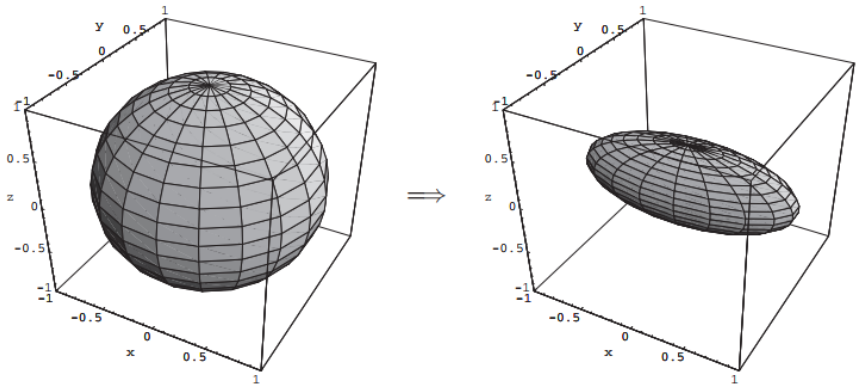

Figure 3.2 Adapted by [25]. The effect of the bit flip map on the Bloch sphere. The sphere on the left represents the set of all pure states, and the deformed sphere on the right represents the states after going through the channel. Note that the $v_x$ axis is left fixed, while the $v_y$ and $v_z$ are uniformly contracted by a factor of $1-2p$.

**Depolarizing map**

The depolarizing map is introduced as

$$\Phi(\rho) = p\frac{I}{2} + (1-p)\rho \tag{3.35}$$

which means

$$\rho \to \rho' = \begin{cases} \frac{I}{2} & \text{prob. p} \\ \rho & \text{prob. 1-p.} \end{cases} \tag{3.36}$$

Using $\rho = \frac{1}{2}(I + \vec{v}.\vec{\sigma})$ in Eq. (3.35) results in

$$\Phi(\rho) = p\frac{I}{2} + \frac{1-p}{2}(I + \vec{v}.\vec{\sigma}) = \frac{1}{2}(I + \vec{v'}.\sigma), \tag{3.37}$$

where $\vec{v'} = (1-p)\vec{v}$ and form (3.15) we conclude that $\vec{c} = 0$ meaning the depolarizing map is unital. Eq. (3.37) shows the Bloch sphere shrinking uniformly to a radius of $1-p$. The fully mixed state $\vec{v} = 0$ (the origin) is the only invariant state. Other states lose purity as they get more mixed.

It is clear that the Eq. (3.35) is not in a Kraus operator form (3.9), however by using (3.32) and also

$$\begin{aligned} Y(\vec{v}.\vec{\sigma})Y &= -v_x X + v_y Y - v_z Z, \\ Z(\vec{v}.\vec{\sigma})Z &= -v_x X - v_y Y + v_z Z, \end{aligned} \tag{3.38}$$

we can see that

$$\rho + X\rho X + Y\rho Y + Z\rho Z = 2I, \tag{3.39}$$

in which $\sum_j \sigma_j(\vec{v}.\vec{\sigma})\sigma_j = 0$. So, the Eq. (3.35) can be rewritten as

$$\begin{aligned} \Phi(\rho) &= \frac{p}{4}(\rho + X\rho X + Y\rho Y + Z\rho Z) + (1-p)\rho \\ &= (1 - \frac{3p}{4})\rho + \frac{p}{4}(X\rho X + Y\rho Y + Z\rho Z), \end{aligned} \tag{3.40}$$

which gives the Kraus operators of the depolarizing map (3.35) as

$$\begin{aligned} K_0 &= \sqrt{1 - \frac{3p}{4}}I, \\ K_i &= \sqrt{\frac{p}{4}}\sigma_i, \quad i = 1, 2, 3. \end{aligned} \tag{3.41}$$

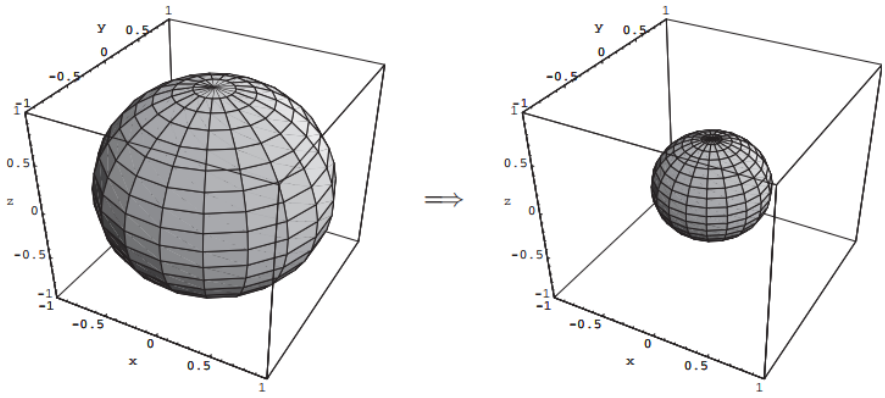

Figure 3.3 Adapted by [25]. The effect of the depolarizing map on the Bloch sphere. Note how the entire sphere contracts uniformly as a function of $p$.

### Amplitude damping channel

Spontaneous emission (SE) is the process by which an atom, nucleus, etc., undergoes a transition from a higher state of energy to a lower state of energy, thus releasing energy to the bath (relaxation). This could through the release of a photon, a phonon, or some other elementary excitation. If the bath is at temperature $T = 0$, then the system cannot absorb energy, so the reverse process of excitation does not occur. We consider a single qubits, with a ground state $|0\rangle$ and an excited state $|1\rangle$. Thus the map $\Phi$ is:

$$\begin{cases} |0\rangle \to |0\rangle \quad \text{prob. } 1 \\ |1\rangle \to |0\rangle \quad \text{prob. p} \end{cases} \tag{3.42}$$

One of the Kraus operator is obvious $K_1 = \sqrt{p}|0\rangle\langle 1|$. The second Kraus operator should keep the ground state $|0\rangle\langle 0|$; but the normalization condition should be satisfied. Thus we consider the state

$$K_2 = |0\rangle\langle 0| + S = \begin{pmatrix} 1 & a \\ b & c \end{pmatrix} \tag{3.43}$$

and considering the normalization condition $K_1K_1^\dagger + K_2K_2^\dagger = 1$ becomes:

$$\begin{pmatrix} 1+|b|^2 & a+b^*c \\ a^*+bc^* & |a|^2+|c|^2 \end{pmatrix} + p|1\rangle\langle 0|0\rangle\langle 1| = \begin{pmatrix} 1 & 0 \\ 0 & 1 \end{pmatrix} \tag{3.44}$$

then we obtain

$$K_2 = \begin{pmatrix} 1 & 0 \\ 0 & \sqrt{1-p} \end{pmatrix} \tag{3.45}$$

Since

$$\rho' = \sum_{\alpha=1}^{2} K_\alpha[\frac{1}{2}(I+\vec{v}.\vec{\sigma})]K_\alpha^\dagger = \frac{1}{2}(I+\vec{v'}.\vec{\sigma}), \tag{3.46}$$

the good direct way to get $M$ and $\vec{c}$ of (3.15) is to map $I$ and $\vec{v}.\vec{\sigma}$ via the Kraus OSR

$$\begin{aligned} I \quad &\rightarrow \quad K_1K_1^\dagger + K_2K_2^\dagger = \begin{pmatrix} 1 & 0 \\ 0 & 1-p \end{pmatrix} + p|0\rangle\langle 1|1\rangle\langle 0| \\ &= \quad \begin{pmatrix} 1+p & 0 \\ 0 & 1-p \end{pmatrix} = I + pZ \end{aligned} \tag{3.47}$$

Thus SE is not a unital map and we have

$$\vec{c} = (0,0,p) \tag{3.48}$$

Then we study $\vec{v}.\vec{\sigma} \rightarrow K_1(\vec{v}.\vec{\sigma})K_1^\dagger + K_2(\vec{v}.\vec{\sigma})K_2^\dagger$ which gives

$$\begin{aligned} K_1XK_1^\dagger + K_2XK_2^\dagger &= \sqrt{1-p}X \\ K_1YK_1^\dagger + K_2YK_2^\dagger &= \sqrt{1-p}Y \\ K_1ZK_1^\dagger + K_2ZK_2^\dagger &= (1-p)Z \end{aligned} \tag{3.49}$$

and consequently we obtain $M = diag(\sqrt{1-p}, \sqrt{1-p}, 1-p)$. The geometric meaning of the spontaneous emission map is now clear. The center $(0,0,0,) \rightarrow (0,0,p)$ and the Bloch sphere

is compressed more along the $v_z$ axis than along the $v_x$ and $v_y$ axes. In other words, all points on the Bloch sphere move closer to its north pole, which is the ground state.

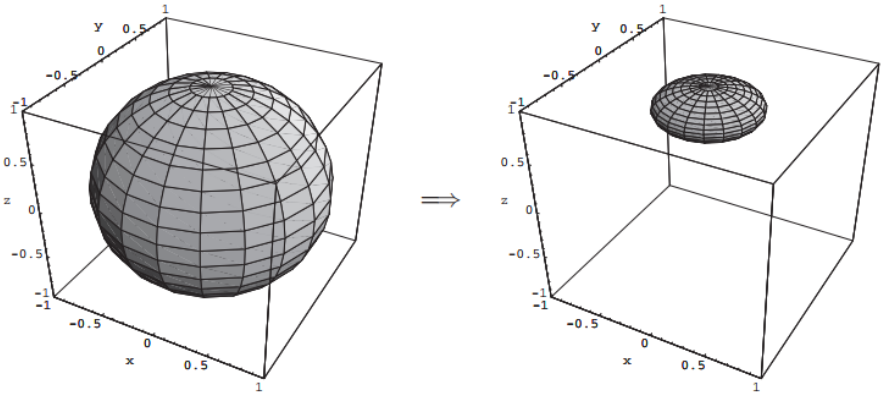

Figure 3.4 Adapted by [25]. The effect of the amplitude damping map on the Bloch sphere. Note how the entire sphere shrinks towards the north pole, the $|0\rangle$.

## 3.2 Information transfer in a chain of two molecules

Considering the exciton in Davydovs model as an electron, then its Hamiltonian in (2.16) is written as

$$\begin{aligned}\hat{H}_{el} &= \sum_{n=1}^{N}\sum_{\alpha=1}^{3}\Big[E_0\hat{B}^{\dagger}_{n,\alpha}\hat{B}_{n,\alpha} + J\left(\hat{B}^{\dagger}_{n,\alpha}\hat{B}_{n+1,\alpha} + \hat{B}^{\dagger}_{n,\alpha}\hat{B}_{n-1,\alpha}\right)\\ &+ L\left(\hat{B}^{\dagger}_{n,\alpha}\hat{B}_{n,\alpha+1} + \hat{B}^{\dagger}_{n,\alpha}\hat{B}_{n,\alpha-1}\right)\Big],\end{aligned} \tag{3.50}$$

where $\hat{B}$ and $\hat{B}^{\dagger}$ are the lowering and rising operators for spin-$\frac{1}{2}$ and the tunneling term $J$ is considered positive for an excited electron [35]. Hamiltonian (3.50) implies to deal with $3N$ qubits with associated space of states $\mathcal{H} \simeq (\mathbb{C}^2)^{\otimes 3N}$. This is described by a $2^{3N} \times 2^{3N}$ matrix with the usual computational basis for qubits. We can study the qubit state transfer along a macromolecule by considering the latter as a spin network. To describe a network of $3N$ spin-half quantum particles, let $G = (V, E)$ be a simple undirected graph (that is, without loops or parallel edges), with a set of vertices (nodes) $V(G) = \{1, \ldots, 3N\}$ and set of edges $E(G)$. So, the particles are attached to the vertices of $G$, while the edges of $G$ denote their allowed couplings. We restrict our attention to the union of the single excitation subspace (2.20). In

$t = 0$ we introduce the one-spin-up vector

$$|k\rangle = |000...1....00\rangle, k = 1, 2, ..., s, ..., r, ..., 3N \tag{3.51}$$

in which the spin at the $k-$th site has been flipped to the state $|1\rangle$ [36]. Alice places a spin in the unknown generic state at the $s$-th site in the spin chain

$$|\psi(t=0)\rangle = \cos\frac{\theta}{2}|0\rangle + e^{i\phi}\sin\frac{\theta}{2}|s\rangle, \tag{3.52}$$

where $\theta \in [0, \pi]$, $\phi \in [0, 2\pi]$ and $|0\rangle = |00...00\rangle$. Bob wants to retrieve this state, or a state as close to it as possible, from the $r-$th site of the graph, i.e., $|\psi(t)\rangle_r = \cos\frac{\theta}{2}|0\rangle + e^{i\phi}\sin\frac{\theta}{2}|r\rangle$. The time evaluation of the systems is obtained by (3.4) and the input state $\rho(0) = |\psi(t)\rangle\langle\psi(0)$. The state of the $r$-th qubit (output) after time $t$ is described by the partial trace overall qubits but $r$-th on the density operator $\rho(t) = |\psi(t)\rangle\langle\psi(t)|$ read as $\rho_r(t) = \mathrm{Tr}_{\not r}[\rho(t)]$. In this section we consider a two-molecule system and study the quantum state transport on them through fidelity and ITF. Then in the next section we investigate ITF in a chain of $N$ molecules.

We consider just two molecules ($N = 2$) and non-periodic condition for $\alpha$, so that the Hamiltonian (3.50) becomes

$$\begin{aligned}\hat{H}_{el} &= J\Big(\hat{B}^{\dagger}_{1,1}\hat{B}_{2,1} + \hat{B}^{\dagger}_{1,2}\hat{B}_{2,2} + \hat{B}^{\dagger}_{1,3}\hat{B}_{2,3} + H.c\Big). \\ &+ L\Big(\hat{B}^{\dagger}_{1,1}\hat{B}_{1,2} + \hat{B}^{\dagger}_{2,1}\hat{B}_{2,2} + \hat{B}^{\dagger}_{1,2}\hat{B}_{1,3} + \hat{B}^{\dagger}_{2,2}\hat{B}_{2,3} + H.c\Big).\end{aligned} \tag{3.53}$$

where for simplicity the constant energy $E_0$ is considered zero. It is a reasonable choice because $E_0$ is just a shift of energy in the Hamiltonian (3.50) and we may suppose all the qubits are in their lowest energy states. The associated space of states is $\mathcal{H} \simeq (\mathbb{C}^2)^{\otimes 6}$. Union of the single excitation subspace and the null space of the Hamiltonian (3.53) is $\widetilde{\mathcal{H}} = span\{|k\rangle\}_{k=0}^{6}$. Here according to (3.51), the vector $|k\rangle = |0\rangle_1 \ldots |1\rangle_k \ldots |0\rangle_6$ indicates the presence of excitation in the $k$th site under the convention

$$k = (\alpha - 1)N + n. \tag{3.54}$$

The Hamiltonian $\hat{H}_{el}$ in the basis $\{|k\rangle\}_{k=1}^{6}$ ($|0\rangle$ belongs to its null space) has the matrix

representation

$$\begin{pmatrix} 0 & -J & L & 0 & 0 & 0 \\ -J & 0 & 0 & L & 0 & 0 \\ L & 0 & 0 & -J & L & 0 \\ 0 & L & -J & 0 & 0 & L \\ 0 & 0 & L & 0 & 0 & -J \\ 0 & 0 & 0 & L & -J & 0 \end{pmatrix} \tag{3.55}$$

with eigenvalues $\{-J, J, -J - \sqrt{2}L, J - \sqrt{2}L, -J + \sqrt{2}L, J + \sqrt{2}L\}$.

The unitary evolution operator

$$\hat{U}(t) = e^{-i\hat{H}_{el}t} \tag{3.56}$$

($\hbar = 1$) can then be represented as

$$\begin{pmatrix} U_{11} & U_{12} & U_{13} & U_{14} & U_{15} & U_{16} \\ U_{21} & U_{22} & U_{23} & U_{24} & U_{25} & U_{26} \\ U_{31} & U_{32} & U_{33} & U_{34} & U_{35} & U_{36} \\ U_{41} & U_{42} & U_{43} & U_{44} & U_{45} & U_{46} \\ U_{51} & U_{52} & U_{53} & U_{54} & U_{55} & U_{56} \\ U_{61} & U_{62} & U_{63} & U_{64} & U_{65} & U_{66} \end{pmatrix} \tag{3.57}$$

where

$$
\begin{aligned}
U_{11}(t) &= U_{22}(t) = U_{33}(t) = U_{44}(t) = U_{55}(t) = U_{66}(t) \\
&= \frac{1}{8} e^{-i(J+\sqrt{2}L)t}(1+e^{i2Jt})(1+e^{i\sqrt{2}Lt})^2, \\
U_{21}(t) &= U_{12}(t) = U_{34}(t) = U_{43}(t) = U_{56}(t) = U_{65}(t) \\
&= \frac{1}{8} e^{-i(J+\sqrt{2}L)t}(-1+e^{i2Jt})(1+e^{i\sqrt{2}Lt})^2, \\
U_{31}(t) &= U_{13}(t) = U_{42}(t) = U_{24}(t) = U_{53}(t) = U_{35}(t) = U_{64}(t) = U_{46}(t) \\
&= \frac{-1}{4\sqrt{2}} e^{-i(J+\sqrt{2}L)t}(1+e^{i2Jt})(-1+e^{i2\sqrt{2}Lt}), \\
U_{41}(t) &= U_{14}(t) = U_{32}(t) = U_{23}(t) = U_{45}(t) = U_{54}(t) = U_{36}(t) = U_{63}(t) \\
&= \frac{-1}{4\sqrt{2}} e^{-i(J+\sqrt{2}L)t}(-1+e^{i2Jt})(-1+e^{i2\sqrt{2}Lt}), \\
U_{51}(t) &= U_{15}(t) = U_{62}(t) = U_{26}(t) \\
&= \frac{1}{8} e^{-i(J+\sqrt{2}L)t}(1+e^{i2Jt})(-1+e^{i\sqrt{2}Lt})^2, \\
U_{61}(t) &= U_{16}(t) = U_{52}(t) = U_{25}(t) \\
&= \frac{1}{8} e^{-i(J+\sqrt{2}L)t}(-1+e^{i2Jt})(-1+e^{i\sqrt{2}Lt})^2. \qquad (3.58)
\end{aligned}
$$

Let us indicate by $i$ and $j$ the input and output nodes respectively. Concerning (3.52), we initially consider the input qubit in a generic state

$$
|\psi\rangle_i = \cos\frac{\theta}{2}|0\rangle_i + e^{i\phi}\sin\frac{\theta}{2}|1\rangle_i \qquad (3.59)
$$

and all the other qubit in the ground state. That is, the initial state of the network reads as

$$
|\psi(0)\rangle = |0\rangle_1 \ldots |\psi\rangle_i \ldots |0\rangle_{3N}. \qquad (3.60)
$$

The time evolution of the density operator $\hat{\rho}(t)$ is given by (3.4) where $\rho_S(0) = |\psi\rangle_i\langle\psi|$ is taken part from $\hat{\rho}(0) = |\psi(0)\rangle\langle\psi(0)|$ so that the rest is considered as the density operator of bath $\rho_B(0)$. The state of the output qubit after time $t$ is described by the partial trace overall qubits but the output one, $\rho_j(t) = \mathrm{Tr}_{\not j}[\rho(t)]$. Then we arrive at

$$
\begin{aligned}
\hat{\rho}_j(t) &= \left[\cos^2\frac{\theta}{2} + \sin^2\frac{\theta}{2}\sqrt{1-|U_{ji}|^2}\right]|0\rangle_j\langle 0| + \sin^2\frac{\theta}{2}|U_{ji}|^2|1\rangle_j\langle 1| \\
&+ e^{i\phi}\sin\frac{\theta}{2}\cos\frac{\theta}{2}U_{ji}^*|0\rangle_j\langle 1| + e^{-i\phi}\sin\frac{\theta}{2}\cos\frac{\theta}{2}U_{ji}|1\rangle_j\langle 0|. \qquad (3.61)
\end{aligned}
$$

According to (3.9) and the section (3.1.2), the resulting reduced dynamics corresponds to an amplitude damping channel applied to the input state, i.e.

$$\hat{\rho}_j(t) = \hat{K}_0|\psi\rangle_i\langle\psi|\hat{K}_0^\dagger + \hat{K}_1|\psi\rangle_i\langle\psi|\hat{K}_1^\dagger, \tag{3.62}$$

with (Kraus) operators

$$\hat{K}_0 = |0\rangle_{ji}\langle 0| + z|1\rangle_{ji}\langle 1|, \tag{3.63}$$

$$\hat{K}_1 = \sqrt{1-|z|^2}\,|0\rangle_{ji}\langle 1|, \tag{3.64}$$

and

$$z := \langle j|\hat{U}(t)|i\rangle. \tag{3.65}$$

where $\hat{U}(t) = e^{-i\hat{H}_{el}t}$. The fact that the reduced dynamics is described by an amplitude damping channel is a consequence of the commutativity of the system Hamiltonian (3.53) with the operator $\hat{N} = \sum_{k=1}^{3N} |k\rangle\langle k|$ expressing the total number of excitations in the network [37].
If the state at the output node overlaps on the input state, that is, if the output state reads $|\psi\rangle_j$, thus it would be natural to consider as figure of merit for PST the fidelity (2.7) as

$$f_{ij} = {}_j\langle\psi|\hat{\rho}_j(t)|\psi\rangle_j, \tag{3.66}$$

However, after the interaction among qubit, we can admit the action of an arbitrary unitary operation $\hat{V}$ at the output qubit aimed at facilitating the decoding. Thus the fidelity (3.66) can be more properly defined as [38]

$$f_{ij}^{\hat{V}}(\theta,\phi,t) := {}_i\langle\psi|\hat{V}\rho_j(t)\hat{V}^\dagger|\psi\rangle_i, \tag{3.67}$$

Obviously perfect state transfer (PST) is obtained if there exist an evolution time $t$ and a unitary $\hat{V}$ such that $f_{\text{io}}^{\hat{V}}(\theta,\phi,t) = 1$ for all $\theta$ and $\phi$. To circumvent the dependence from too many variables, we shall take the average over $\theta$ and $\phi$

$$F_{ij}^{\hat{V}}(t) = \frac{1}{4\pi}\int_0^\pi d\theta \sin\theta \int_0^{2\pi} d\phi\; f_{ij}^{\hat{V}}(\theta,\phi,t), \tag{3.68}$$

and the maximum over $\hat{V}$

$$F_{ij}(t) = \max_{\hat{V}} F_{ij}^{\hat{V}}(t). \tag{3.69}$$

In order to optimize $\hat{V}$, let us set

$$\hat{V} = u|0\rangle\langle 0| + v|0\rangle\langle 1| - v^*|1\rangle\langle 0| + u^*|1\rangle\langle 1|, \tag{3.70}$$

with $u, v \in \mathbb{C}$, $|u|^2 + |v|^2 = 1$. This yields

$$F_{ij}^{\hat{V}}(t) = \frac{1}{2} + \frac{Re(z^* u^2)}{3} + \frac{|z|^2}{6}\left(2|u|^2 - 1\right). \tag{3.71}$$

It follows that the optimal choice is $u = e^{iargz/2}$, leading to

$$F_{ij}(t) = \frac{1}{2} + \frac{|z|}{3} + \frac{|z|^2}{6}. \tag{3.72}$$

When $z = 1$ the fidelity (3.72) becomes unity.

We have seen that the quantity to study is $z$. It represents the quantum probability of transition [39] from state $|i\rangle$ to state $|j\rangle$ in time $t$, namely

$$p_t(i,j) := |\langle i|e^{-i\hat{H}_{el}t}|j\rangle|^2 = |z|^2, \tag{3.73}$$

where we assume $\hbar = 1$. This can be rewritten as

$$p_t(i,j) = \left|\sum_{\ell=1}^{3N}\langle i|\hat{\Pi}_\ell|j\rangle e^{-i\lambda_\ell t}\right|^2 \leq \sum_{\ell=1}^{3N}\left(\langle i|\hat{\Pi}_\ell|j\rangle\right)^2 =: p_{max}(i,j), \tag{3.74}$$

in which we used the spectral decomposition for the Hamiltonian (3.55) as

$$\hat{H}_{el} = \sum_{\ell=1}^{3N}\lambda_\ell\hat{\Pi}_\ell. \tag{3.75}$$

The upper bound in the above summations of our present case with two molecules is 6. The maximum transition probability $p_{max}(i,j)$ is referred also to information transfer fidelity (ITF) and obviously $p_{\max}(i,j) \leq 1$. By analyzing (3.74), we found the following results:

- $p_t(1,2)$ attains the value 1 under the condition $\dfrac{L}{J} = \dfrac{2\sqrt{2}(2q+1)}{2p+1}$ with $p, q \in \mathbb{Z}$.

- $p_t(1,6)$ attains the value 1 under the condition of $\frac{L}{J} = \frac{\sqrt{2}(2q+1)}{2p+1}$ with $p, q \in \mathbb{Z}$.

All above calculations can be also done for the periodic condition on $\alpha$, i.e. the Hamiltonian (3.50) for two atoms becomes

$$\begin{aligned} \hat{H}_{el} &= -J\Big(\hat{B}^{\dagger}_{1,1}\hat{B}_{2,1} + \hat{B}^{\dagger}_{1,2}\hat{B}_{2,2} + \hat{B}^{\dagger}_{1,3}\hat{B}_{2,3} + H.c\Big). \\ &+ L\Big(\hat{B}^{\dagger}_{1,1}\hat{B}_{1,2} + \hat{B}^{\dagger}_{2,1}\hat{B}_{2,2} + \hat{B}^{\dagger}_{1,2}\hat{B}_{1,3} + \hat{B}^{\dagger}_{2,2}\hat{B}_{2,3} \\ &+ \hat{B}^{\dagger}_{1,3}\hat{B}_{1,1} + \hat{B}^{\dagger}_{2,3}\hat{B}_{2,1} + H.c\Big). \end{aligned} \tag{3.76}$$

Its matrix representation in the basis $\{|k\rangle\}_{k=1}^{6}$ reads

$$\hat{H}_{el} = \begin{pmatrix} 0 & -J & L & 0 & L & 0 \\ -J & 0 & 0 & L & 0 & L \\ L & 0 & 0 & -J & L & 0 \\ 0 & L & -J & 0 & 0 & L \\ L & 0 & L & 0 & 0 & -J \\ 0 & L & 0 & L & -J & 0 \end{pmatrix} \tag{3.77}$$

with eigenvalues $\{-J-L, -J-L, J-L, J-L, -J+2L, J+2L\}$.

By analyzing (3.74) with the spectral decomposition of (3.77), we found just the following result:

- $p_t(1,2)$ attains the value 1 under the condition $\frac{L}{J} = \frac{4q}{3(2p+1)}$ with $p, q \in \mathbb{Z}$.

Then we expanded the spin network with the boundary (3.54) to $N$ molecules with three channels $\alpha = 1, 2, 3$ and found PST is less than 1 for $N > 3$. Therefore, we decided to change the boundary condition on the molecule $n$ and channel $\alpha$. The more details are reported in the next section.

### 3.3 Information transfer in a macromolecule with $N$ molecules

In another manner, we simplify the treatment by restricting our attention to the single excitation subspace of the Hamiltonian (3.50) as $H_{el} = span\{|n\rangle\}_{n=1}^{N} \bigotimes \{|\alpha\rangle\}_{\alpha=1}^{3}$. Here the vector $|n,\alpha\rangle = |0\rangle_{1,1}|0\rangle_{1,2}\ldots|1\rangle_{n,\alpha}\ldots|0\rangle_{N,3}$ indicates the presence of excitation in the $n$th molecule and $\alpha$th channel. In this new basis, the system is described by a $3N \times 3N$ matrix.

Using this basis, the Hamiltonian describing the system is represented by the matrix

$$\hat{H}_{el} = \begin{pmatrix} \mathbf{C}_0^0 & \mathbf{C}_1^0 & \mathbf{C}_2^0 & \cdots & \mathbf{C}_{N-1}^0 \\ \mathbf{C}_0^1 & \mathbf{C}_1^1 & \mathbf{C}_2^1 & \cdots & \mathbf{C}_{N-1}^1 \\ \vdots & & \ddots & \cdots & \vdots \\ \mathbf{C}_0^{N-1} & \mathbf{C}_1^{N-1} & \mathbf{C}_2^{N-1} & \cdots & \mathbf{C}_{N-1}^{N-1} \end{pmatrix}, \tag{3.78}$$

in which $\mathbf{C}_m^n$ (with $m, n = 0, \cdots N-1$) are $3 \times 3$ matrices which depend on the boundary conditions.

**closed boundary on both $n$ and $\alpha$**

Here, we aim to consider the special case of the close boundaries on both $n$ and $\alpha$ (see Fig. 3.5). Restricted to the single excitation subspace, the Hamiltonian of the system becomes a block circulant matrix with circulant blocks from the ordered set $\{\mathbf{C}_0^0, \mathbf{C}_1^0, ..., \mathbf{C}_{N-1}^0\}$. Therefore, $\hat{H} = \text{circ}(\mathbf{C}_0^0, \mathbf{C}_1^0, ..., \mathbf{C}_{N-1}^0) \in \mathcal{BC}_{\alpha,N}$ is a $N \times N$ block circulant matrix with $\alpha \times \alpha (\alpha = 3)$ circulant generating matrices

$$\mathbf{C}_0^0 = \begin{pmatrix} 0 & L & L \\ L & 0 & L \\ L & L & 0 \end{pmatrix}; \quad \mathbf{C}_1^0 = \mathbf{C}_{N-1}^0 = \begin{pmatrix} J & 0 & 0 \\ 0 & J & 0 \\ 0 & 0 & J \end{pmatrix} \tag{3.79}$$

and $\mathbf{C}_2^0 = \mathbf{C}_3^0 = ... = \mathbf{C}_{N-2}^0 = 0$. Then the Hamiltonian $\hat{H}$ has the matrix form

$$\hat{H}_{\text{el}} = \begin{pmatrix} \mathbf{C}_0^0 & \mathbf{C}_1^0 & 0 & \cdots & \mathbf{C}_{N-1}^0 \\ \mathbf{C}_{N-1}^0 & \mathbf{C}_0^0 & \mathbf{C}_1^0 & & 0 \\ 0 & \mathbf{C}_{N-1}^0 & \ddots & \ddots & \vdots \\ \vdots & & \ddots & & \mathbf{C}_1^0 \\ \mathbf{C}_1^0 & 0 & \cdots & \mathbf{C}_{N-1}^0 & \mathbf{C}_0^0 \end{pmatrix}. \tag{3.80}$$

The eigenvalues of $\hat{H}_{el}$ are found to be [40]

$$\lambda_n^\alpha = 2J \cos\left(\frac{2\pi n}{N}\right) - 2e^{i\alpha\pi} L \cos\left(\frac{\pi}{3}(\alpha - 1)\right), \tag{3.81}$$

in which $\lambda_n^\alpha$ is the $\alpha$th diagonal element of the $n$th $3\times 3$ block for $n = 0, 1, 2, ..., N-1$ and $\alpha = 1, 2, 3$. Moreover, the eigenvectores of $\hat{H}_{el}$ are the columns of the matrix $W = \rho \otimes V$ where $\rho$ is a $N \times N$ Fourier Matrix and $V$ is a $3\times 3$ Fourier Matrix [40]. So, we can write the normalized eigenvectores briefly as

$$W_n^\alpha = \frac{1}{\sqrt{3N}}\Big(\rho_n^{-1}V_\alpha, V_\alpha, \rho_n V_\alpha, \rho_n^2 V_\alpha, ..., \rho_n^{N-2}V_\alpha\Big)^T \tag{3.82}$$

where $\rho_n = e^{i2\pi n/N}; (n = 0, 1, ..., N-1)$ is the $N$-th Root of Unity and $V_\alpha$ is defined as

$$\vec{V}_1 = \Big(1, 1, 1\Big)^T, \quad \vec{V}_2 = \Big(e^{-\frac{2i\pi}{3}}, 1, e^{\frac{2i\pi}{3}}\Big)^T, \quad \vec{V}_3 = \Big(e^{\frac{2i\pi}{3}}, 1, e^{-\frac{2i\pi}{3}}\Big)^T. \tag{3.83}$$

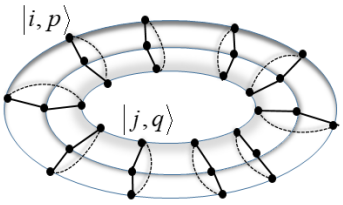


Figure 3.5 Close boundaries on both $N$ molecules and $\alpha = 3$ channels.

**Eigendecomposition of the Hamiltonian**

We first point out that according to (3.81), the eigenvalues corresponding to $\alpha = 2$ and $\alpha = 3$ are equal, i.e., $\lambda_n^2 = \lambda_n^3$. This allows us to discuss the problem that eigenvalues of the Hamiltonian for only two categories corresponding to $\alpha = 1$ and $\alpha = 2$ (or 3).
We begin by considering the case $\alpha = 1$:

- If $N$ is even, but not divisible by 4, we have $\lambda_n^1 = \lambda_{N-n}^1 = -\lambda_{N/2-n}^1 = -\lambda_{N/2+n}^1 \neq 0$, which means there are $\frac{N}{2}-1$ distinct pairs of double eigenvalues and two single eigenvalues $\pm 2J + 2L$ for $n = 0$ and $n = \frac{N}{2}$ giving totally $\tilde{N} = \frac{N}{2} + 1$ pairwise distinct eigenvalues:

$$\{-2J + 2L, \lambda_n^1, 2J + 2L : n = 1, 2, ..., \frac{N}{2} - 1\}. \tag{3.84}$$

  In this case, if $N$ is divisible by 4, there is also a double eigenvalues at 0 for $n = \frac{N}{4}$ and $\frac{3N}{4}$ giving totally $\tilde{N} = \frac{N}{2} + 2$ pairwise distinct eigenvalues.

- If $N$ is odd, $\lambda_n^1 = \lambda_{N-n}^1 \neq 0$ and there are $(N-1)/2$ distinct pairs of double eigenvalues and

a single eigenvalue $2J+2L$ at $n=0$ which is totally $\tilde{N}=(N+1)/2$ distinct eigenvalues:

$$\{\lambda_n^1, 2J+2L : n=1,2,...,\frac{N-1}{2}\}. \tag{3.85}$$

On the other hand, for the cases $\alpha=2$ (and/or $\alpha=3$), we have:

- If $N$ is even, but not divisible by 4, we have $\lambda_n^\alpha=\lambda_{N-n}^\alpha=-\lambda_{N/2-n}^\alpha=-\lambda_{N/2+n}^\alpha\neq 0$ and so $\frac{N}{2}-1$ distinct pairs of the double eigenvalues and two single eigenvalues $\pm 2J-L$ giving totally $\tilde{N}=\frac{N}{2}+1$ pairwise distinct eigenvalues:

$$\{-2J-L, \lambda_n^\alpha, 2J-L : \alpha=2 \quad (\text{or} \quad 3) \quad \text{and} \quad n=1,2,...,\frac{N}{2}-1\}. \tag{3.86}$$

  If $N$ is divisible by 4, a double eigenvalue at 0 for $n=\frac{N}{4}$ and $\frac{3N}{4}$ giving totally $\tilde{N}=\frac{N}{2}+2$ pairwise distinct eigenvalues.

- If $N$ is odd, $\lambda_n^\alpha=\lambda_{N-n}^\alpha\neq 0$, we have $(N-1)/2$ distinct pairs of double eigenvalues and a single eigenvalue $2J-L$ at $n=0$ which is totally $\tilde{N}=(N+1)/2$ distinct eigenvalues:

$$\{\lambda_n^\alpha, 2J-L : \alpha=2 \quad (\text{or} \quad 3) \quad \text{and} \quad n=1,2,...,\frac{N-1}{2}\} \tag{3.87}$$

Now we are in a position to construct the eigendecomposition of the Hamiltonian [39]. To this end, we first define for the both even and odd $N$, the eigenprojection on the corresponding double eigenvalue $\lambda_n^\alpha=\lambda_{N-n}^\alpha$ to be as $\prod_n^\alpha := |W_n^\alpha\rangle\langle W_n^\alpha| + |W_{N-n}^\alpha\rangle\langle W_{N-n}^\alpha|$. Also, we consider the eigenprojection of the eigenvalue at $n=0$ as $\prod_0^\alpha := |W_0^\alpha\rangle\langle W_0^\alpha|$. Finally, if $N$ is even, the eigenprojection of the eigenvalue at $n=N/2$ is $\prod_{N/2}^\alpha := |W_{N/2}^\alpha\rangle\langle W_{N/2}^\alpha|$ and further, if $N$ is divisible by 4, then we define also $\prod_{N/4}^\alpha := |W_{N/4}^\alpha\rangle\langle W_{N/4}^\alpha| + |W_{3N/4}^\alpha\rangle\langle W_{3N/4}^\alpha|$ for the corresponding eigenvalues at $n=N/4$ and $n=3N/4$. Cautiously, by using the above definitions for the involved eigenprojections, we study the eigenprojections for three channels ($\alpha=1,2,3.$) separately. With this notation, the spectral decomposition for the Hamiltonian (3.80) will be

$$\hat{H}_{el}=\sum_{n=0}^{\tilde{N}-1}\sum_{\alpha=1}^{3}\lambda_n^\alpha\prod_n^\alpha. \tag{3.88}$$

Now, to study the maximum transfer fidelity (3.74) for our $3N$-qubit system, suppose the single excitation initially resides in the $i$th qubit at channel $p$, $|i,p\rangle$ with $i \in \{0,1,\cdots,N-1\}$ and $p \in \{1,2,3\}$. Then the single excitation assumption allows only the transitions of the from $|i,p\rangle \leftrightarrow |j,q\rangle$. Therefore, from [39] and (3.73), it seems quite logical to define the transition probability from state $|i,p\rangle$ into $|j,q\rangle$ as follow

$$p_t([i,p],[j,q]) = |\langle i,p|e^{-i\hat{H}_{\rm el}t}|j,q\rangle|^2. \tag{3.89}$$

Using the spectral decomposition (3.88), the above relation can be written as

$$p_t([i,p],[j,q]) = \left|\sum_{n=0}^{\tilde{N}-1}\sum_{\alpha=1}^{3}\langle i,p|\prod_{n}^{\alpha}|j,q\rangle e^{-i\lambda_n^\alpha t}\right|^2. \tag{3.90}$$

Now assume there exists $t$ such that the phase factor $e^{-i\lambda_n^\alpha t}$ can be written as

$$e^{-i\lambda_n^\alpha t} = s_n^\alpha([i,p],[j,q])e^{i\phi}, \quad \forall n = 0,...,N-1, \quad \text{and} \quad \alpha = 1,2,3, \tag{3.91}$$

where $s_n^\alpha([i,p],[j,q]) := \mathrm{Sgn}(\langle i,p|\prod_{n}^{\alpha}|j,q\rangle) \in \{0,\pm 1\}$ is a sign factor and $\phi$ is an arbitrary global phase which must be the same for all $n$'s and $\alpha$'s. The upper bound for the transition probability or ITF is obtained as follow

$$p_{\max}([i,p],[j,q]) = \Big(\sum_{n=0}^{\tilde{N}-1}\sum_{\alpha=1}^{3}|\langle i,p|\prod_{n}^{\alpha}|j,q\rangle|\Big)^2. \tag{3.92}$$

There is no need to mention that $p_{\max}([i,p],[j,q]) \leq 1$.

According to Eq. (3.91), there exists eigenspaces with $s_n^\alpha([i,p],[j,q]) = 0$ which means there is no overlap between the input state $|i,p\rangle$ and the target state $|j,q\rangle$. They do not possess any contribution in the sum (3.92), thus they can be removed from the summation. We refer them as *dark-state* subspaces. Then we can limit ourselves to the $K' \subseteq \{0,1,...,\tilde{N}-1\}$ of indices $n$ for which $s_n^\alpha([i,p],[j,q]) \neq 0$. We point out that for all members of set $K'$ we have $s_n^\alpha = \pm 1$ (for all $n \in K'$). In order to arrive at the dark states of our $3N$-qubit system, we should study the sign factors if $s_n^\alpha([i,p],[j,q]) = 0$. We must study the sign factors for $\alpha = 1,2,3$ separately. According to the Eq. (3.82) and eigenprojections explained above Eq. (3.88), we point out that

for $n = 0$, we have

$$\begin{aligned}
\langle i,p|\Pi_0^1|j,q\rangle &= 1/3N \neq 0,\\
\langle i,p|\Pi_0^2|j,q\rangle &= e^{2i(p-q)\pi/3}/3N \neq 0,\\
\langle i,p|\Pi_0^3|j,q\rangle &= e^{2i(q-p)\pi/3}/3N \neq 0.
\end{aligned} \tag{3.93}$$

This means there is no dark state with respect to $n = 0$ for any value of $\alpha$. Also, for an even $N$, it is straightforward to illustrate the following relation for the case $n = N/2$:

$$\begin{aligned}
\langle i,p|\Pi_{N/2}^1|j,q\rangle &= (-1)^{(i-j)}/3N \neq 0,\\
\langle i,p|\Pi_{N/2}^2|j,q\rangle &= (-1)^{(i-j)}e^{2i(p-q)\pi/3}/3N \neq 0,\\
\langle i,p|\Pi_{N/2}^3|j,q\rangle &= (-1)^{(i-j)}e^{2i(q-p)\pi/3}/3N \neq 0.
\end{aligned} \tag{3.94}$$

Therefore, there is no dark state associated with $n = N/2$ for an even $N$. Furthermore, we have

$$\begin{aligned}
\langle i,p|\Pi_n^1 + \Pi_{N-n}^1|j,q\rangle &= 2\cos\left(2\pi n(j-i)/N\right)/3N,\\
\langle i,p|\Pi_n^2 + \Pi_{N-n}^2|j,q\rangle &= 2\cos\left(2\pi n(j-i)/N\right)e^{2i(p-q)\pi/3}/3N,\\
\langle i,p|\Pi_n^3 + \Pi_{N-n}^3|j,q\rangle &= 2\cos\left(2\pi n(j-i)/N\right)e^{2i(q-p)\pi/3}/3N,
\end{aligned} \tag{3.95}$$

for $n = 1, ..., \lceil (N-2)/2 \rceil$. According to the relations (3.95), it is obvious that for all values of $\alpha$, there are dark states if $\cos\left(2\pi n(j-i)/N\right) = \cos\left(m\pi/2\right) = 0$ with $m$ an odd integer. Thus, we can say that the divisibility of $N$ by 4 is a necessary but not sufficient condition to have dark states due to the term $(j-i)$.

Our both analytical and numerical computations shows that $p_{max}([i,p],[j,q])$ in (3.92) is always 1 ( independent on input and output qubits) due to the fact that the analytical eigenvectors of the Hamiltonian are the Kronecker product of two Fourier matrices (3.82) where each element of the eigenvectors has the same structure as $e^{i\phi}/\sqrt{3N}$, in which $\phi$ is a phase. This results in a value of 1 for the $p_{max}$.

Our numerical simulations for the different input and output states shows that the maximum of the transition probability (3.90) is always less than 1.

Bellow, we bring some numerical examples and discuss ITF of the network. Note that to avoid the probable dark states as mentioned above, we are motivated to study the networks with $N$ not divisible by 4. Here we choose an even $N = 10$ and an odd $N = 9$.

**Example 1** We study ITF (3.90) for the system with $N = 10$ and $\alpha = 1, 2, 3$. We consider the different input and output states shown in 3D-plots vs time $\tau = Lt$ and $J/L$ in Figs.(3.6) and (3.7). As a first conclusion from the plots of Fig. (3.6) we can see the maximum probability $p_t$ is higher when the in and out nodes are in the same channel (same $\alpha$) where $p([0,1],[5,1])$ in panel $(e)$ enjoys the highest ITF about 0.9 because the nodes are diametrically opposed. Second, from Fig. (3.6) we can observe that in a short time after the interaction, the amplitude of $p_t$ gets higher for larger amount of $J/L$. Equivalently, from Fig. (3.7) it is observed the higher amplitude $p_t$ occurs for the smaller $J/L$ in a first short time of interaction for the transmission to the other channels. Third, from the panel $(a)$ of Fig. (3.7) we conclude that the higher probability is also appeared when the input and output states are in the same molecule $n = 0$ (namely two different channels within the same molecule), however in panels $(b)$,$(c)$,$(d)$ and $(e)$ $p_t$ decreases around $0.15 - 0.2$ for the transmissions with the different molecules and channels. Suddenly, we can see the probability $p([0,1],[5,2])$ becomes higher about 0.35 in panel (f) ( since of diametrically opposition of in and out qubits). Moreover, because of the closed boundary on both $n$ and $\alpha$ all above considered probabilities are equivalent with

$$
\begin{aligned}
&p_t([0,1],[1,2]) = p_t([0,1],[1,3]) = p_t([0,1],[9,2]) = p_t([0,1],[9,3]),\\
&p_t([0,1],[2,2]) = p_t([0,1],[2,3]) = p_t([0,1],[8,2]) = p_t([0,1],[8,3]),\\
&p_t([0,1],[3,2]) = p_t([0,1],[3,3]) = p_t([0,1],[7,2]) = p_t([0,1],[7,3]),\\
&p_t([0,1],[4,2]) = p_t([0,1],[4,3]) = p_t([0,1],[6,2]) = p_t([0,1],[6,3]),\\
&p_t([0,1],[1,1]) = p_t([0,1],[9,1]),\\
&p_t([0,1],[2,1]) = p_t([0,1],[8,1]),\\
&p_t([0,1],[3,1]) = p_t([0,1],[7,1]),\\
&p_t([0,1],[4,1]) = p_t([0,1],[6,1]),\\
&p_t([0,1],[0,2]) = p_t([0,1],[0,3]),\\
&p_t([0,1],[5,2]) = p_t([0,1],[5,3]).
\end{aligned}
\tag{3.96}
$$

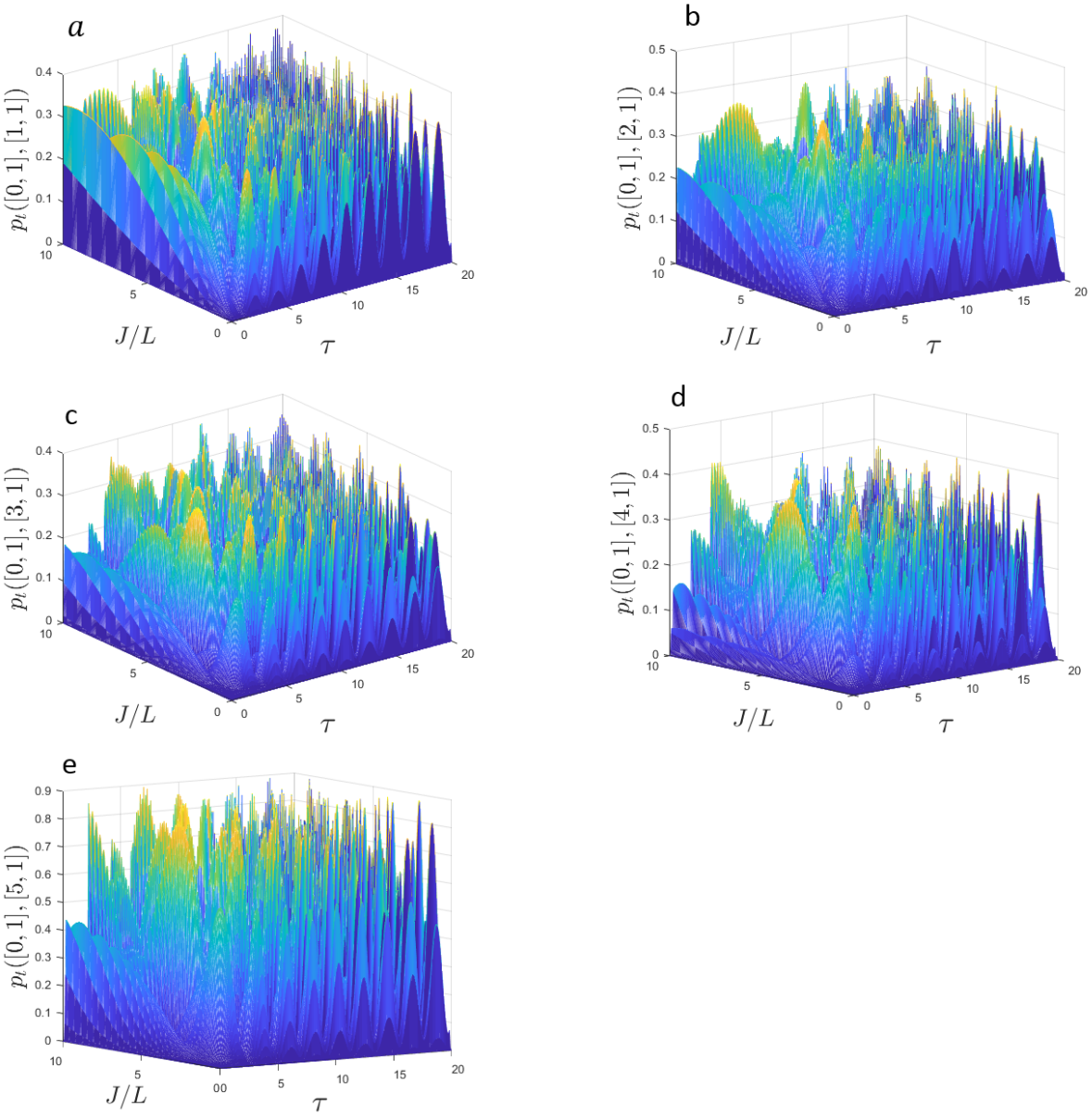


Figure 3.6 The transition probability $p_t$ between the in and out nodes with the same channels for a lattice with $N = 10$.

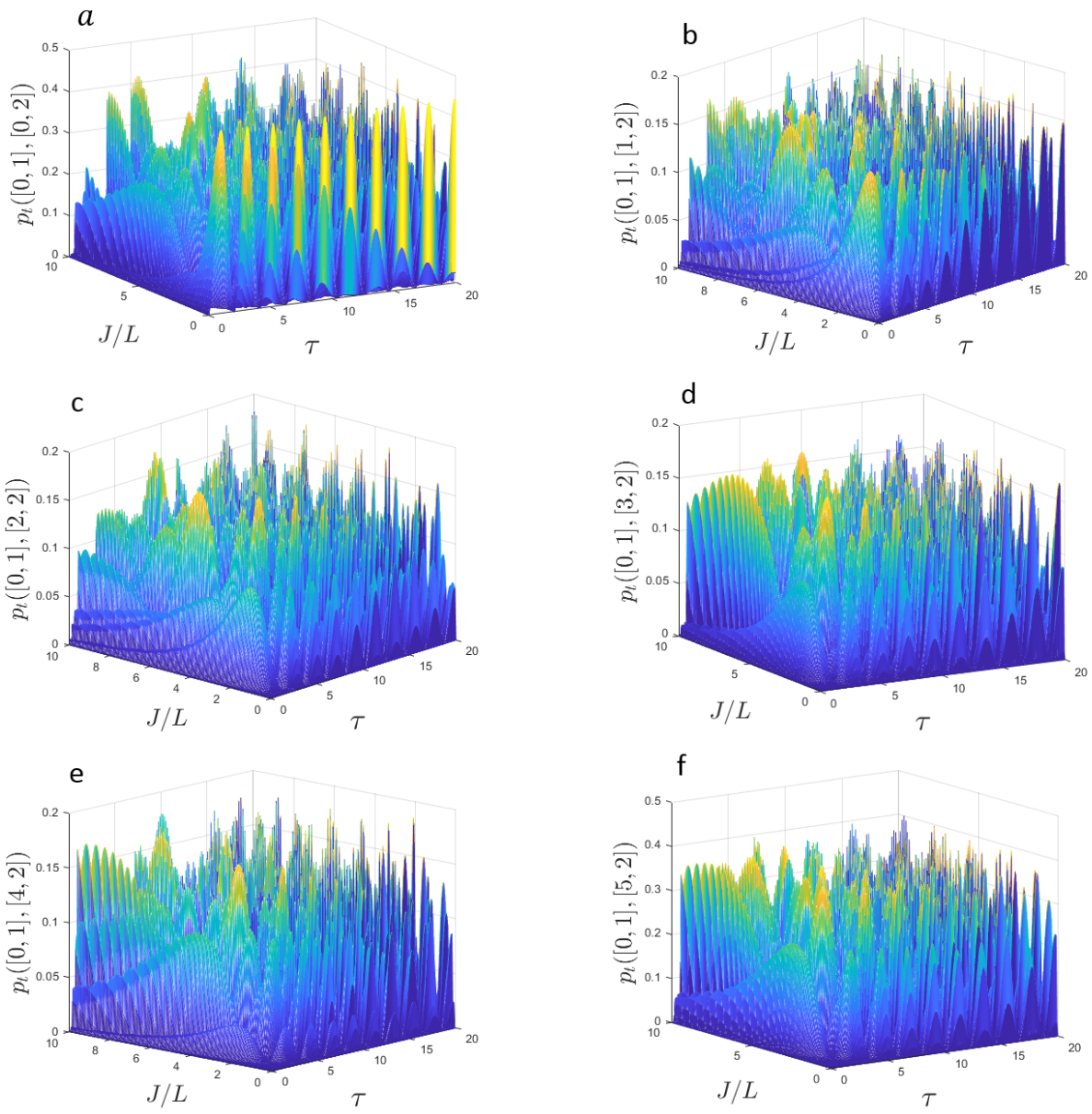


Figure 3.7 The transition probability $p_t$ between the in and out nodes with the different channels for a lattice with $N = 10$.

**Example 2** Now we consider a spin network with $N = 9$ and study ITF in 3D dimensional plots displayed in Figs. (3.8) and (3.9). As it is seen in Fig. (3.8), the amplitude of transition probability $p_t$ is about 0.35 between the input and output states with the same channel $\alpha$. Note that in this case ( odd N) the in and out nodes can not be diametrically opposed and that is why $p_t$ is lower. By changing the channels in Fig. (3.9), the highest probability around 0.5 is found in panel $(a)$ for $p_t([0,1],[0,2])$ with the same molecule $n = 0$; however, transmission

from $|0,1\rangle$ to other sites with the various molecules and channels in panels (b), (c), (d) and (e) are low about 0.15. Moreover, like what we reported in example 1, here in Fig. (3.8) to have maximum $p_t$ at first short time we need higher $J/L$ for the transmission to the same channels and lower $J/L$ for the transmission to the other channels shown in Fig. (3.9). Because of the closed boundary on both $n$ and $\alpha$ we have also

$$
\begin{aligned}
&p_t([0,1],[1,2]) = p_t([0,1],[8,2]) = p_t([0,1],[8,3]) = p_t([0,1],[1,3]),\\
&p_t([0,1],[2,2]) = p_t([0,1],[7,2]) = p_t([0,1],[2,3]) = p_t([0,1],[7,3]),\\
&p_t([0,1],[3,2]) = p_t([0,1],[6,2]) = p_t([0,1],[3,3]) = p_t([0,1],[6,3]),\\
&p_t([0,1],[4,2]) = p_t([0,1],[4,3]) = p_t([0,1],[5,3]) = p_t([0,1],[5,2]),\\
&p_t([0,1],[1,1]) = p_t([0,1],[8,1]),\\
&p_t([0,1],[2,1]) = p_t([0,1],[7,1]),\\
&p_t([0,1],[3,1]) = p_t([0,1],[6,1]),\\
&p_t([0,1],[4,1]) = p_t([0,1],[5,1]),\\
&p_t([0,1],[0,2]) = p_t([0,1],[0,3]).
\end{aligned}
\tag{3.97}
$$

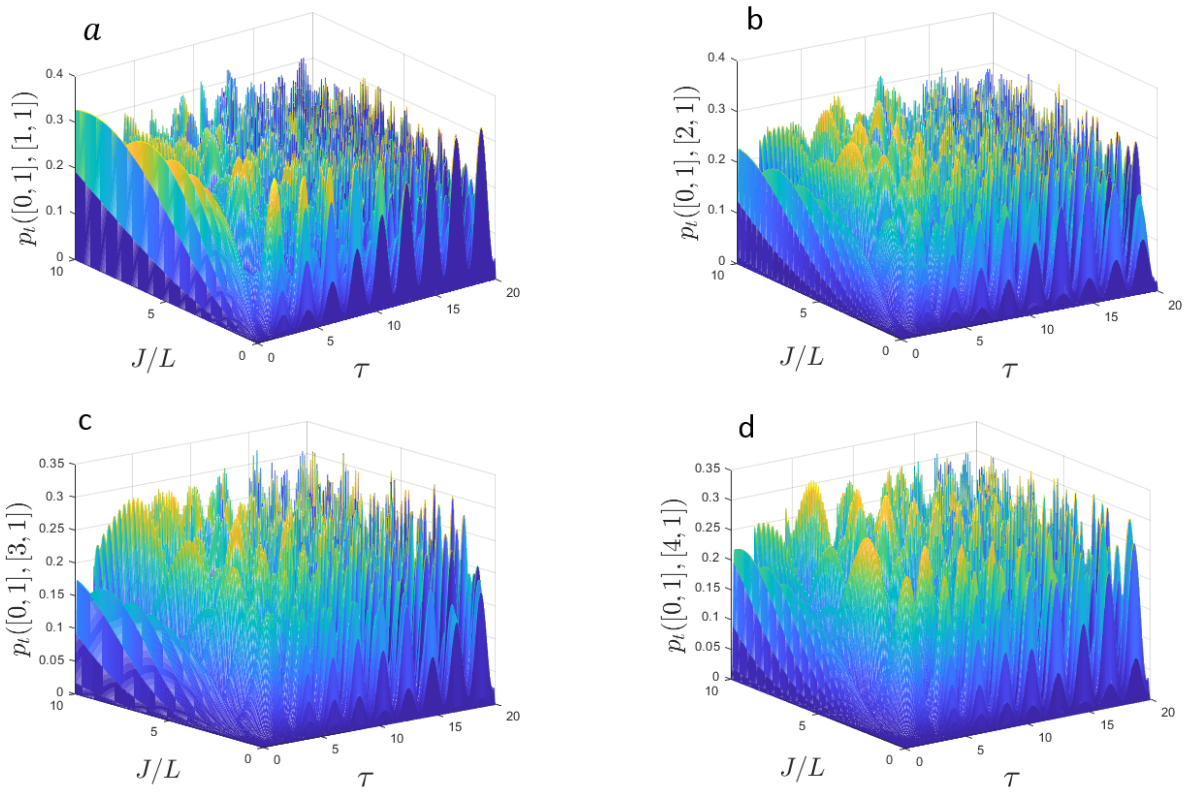


Figure 3.8 The transition probability $p_t$ between the in and out nodes with the same channels for a lattice with $N = 9$.

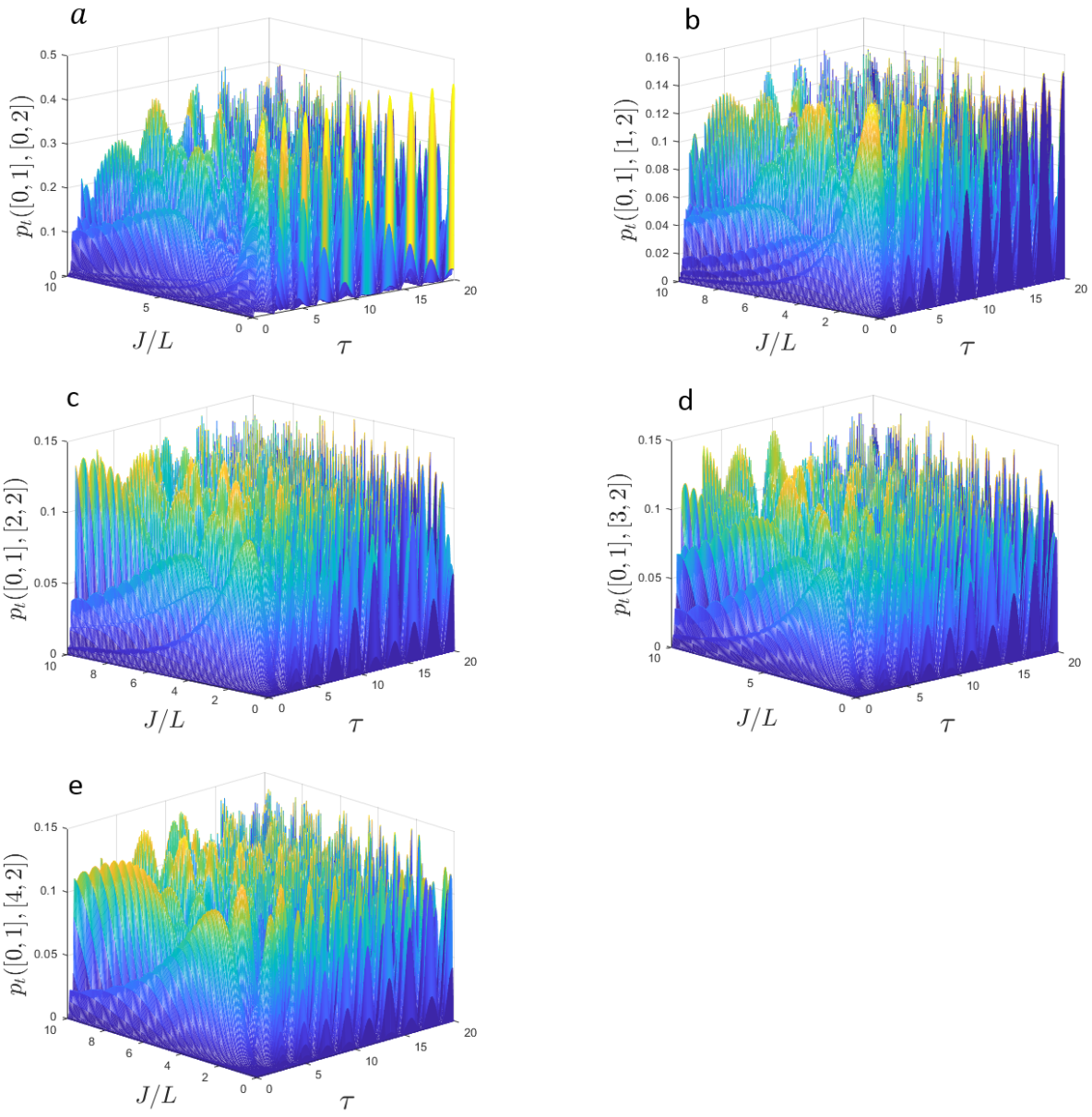


Figure 3.9 The transition probability $p_t$ between the in and out nodes with the different channels for a lattice with $N = 9$.

All in all, in examples 1 with even $N = 10$, ITF is around 0.9 while in example 2 with odd $N = 9$ there is not such an impressive high transition probability. However, in these two examples it is observed that $p_t$ is almost high around 0.5 by transferring between two nodes with the same molecule $n = 0$ (namely two different channels within the same molecule). It sounds also that $p_t$ has higher amplitude at the first short time with larger $J/L$ for transmissions to the same channel $\alpha$. Equivalently, the amplitude is higher at a short interval of time for smaller amount of $J/L$ for the transmission to other channels.

# CHAPTER 4. Interactions among biomolecules

In this chapter, short range interactions that are important biological reactions between biomolecules but insufficient on long ranges are presented. Then a review of selective long range electrodynamic interactions among biomolecules is reported. Main background of ongoing researches are presented; in particular some main aspect of the so called Fröhlich condensation (the analogous of Bose-Einstein condensation for out-of-thermal-equilibrium systems) are recalled in relation to the possibility of activating such long range interactions among biomolecules. Moreover, the resonant recognition model (RRM) is introduced which presents selective protein interactions relevant to their biological function, i.e., interaction with its target (other protein, DNA regulatory segment or small molecule). RRM is capable to calculate the frequencies from periodicities within the distribution of energy of delocalised electrons along protein and DNA molecules using charge velocity through these macromolecules.

## 4.1 Intermolecular interactions

Molecular interaction includes forces of attraction or repulsion which act between atoms and other types of neighboring particles, e.g. atoms or ions. In order to define long-range and short-range interactions, we recall an interaction potential $V(r)$ where $r$ is the distance between interacting particles in a $d$-dimensional space. The interaction is short-range if

$$\lim_{|V(r)|\to+\infty} V(\mathbf{r})r^d < +\infty, \tag{4.1}$$

otherwise if this limit diverges in the same conditions, the potential is long-range

$$\lim_{|V(r)|\to+\infty} V(\mathbf{r})r^d > +\infty. \tag{4.2}$$

### 4.1.1 Steric interactions

Steric repulsion refers to the arrangement of atoms in a molecule. If atoms are brought too close together, apparently they will suddenly experience an infinite repulsive force. This effect is attributed due to overlapping of electron clouds (Pauli or Born repulsion) and may affect the molecule's conformation and reactivity. Steric repulsion ia also known as Steric exclusion or hard core repulsion. The repulsion force is characterized in a very short range and its intensity increases where two atoms or molecules approach each other. Several repulsive potential laws are empirically used to model this phenomenon. The first option is a hard wall/core/sphere potential with a singularity at zero

$$U_{hs}(\mathbf{r}) = \begin{cases} \infty & \text{if } r \leq R \\ 0 & \text{if } r > R \end{cases} \tag{4.3}$$

where $R$ is the radius of the hard sphere [41].
Other repulsive potential is a power-law one with a large integer exponent $n_{pw}$ ( between 9 and 16)

$$U_{pw}(\mathbf{r}) = C_{pw} r^{-n_{pw}} \tag{4.4}$$

and finally an exponential potential

$$U_{exp}(\mathbf{r}) = C_{exp} e^{-r/r_{exp}} \tag{4.5}$$

where $r_{exp} \simeq 0.02$ nm and $C_{pw}$ and $C_{exp}$ are adjustable constants.

### 4.1.2 Van der Waals forces

Van der Waals interactions are highly distance dependent and occur when two neutral atoms or molecules approach enough and polarize each other resulting in a correlation between the atomic states with an action range in the order of few Angstroms. These forces is explained by Quantum mechanics and quantum electrodynamics. In quantum mechanics, each atom or molecule has its own wave functions describing its electron distribution. The quantum basis of interaction is that two atoms or molecules are correlated to each other as dipoles, each

atom or molecule's dipolar electric field shining out as $1/r^3$ with distance $r$ from the center. The average of this dipole interaction is considered zero when taken over the set of electron positions of the isolated atoms. However when the electron distributions of the isolated-atom are themselves perturbed by each other's dipolar fields, "second-order perturbation" makes the extra energy as the interaction potential proportionally as $1/r^6$ at separations $r$ much greater than dipole size. Van der waals forces includes three kinds of dipole-dipole interactions due to similar mechanism involving instantaneous coupling among fluctuating electric dipole moments or induced polarization effects:

- *Keesom's interactions* These forces originate from the classical attraction between two permanent dipoles whose orientated fluctuations are due to thermal noise. Dipole-dipole electrostatic interaction known as *Keesom's interactions* tends to correlate the orientation of the molecules:

$$U_{Keesom}(\mathbf{r}) = -\frac{\mu_1\mu_2}{24k_BT\pi^2\epsilon_0^2\epsilon_r^2r^6} \tag{4.6}$$

  where $\mu_i, i = 1, 2$ are the dipole moments of two particles, $\epsilon_0$ is the permitivity of free space, $\epsilon_r$ is dielectric constant of surrounding material, $k_B$ is the Boltzmann constant, $T$ is temperature and $r$ is the separation between particles.

- *Debye interactions* are classical inductive effects among permanent dipoles and the dipolar moment induced by them in a non polar molecule [42]. The Debye potential is given by

$$U_{Debye}(\mathbf{r}) = -\frac{\mu_1^2\alpha_2 + \mu_2^2\alpha_1}{\epsilon_r^2r^6} \tag{4.7}$$

  where $\alpha_i, i = 1, 2.$ are the polarizibilities of the two molecules.

- *London's dispersion interactions* among two non polar molecules with polarizabilities $\alpha_i$ and first ionization energies corresponding to $\hbar\nu_i$ [43, 44]. The dispersion interactions potential is given by

$$U_{London}(\mathbf{r}) = -\frac{3h\nu_1\nu_2\alpha_1\alpha_2}{32\pi^2\epsilon_0^2(\nu_1+\nu_2)r^6} \tag{4.8}$$

  where $h$ is the Plank constant.

The van der waals forces are Generally described as a combination of the previously mentioned interactions

$$U_{van}(\mathbf{r}) = U_{Keesom}(\mathbf{r}) + U_{Debye}(\mathbf{r}) + U_{London}(\mathbf{r}) \propto 1/r^6 \tag{4.9}$$

and the corresponding force decays as $1/r^7$. The characteristic features of these forces are as follow:

- anisotropy of the interaction due to the dependence of the polarizability on the mutual orientation of the molecules.
- non-additivity property due to reflection many body effects for the fields generated by molecules.
- retardation effects, concerning the dispersive forces are due to the finite propagation time of the electromagnetic waves between two dipoles when this is comparable with the characteristic time scale of dipole fluctuations. Casimir and Poldar have shown how these effects appears on a length scale around 30 nm and the London dispersion potential decreases as $1/r^7$ for the distance larger than 100 nm [45].

### 4.1.3 Hamaker theory

An extension of the van der waals interactions is assumed from the dipole-dipole interaction of two molecules to the bodies in a macro scale by taking a summation over all of the forces between the molecules in each of the bodies involved. Hamaker derived the interaction between two spheres of radii $R_1$ and $R_2$ under two approximations: neglecting retardation effects for any distance, and ignoring many body effects (due to presence of surrounding molecules),

$$\begin{aligned} U(z; R_1, R_2) &= \frac{A}{6}\Big[\frac{2R_1R_2}{z^2-(R_1+R_2)^2} + \frac{2R_1R_2}{z^2-(R_1-R_2)^2} \\ &+ \ln\Big(\frac{z^2-(R_1+R_2)^2}{z^2-(R_1-R_2)^2}\Big)\Big] \end{aligned} \tag{4.10}$$

where $A$ is Hamaker coefficient dependent strongly on the medium of spheres surrounding and $z = r + R_1 + R_2$ wherein $r$ is the distance between the spheres surfaces. The van der waals interactions among protein are in the range $\sim 3 - 5$ Angstroms and can be considered as

contact interactions, therefor start to drive the dynamical organization in cells if this requires to go beyond random encounters between reaction partners.

### 4.1.4 Electrostatic interactions

Charged and polar groups, through forming ionic pairs, hydrogen bonds, and other less specific electrostatic interactions, impart important properties to biomolecules (DNA, RNA and proteins). The electrostatic field in biomolecules is determined by many factors of the superficial charge distribution, the presence of a solvent (water) and the ionic population of the surrounding environment. These interactions could be influenced by electric-field screening.
The electrostatic potential $\phi$ at the point $r$ generated by a charge distribution $(q_i, \mathbf{r}_i)$ is defined as

$$\phi(\mathbf{r}) = \sum_i \frac{q_i}{|\mathbf{r} - \mathbf{r}_i|} = \sum_i \frac{q_i}{r}\left[1 - \frac{2\mathbf{r}.\mathbf{r}_i}{r^2} + \left(\frac{\mathbf{r}_i}{r}\right)^2\right]^{-1/2} \tag{4.11}$$

To study the electrostatic forces on length scales much larger than the characteristic molecular dimensions, we take $\forall i, r \geq r_i$ when $r = |\mathbf{r}|$ and $r_i = |\mathbf{r}_i|$. Then Eq. (4.11) can be expanded in Taylor series as

$$\begin{aligned}\phi(\mathbf{r}) &= \sum_i \frac{q_i}{r}\left[1 + \frac{\mathbf{r}.\mathbf{r}_i}{r^2} - \frac{1}{2}\left(\frac{\mathbf{r}_i}{r}\right)^2 + \frac{3}{2}\left(\frac{\mathbf{r}.\mathbf{r}_i}{r^2}\right)^2 + \cdots\right] \\ &= \sum_i \frac{q_i}{r}\left[1 + \frac{\mathbf{r}.\mathbf{r}_i}{r^2} + \frac{1}{2}\left(3\left(\frac{\mathbf{r}.\mathbf{r}_i}{r^2}\right)^2 - \left(\frac{\mathbf{r}_i}{r}\right)^2\right) + \cdots\right].\end{aligned} \tag{4.12}$$

Then the above equation is written as

$$\phi(\mathbf{r}) = \frac{Q}{r} - \sum_{\alpha=1}^{3} \mu_\alpha \frac{\partial}{\partial x_\alpha}\left(\frac{1}{r}\right) - \frac{1}{2}\sum_{\alpha,\beta=1}^{3} M_{\alpha\beta}\frac{\partial}{\partial x_\alpha \partial x_\beta}\left(\frac{1}{r}\right) + \cdots, \tag{4.13}$$

in which

$$Q = \sum_i q_i, \quad \mu_\alpha = \sum_i q_i x_{i,\alpha} \quad \text{and} \quad M_{\alpha,\beta} = \sum_i q_i x_{i,\alpha} x_{i,\beta}; \tag{4.14}$$

where $Q$ is the total charge, the vector $\mu$ is the dipole momentum, $M$ is the quadrupole momentum tensor and $x_{i,\alpha}$ are the components of $\mathbf{r}_i$ for $\alpha = 1, 2, 3$.
Eq. (4.13) shows a multipole expansion which can be applied also to the interaction among a

set of charges $\{q_i, \mathbf{r}_i\}$ and an external electrostatic potential $\phi$ at the point $\mathbf{r}_i$ as

$$U(\mathbf{r}_i) = \sum_i q_i \phi(\mathbf{r}_i). \tag{4.15}$$

By considering $r \geq r_i$ we can substitute $\mathbf{r}_i$ for $\mathbf{r} + \mathbf{r}_i$ and we arrive at

$$\begin{aligned} U &= \sum_i q_i \left[ \phi(\mathbf{r}) + \sum_{\alpha=1}^{3} x_{i,\alpha} \frac{\partial \phi(\mathbf{r})}{\partial x_\alpha} + \frac{1}{2} \sum_{\alpha,\beta=1}^{3} x_{i,\alpha} x_{i,\beta} \frac{\partial}{\partial x_\alpha} \frac{\partial \phi(\mathbf{r})}{\partial x_\beta} \right] \\ &= \left[ Q + \sum_{\alpha=1}^{3} \mu_\alpha \frac{\partial}{\partial x_\alpha} + \frac{1}{2} \sum_{\alpha,\beta=1}^{3} M_{\alpha,\beta} \frac{\partial}{\partial x_\alpha} \frac{\partial}{\partial x_\beta} \right] \phi(\mathbf{r}). \end{aligned} \tag{4.16}$$

As it is well known the electric field is given by $\mathbf{E} = -\nabla\phi$ and so it is possible to calculate the electrostatic interaction potential among biomolecules on length scales. To this end, a system composed by a molecule $A$ characterized by a set of charges $\{q_{A,i}, \mathbf{r}_{A,i}\}$ and the electrostatic potential generated by the charge distribution $\{q_{B,i}, \mathbf{r}_{B,i}\}$ of a molecule $B$ is considered. ( $\mathbf{r}_{A,i}$ and $\mathbf{r}_{B,i}$ are defined respectively with respect to the center of mass of the molecules $A$ and $B$ and also $\mathbf{r}$ is the vector joining the mass centers of both molecules). In distance much larger than the dimensions of the two molecules $A$ and $B$, from the Eqs. (4.13) and (4.16)the electrostatic interaction potential is found as

$$\begin{aligned} U(\mathbf{r}) &= \left[ Q_A + \sum_{\alpha=1}^{3} \mu_{A,\alpha} \partial^\alpha + \frac{1}{2} \sum_{\alpha,\beta=1}^{3} M_{A,\alpha,\beta} \partial^\alpha \partial^\beta + \cdots \right] \phi(\mathbf{r}) \\ &= \left[ Q_A + \sum_{\alpha=1}^{3} \mu_{A,\alpha} \partial^\alpha + \frac{1}{2} \sum_{\alpha,\beta=1}^{3} M_{A,\alpha,\beta} \partial^\alpha \partial^\beta + \cdots \right] \\ &\times \left[ \frac{Q_B}{r} - \sum_{\gamma=1}^{3} \mu_{B,\gamma} \partial^\gamma \left( \frac{1}{r} \right) - \frac{1}{2} \sum_{\gamma,\lambda=1}^{3} M_{B,\gamma\lambda} \partial^\gamma \partial^\lambda \left( \frac{1}{r} \right) + \cdots \right] \end{aligned} \tag{4.17}$$

Eq. (4.17) shows the possibility of the long-range electrostatic interactions in vacuum in which:

- the Coulombic interaction potential between two charges $Q_1$ and $Q_2$ is

$$U_c \propto \frac{Q_A Q_B}{r} \tag{4.18}$$

- the dipole-dipole interaction potential when one of the two molecules is electrically neutral

is

$$\begin{aligned} U_{dd} &= -\sum_{\alpha,\gamma} \mu_{A,\alpha}\mu_{B,\lambda}\partial^{\alpha}\partial^{\lambda}\left(\frac{1}{r}\right) \\ &= \sum_{\alpha,\gamma} \mu_{A,\alpha}\mu_{B,\lambda}\partial^{\alpha}\partial^{\lambda}\left(\frac{\delta^{\alpha,\lambda}}{r^3} - \frac{3x^{\alpha}x^{\lambda}}{r^5}\right). \end{aligned} \tag{4.19}$$

Higher orders with $r^{-n}$ for $n > 5$ are classified in the short-range interaction potentials.

### 4.1.5 Screened electrostatic fields

Screening is the damping of electric fields by the presence of the mobile charge carriers. In the biomolecular systems, the water as the universal solvent ( in which the ions are immersed) has rather high dielectric value $\epsilon \sim 80$ at $T = 300$K. The dielectric medium of water can be considered continuous and the classical polarization field $P$ for an arbitrary small electric field in an isotropic media is

$$\mathbf{P} = \chi_e \mathbf{E}, \tag{4.20}$$

where $\chi_e$ is the electric susceptibility of the media. This polarization field is satisfied in living systems typically. For electric field generated by a charge distribution $\rho(\mathbf{r})$ we can write

$$\begin{cases} \mathbf{D}(\mathbf{r}) = \mathbf{E}(\mathbf{r}) + 4\pi\mathbf{P}(\mathbf{r}) \\ \nabla.\mathbf{D}(\mathbf{r}) = 4\pi\rho(\mathbf{r}). \end{cases} \tag{4.21}$$

From Eqs. (4.20) and (4.21) we have

$$\nabla.\mathbf{E}(\mathbf{r}) = \frac{4\pi\rho}{\epsilon}, \quad \epsilon = 1 + 4\pi\chi_e. \tag{4.22}$$

where $\epsilon$ is called the electrostatic dielectric constant. Eq. (4.22) means that the electric field is screened by $1/\epsilon$. Clearly, the electric field is more screened sufficiently when the freely moving ions are more concentrated so that the electrostatic potential $\phi(\mathbf{r})$ decaying to zero beyond a characteristic distance $\kappa^{-1}$ called Debye screening length. According to Debye and Hückle

theory the potential $\phi(\mathbf{r})$ originated by a single electric charge $q$ at the temperature $T$ is [46]

$$\phi(\mathbf{r}) = \frac{q}{\epsilon r} e^{-r/\kappa} \tag{4.23}$$

where Debye-Hückle length is

$$\kappa = \left( \frac{e^2 N_A}{\epsilon k_B T} \sum_j Z_j^2 n_j \right) \tag{4.24}$$

in which $e$ is the electronic charge, $N_A$ is the Avogadro's number, $Z_j$ is the ionic valence, $k_B$ is the Boltzmann constant and a numerical concentration $n_j$. While the electrostatic potential $\phi(\mathbf{r})$ diverges at long range, the screened potential (4.23) shows that according to the ionic strength $\sum_j n_j$ of the electrolyte solution, the electrostatic forces are small at the distance larger than $\kappa$.

## 4.2 Long range electrodynamic interactions among biomolecules

### 4.2.1 The possibility of the electrodynamic forces in long distances

In the above-mentioned section we stressed the significant progress has been made understanding interactions acting at a short distance with a typical range of a few Angstrom among biomolecules. However, the electrodynamic intermolecular interactions poorly investigated in biological systems because of the electric screening effect and the large static dielectric constant of water ($\sim 80$) at room temperature. Nevertheless, experimental evidence has generally shown the inefficiency of Debye screening on an electrolyte solution behaving like a pure dielectric, which is influenced by oscillating electric field at a frequency larger than $\sim 250$ MHz. In another word, charges/dipoles oscillate faster with no electric screening effects than a suitable frequency. Moreover, it has been proved that beyond a few hundred of GHz, the water dielectric constant has a much smaller values around $\sim 4$ than the one in the electrostatic case what enables presence of the electrodynamic forces in long distance. In another case in the out of thermal equilibrium condition, the long range interaction can be also effective where the vibrational modes of two molecules oscillate with a common frequency. Also, recently the long-range interaction due to the high polarization of water molecules in biochemical reactions has been suggested in [47]. In the following we go to the details of some of these aspects.

**Pure-dielectric behavior of electrolyte acted by high frequency oscillating electric fields:**

According to the experiments of Xammar Oro and his colleagues in 1992 [48], they applied an alternative sinusoidal tension to the electrodes of a cell containing an electrolyte solution. This can be equivalent to a parallel RC circuit where the impedance $Z$ of electrolyte, which is measured as a function of the tension frequency $\omega$, plays a role similar to a capacitive for a large $\omega$ as you see in Fig. 4.1. In this way the impedance value has the form

$$Z = \left(\frac{1}{R^2} + \omega^2 C^2\right)^{-1/2} \tag{4.25}$$

where the capacity $C = g\epsilon$ and the resistance $R = 1/g\sigma$. The frequency-dependent factors $\epsilon$ and $\sigma$ are respectively the dielectric constant and the conductivity $g$ is a geometric factor. From Eq. (4.25) it is clear that the impedance $Z = R$ when the frequency $\omega$ tends to zero which means the domination of the resistor $R_0$ on the impedance value so that the electrolyte behaves as a pure conductor. Also, the impedance $Z$ tends to zero and so electrolyte behaves like a pure dielectric (i.e., free of conducting properties) for $\omega \to +\infty$. Such a threshold frequency was originally identified by Maxwell with frequencies larger than 250 MHz.

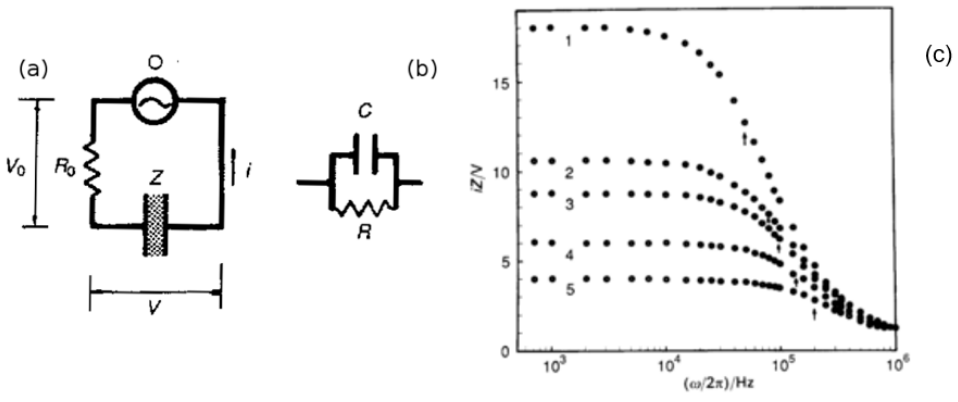


Figure 4.1 Adapted by [48]. (a) Measure circuit with the oscillator $O$, (b) the equivalent RC circuit and (c) Product of impedance $Z$ as a function of frequency $\omega$ and the current $i$ in the cell containing the electrolyte.

Fig. 4.1(c) shows the electrolyte impedance plotted versus the tension frequency $\omega$ as the experimental outcomes of Xammar Oro's. It is seen that the impedance drops noticeably for

the frequencies $\omega > 250$ MHz and reaches to zero for very high frequencies. This means that if the molecular dipoles oscillate with an higher frequency than this threshold, the electrolyte in the surrounding are not going to screen this electrodynamic field, leading to possible long range interactions.

**Dielectric constant of water subjected to high frequency electric fields:**

The water shows the different dielectric features under a large enough applied frequencies. The relative permittivity, or dielectric constant, of a material is the ratio relative of its absolute permittivity $\varepsilon(\omega)$ to the vacuum permittivity $\varepsilon_0$ as $\varepsilon_r(\omega) = \varepsilon(\omega)/\varepsilon_0$. The relative permittivity $\varepsilon(\omega)$ of a medium is a complex number because $\varepsilon(\omega)$ is related to the medium electric susceptibility $\chi_e$ which is a dimensionless constant indicating the dielectric polarization $\mathbf{P}$ of the medium is directly proportional to the applied electric field $\mathbf{E}$ as $\mathbf{P} = \varepsilon_0 \chi_e \mathbf{E}$. Then the relative permittivity is written as [49]

$$\varepsilon_r(\omega) = \varepsilon_r'(\omega) - i\varepsilon_r''(\omega) \tag{4.26}$$

where $i$ is the imaginary unit; the real part is related to the energy stored in the medium while imaginary part is related with dissipation. In the polar representation, the phase of permittivity corresponds to the phase difference among the polarization field $\mathbf{P}$ and the electric field $\mathbf{E}$. Fig. (4.2.1) displays the the theoretical and experimental results of the relative permitivity of water [50] where the both real and imaginary parts drop significantly from $\sim 80$ to $\sim 4$ for high frequencies $\sim 0.1 - 1$ THz.

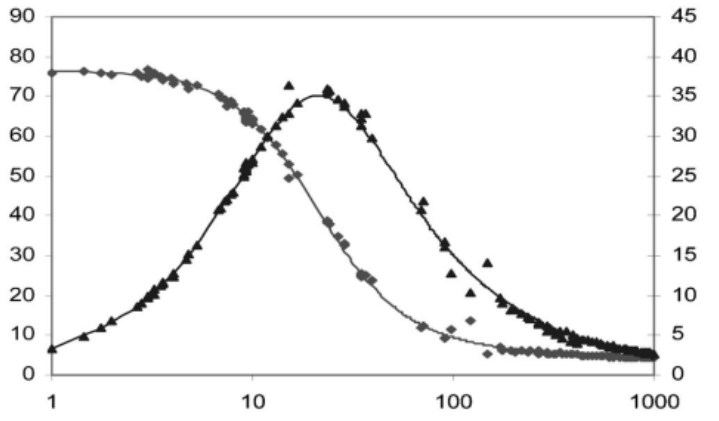


Figure 4.2 Adapted by [50]. Water permittivity at room temperature as a function of frequency (in GHz) for theoretical (line) and experimental measurement(dots). The real part of permittivity $\varepsilon'_r(\omega)$ is reported with diamonds (referred to the left axis), and the imaginary part $\varepsilon''_r(\omega)$ with triangles (referred to the right axis).

**Resonant interactions between biomolecules at thermal equilibrium:**

From the quantum electrodynamics (QED) the long range interactions between two neutral atoms have been shown to arise a resonant transition energies of them when one of the atoms is in an excited state [51, 52]. However, this leads to an entanglement, between the subsystems, which are fragile ( with lifetime $\sim 10^{-10}$ s) avoiding any quantum interactions over long distance. The same in QED, the electrodynamic interactions can be derived classically when the dipole moments of two molecules oscillate with a common frequency due to the their conformational vibrations rather than the electronic motion. Such modes, which are generally coupled among themselves, can be disintegrated in an elastic approximation as the sum of decoupled modes of the interacting systems known as normal modes.

Experimental observations have indicated the low frequency Raman and far-infrared spectra ($\sim 0.1 - 10$ THz) of equilibrium collective excitations within the biomolecules of the polar proteins and poly-nucleotides [53, 54, 55]. Besides, theoretical investigations of standard biomolecules have also presented that the many absorption peaks for many proteins occur in the this spectral domain for the collective vibrational modes in Fig (4.3) [19, 20, 56]. However, the in-phase and out-of-phase oscillations respectively of the normal modes might cancel out the long-range average effect of dipolar nature of biomolecules at thermal equilibrium. Therefore, as we will see in the next sections, an out-of-thermal equilibrium is required in order to reasonably see the

possibility of the electrodynamic interactions in long distance.

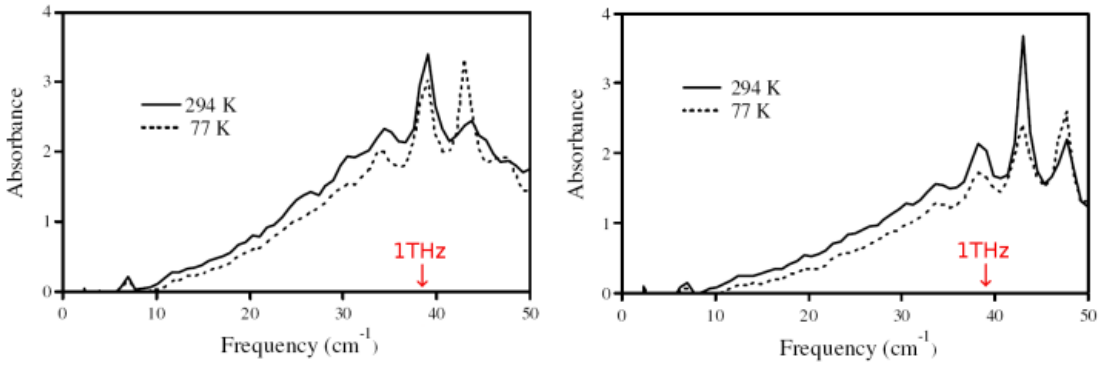


Figure 4.3 Adupted by [57]. THz absorption spectra of Lysozime (left) and myoglobine (right).

### 4.2.2 Fröhlich theory

According to the above discussion, can biomolecules be subject of such an external energy redistributed in the space of modes? The answer is Fröhlich theory [19, 20] analogous to Bose-Einstein condensation in which the cooling bosonic atoms to a very low temperature would cause bosons to fall (or condense) into the lowest accessible quantum state, resulting in a new form of matter or phase transition. Stimulated by a different attitude, however, a quiet same phenomenon to Bose condensation may happen in substances with phonons. If an external energy feeds to these modes, the energy transfers to other degrees of freedom of the substance then a stationary state will be reached in which the energy content of the electric modes is higher than in thermal equilibrium. This excess energy is found to be channeled into a lowest vibrational frequency of modes when the input energy is sufficiently large. He noticed that under these conditions, the energy supply to the substance is thus not completely thermalized but partly used in creating a strong coherent electric vibrations in the substance. This order exhibits itself long-range phase correlations.

In biological systems, the extraordinary dielectric properties are the original reasons to consider the electric modes. The thickness of the membrane of cells is about $10^{-6}$ cm maintaining a very strong dipolar layer. It is feasible that the positive and the negative part of a particular section of the membrane vibrate locally against each other leading to an oscillating electric dipole in a frequency between $10^{11}$ and $10^{12}$ Hz. Moreover, the biomolecules have the polarization properties due to the hydrogen bonds. Another explanation of the dipolar oscillations in the same

frequency region might be also because of the non-localized electrons in the same regions of the cell.

**Fröhlich rate equations**

According to the model introduced by Fröhlich, in an homogeneous system containing charged particles ( electric modes), the long wave electric oscillations are predictable with the lowest frequency $\omega_1/2\pi$ different from zero [20]. The system is assumed as a set of $N$ harmonic oscillators with frequencies $\{\omega_i\}_{i=1,2,...,N}$ with no interactions between them ( normal modes); however they are strongly coupled with the environment at temperature $T$. The energy of each mode containing $n_i$ quanta is given by $E_i = n_i\hbar\omega_i$. The exchange energy due to the emission or the absorption of a single quanta $\hbar\omega_i$ from the thermal bath is described by the term

$$\dot{n}_{i,\phi} = -\phi(T)\left(n_i e^{\hbar\omega_i/K_\beta T} - (n_i+1)\right), \tag{4.27}$$

where $K_\beta$ is the Boltzmann constant and $\phi(T)$ is the the linear coupling of $i$-th mode with the thermal bath. $\phi(T)$ depends on temperature but for simplicity its dependency on frequency $\omega_i$ is ignored. Moreover, there is an exchange energy between the branch of electric modes and thermal bath because of the relevance between the absorption energy of $\hbar\omega_i$ and the emission energy of $\hbar\omega_j$. This term is written as

$$\dot{n}_{i,\chi} = -\chi(T)\sum_j \left(n_i(1+n_j)e^{\hbar\omega_i/K_\beta T} - n_j(1+n_i)e^{\hbar\omega_j/K_\beta T}\right), \tag{4.28}$$

where $\chi(T)$ is the non-linear coupling between $i$-th and $j$-th electric modes of the system mediated by the thermal bath. Also here the dependency of $\chi(T)$ on $\omega_i$ and $\omega_j$ is neglected. Due to the conservation of the total number of oscillators, the rate equation has the relevant property $\sum \dot{n}_{i,\chi} = 0$. By providing an external source of energy to the electric modes of the system, the total supplied energy rate is

$$S = \sum_i^N \langle s_i \rangle. \tag{4.29}$$

where $\langle s_i \rangle$ is the energy supplied locally to each mode at a rate $s_i$. The rate of loss of energy from mode $i$ reads as

$$s_i = \dot{n}_i = \dot{n}_{i,\phi} + \dot{n}_{i,\chi}, \tag{4.30}$$

and then the temporal evolution $\dot{n}_i$ for the system is obtained

$$\begin{aligned} \dot{n}_i &= s_i - \phi(T)\left(n_i e^{\hbar\omega_i/K_\beta T} - (n_i+1)\right) \\ &- \chi(T)\sum_j \left(n_i(1+n_j)e^{\hbar\omega_i/K_\beta T} - n_j(1+n_k)e^{\hbar\omega_j/K_\beta T}\right). \end{aligned} \tag{4.31}$$

Fröhlich studied the condition for stationarity for each $i$ of above equation $\dot{n}_i = 0$ and found when the pumping rate of energy is zero providing the thermal equilibrium $s_i = 0$ ($\dot{n}_{i,\phi} = 0, \dot{n}_{i,\chi} = 0$), the stationary solution leads to the Plank distribution

$$n_i = \frac{1}{e^{\hbar\omega_j/K_\beta T} - 1}. \tag{4.32}$$

In the case of $s_i \neq 0$ but the non-linear coefficient $\chi = 0$, the stationary solution is given by

$$n_i = \frac{s_i + \phi}{\phi(e^{\hbar\omega_j/K_\beta T} - 1)} \tag{4.33}$$

so that the presence of an external energy supply has the only effect to increase the total number of oscillators present into the system for sufficiently high values of $S$. However, when the both $S \neq 0$ and $\chi \neq 0$, the stationarity of Fröhlich rate equation formally is obtained as follow

$$n_i = \left(1 + \frac{S}{\phi + \chi N}\right)\left[e^{\beta(\hbar\omega_i - \mu)} - 1\right]^{-1} \tag{4.34}$$

with $N = \sum_i n_i$ and

$$e^{-\beta\mu} = \frac{\phi + \chi\sum_j (1+n_j)e^{-\beta\hbar\omega_j}}{\phi + \chi N}, \tag{4.35}$$

where $\beta = 1/K_\beta T$ and $\mu \geq 0$ is an effective chemical potential. Equation (4.34) can be rewritten in the form

$$n_i = \left(1 + \frac{s_i \phi (1 - e^{-\beta\mu})}{\chi S}\right) \left[e^{\beta(\hbar\omega_i - \mu)} - 1\right]^{-1} \tag{4.36}$$

where

$$1 - e^{-\beta\mu} = \frac{\chi}{\phi} \frac{S}{\phi + \chi \sum_j n_j e^{\beta\hbar\omega_j}} \geq 0. \tag{4.37}$$

Obviously equation (4.36) requires $\hbar\omega_1 > \mu \geq 0$, where $\omega_1 = \min_{\{\omega_i\}_{i=1,2,\ldots,N}} \omega_i$, to satisfy $n_i \geq 0$ which allows to find an upper bound of $N$

$$N = \sum_i n_i < \left(1 + \frac{s_i \phi (1 - e^{-\beta\hbar\omega_1})}{\chi S}\right) \sum_i (e^{\beta(\hbar\omega_i - \mu)} - 1)^{-1}. \tag{4.38}$$

According to the original argument in Fröhlich's model, if the sum can be replaced by an integral in (4.38), when $\mu$ approaches $\hbar\omega_1$ very closely i.e. $\hbar\omega_1 \sim \mu$, an upper bound of N is reachable independently on $s_i$. Besides, always $s_i/S \leq 1$ leading to the independency of the upper bound of $N$ on $S$. However, this is contradictory with the results that the number of oscillating modes increases by higher amount of $S$. Therefore, the changing of sum to an integral is an incorrect replacement; Fröhlich showed that if the total rate of the external supply of energy $S$ increases after a certain threshold, the lowest frequency mode gets very strongly excited meaning that $n_1$ tends to become very large in comparison with all the others $n_i$ i.e. $n_1 \sim N$. This means that each electric oscillator tends to vibrate around the frequency of the lowest vibrational mode $\omega_1$. This conclusion is called Fröhlich condensation similar to the Einstein condensation of a Bose gas. Biomolecules can also behave as microscopic oscillating antennas if a phonon condensation takes place, which activates low frequency vibrational modes ($10^{11}$ Hz).

### 4.2.3 Wu-Austin model

As we already mentioned in (4.2.2), Fröhlichs mathematical analysis was based upon the utilization of rate equations. Wu and Austin proposed a theoretical and microscopic model using the interaction Hamiltonian formulated in second quantization formalism [58, 59]. They suppose a biological system ( biomolecule) consisting of:

- Oscillating dipoles ( normal modes) assigned with the quantum creation/annihilation operators $\widehat{a}^{\dagger}_{\omega_i}, \widehat{a}_{\omega_i}$ with the frequency $\omega_i$.
- A thermal bath at temperature $T_B$ toward which the normal modes of the biomolecule dissipate energy is represented by a collection of harmonic oscillators with characteristic frequencies $\Omega_j$ whose annihilation/creation operators are $\widehat{b}_{\Omega_j}$ and $\widehat{b}^{\dagger}_{\Omega_j}$.
- The external energy pumping is modeled by another thermal bath at a temperature $T_S \gg T_B$ ( in order to put the biomolecule out of thermal equilibrium), represented by a collection of harmonic oscillators with frequencies $\Omega^{'}_k$, the quantum annihilation/creation operators of which are $\widehat{c}_{\Omega^{'}_k}$ and $\widehat{c}^{\dagger}_{\Omega^{'}_k}$.

Thus, the Hamiltonian of biomolecule is given as

$$\hat{H}_{Tot} = \hat{H}_0 + \hat{H}_{Int} \tag{4.39}$$

where

$$\hat{H}_0 \;=\; \sum_{\omega_i} \hbar\omega_i \; \hat{a}_{\omega_i}\hat{a}^{\dagger}_{\omega_i} + \sum_{\Omega_j} \hbar\Omega_j \; \hat{b}_{\Omega_j}\hat{b}^{\dagger}_{\Omega_j} + \sum_{\Omega^{'}_k} \hbar\Omega^{'}_k \; \hat{c}_{\Omega^{'}_k}\hat{c}^{\dagger}_{\Omega^{'}_k}, \tag{4.40}$$

and

$$\begin{aligned} \hat{H}_{Int} \;&=\; \sum_{\omega_i,\Omega_j} \eta \; \hat{a}^{\dagger}_{\omega_i}\hat{b}_{\Omega_B} + \sum_{\omega_i,\Omega^{'}_k} \xi \; \hat{a}^{\dagger}_{\omega_i}\hat{c}_{\Omega^{'}_k} \\ &+ \sum_{\omega_{A_i},\omega_{A_j},\Omega_k} \chi \; \hat{a}^{\dagger}_{\omega_i}\hat{a}_{\omega_j}\hat{b}^{\dagger}_{\Omega_k} + \text{h.c.} \end{aligned} \tag{4.41}$$

The coefficient $\eta$ defines the linear interactions among the biomolecular normal modes and the thermal baths modes, $\xi$ is the linear interactions between the external source and the biomolecule and $\chi \in \mathbb{C}$ describes the mode-mode interactions among the biomolecule modes mediated by the modes of the thermal bath. If $|\psi(0)\rangle$ is the exact eigenstate of the Hamiltonian (4.40), then the wave function $|\psi(t)\rangle$ at time $t$ could be obtained. Using the Heisenberg equation the rate of change of $i$-th mode quanta is

$$\dot{n}_i = \frac{1}{\mathrm{i}\hbar}[n_i, H_{Tot}], \tag{4.42}$$

where $\hat{n}_i = \hat{a}^\dagger_{\omega_i}\hat{a}_{\omega_i}$. Then the expectation value $\langle \dot{n}_i \rangle = \langle \psi(t)|\dot{n}_i|\psi(t)\rangle$ is found to be

$$\begin{aligned}\langle \dot{n}_i \rangle &= S - \Phi(T, w_i)\left[\langle n_i\rangle e^{\beta\hbar\omega_i} - (1 + \langle n_i\rangle)\right] \\ &- \sum_j \Lambda(T, w_i, w_j)[\langle n_i\rangle(1 + \langle n_j\rangle)e^{\beta\hbar(\omega_i - \omega_j)} \\ &- \langle n_j\rangle(1 + \langle n_j\rangle)],\end{aligned} \tag{4.43}$$

Wu and Austin could find the stationary solution $\langle \dot{n}_i \rangle = 0$ and obtain

$$\langle n_i\rangle = \frac{1}{e^{\beta(\hbar\omega_i - \mu)} - 1}\left[1 + \frac{S}{\Phi(T, w_i) + \sum_j \Lambda(T, w_i, w_j)\langle n_j\rangle}\right], \tag{4.44}$$

where

$$e^{-\beta\mu} = \frac{\Phi(T, w_i) + \sum_j \Lambda(T, w_i, w_j)((1 + \langle n_j\rangle)e^{\beta\hbar\omega_j})}{\Phi(T, w_i) + \sum_j \langle n_j\rangle\Lambda(T, w_i, w_j)}, \tag{4.45}$$

$$S = 4\pi|\xi_{\omega_i\Omega'_k}|^2 \sum \langle \hat{c}^\dagger_{\Omega'_k}\hat{c}_{\Omega'_k}\rangle, \tag{4.46}$$

which is the number of quanta supplied to the $i$-th mode from the external source. Also

$$\Phi(T, w_i) = 4\pi|\eta_{\omega_i\Omega_j}|^2 e^{-\beta\hbar\omega_i}[1 + N(\hbar\omega_i)], \tag{4.47}$$

and

$$\begin{aligned}\Lambda(T, w_i, w_j) &= \pi|\chi_{\omega_i\omega_j\Omega_k}|^2 e^{-\beta\hbar(\omega_i - \omega_j)}[N(\hbar\omega_j - \hbar\omega_i)]; \quad \omega_j > \omega_i \\ \Lambda(T, w_i, w_j) &= \pi|\chi_{\omega_i\omega_j\Omega_k}|^2 e^{-\beta\hbar(\omega_i - \omega_j)}[1 + N(\hbar\omega_i - \hbar\omega_j)]; \quad \omega_i > \omega_j.\end{aligned} \tag{4.48}$$

where $N(\hbar\omega_i)$ describes the number of excitations with energy $\hbar\omega_i$ of the $i$-th mode in the heat bath. The Eqs. (4.44) and (4.45) are exactly the same of Eqs. (4.34) and (4.35) derived by Fröhlich. Thus, these results confirm the possibility of such a phenomenon as Bose condensation in biomolecules.

### 4.2.4 Out-of-equilibrium collective oscillations as phonon condensation in a model protein

Recently, a classical Hamiltonian associated with the quantum Wu-Austin Hamiltonian (4.39)- from which the Fröhlich rate can be derived- has been studied in [21], where they displayed theoretically and experimentally a non-equilibrium phonon condensation corresponding to a channeling into the lowest frequency mode of almost all the energy pumped into the system which means a collective molecular vibrations when the external pumping energy exceeds a threshold value. This phenomenon has been induced by light pumping, realised by shining a laser light on an aqueous solution of BSA (Bovine Serum Albumin) protein molecules each one carrying a few fluorophores covalently attached to their Lysine residues. The fluorophores were excited with a blue light at $4880\mathring{A}$ and then they re-emitted a broadband fluorescence radiation peaked at $5190\mathring{A}$, thus the difference between the absorbed and re-emitted photon energies resulted in a concentration of an average energy of 0.19 eV at the fluorophores sites which thus became "hot points" on each protein. A continuous energy supply of this kind was experimentally found effective to excite the vibrational modes of the proteins and, with an energy supply rate exceeding a suitable threshold, this eventually led to a phonon condensation phenomenon into the lowest vibrational frequency.

BSA (Bovine Serum Albumine) has been chosen as a test protein: such biomolecule is mainly made out of $\alpha$-helices largely studied in the physico-chemical literature. They play a central role in energy trapping mechanisms in biomolecules (2.2).

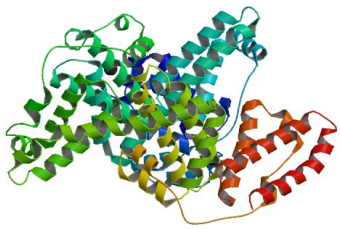

Figure 4.4 Crystal structure BSA

Figure (4.5) shows theoretically the stronger deviation from the energy equipartition corre-

sponding to an increase of the energy concentration in the lowest-frequency mode $\omega_0$ happens when the energy input rate $S$ gets larger.

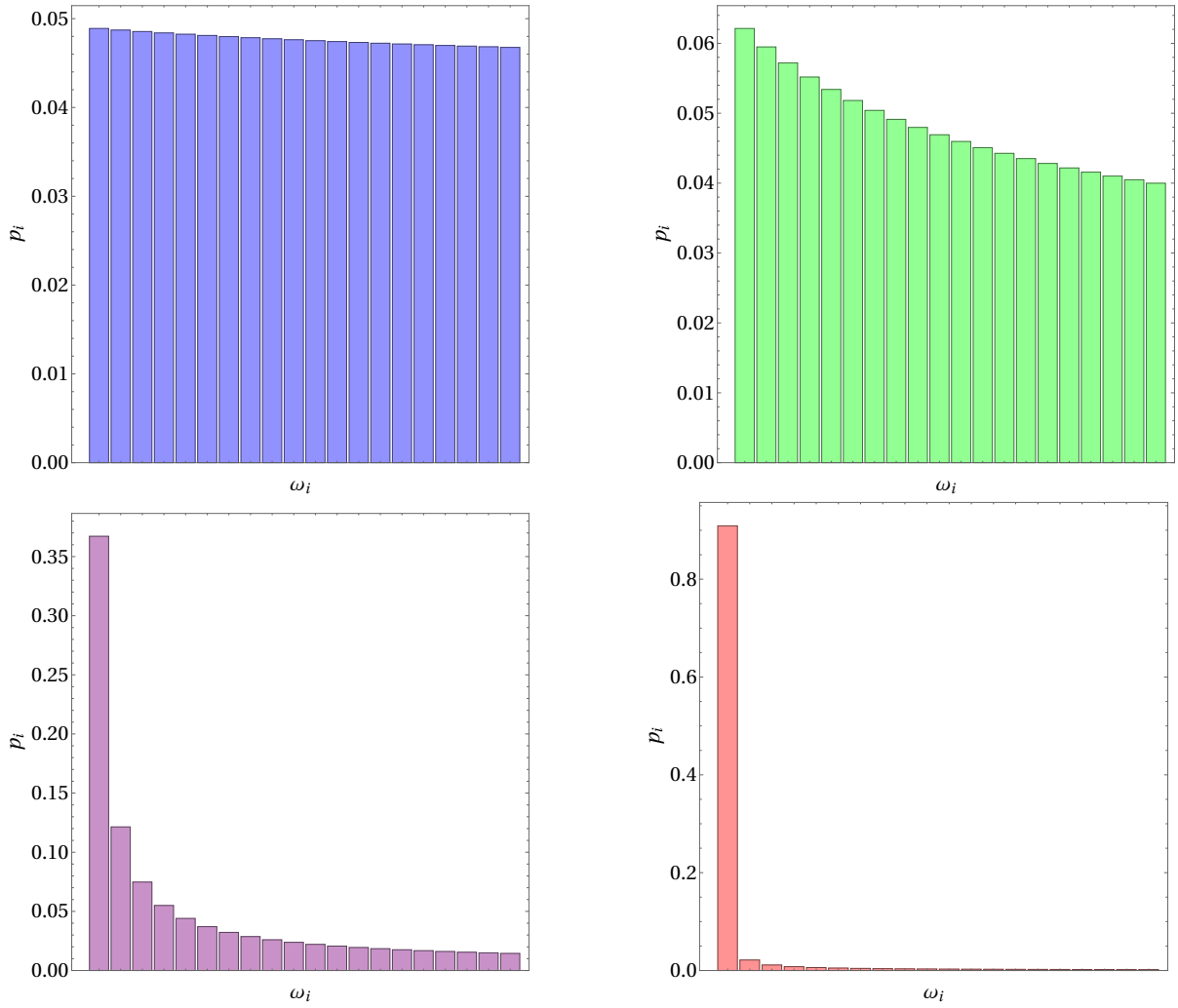


Figure 4.5 Adopted by [21]. Classical Fröhlich-like condensation; Normalized fractions of energy $p_i$ in normal modes vs the mode frequencies for $N = 20$ modes. The spectra correspond to $S = 0.1$ (blue), $S = 1$ (green), $S = 10$ (purple), and $S = 100$ (pink). Equipartition corresponds to equal heights of the bars.

Figure (4.6) highlights the qualitative agreement of the theory and experiment concerned a threshold of the increasing input energy to the protein for the appearance of the collective vibrational modes. The panel (a) shows an experimental threshold in the intensity of the resonant peak at 0.314 THz when the laser input power exceeds $10\mu$W. The panel (b) presents

theoretically a threshold of the intensity of the first mode for the different reported numbers of normal modes of the BSA protein. This threshold becomes more and more evident by increasing number of modes. Moreover, the same saturation effect can be seen in the high energy injection.

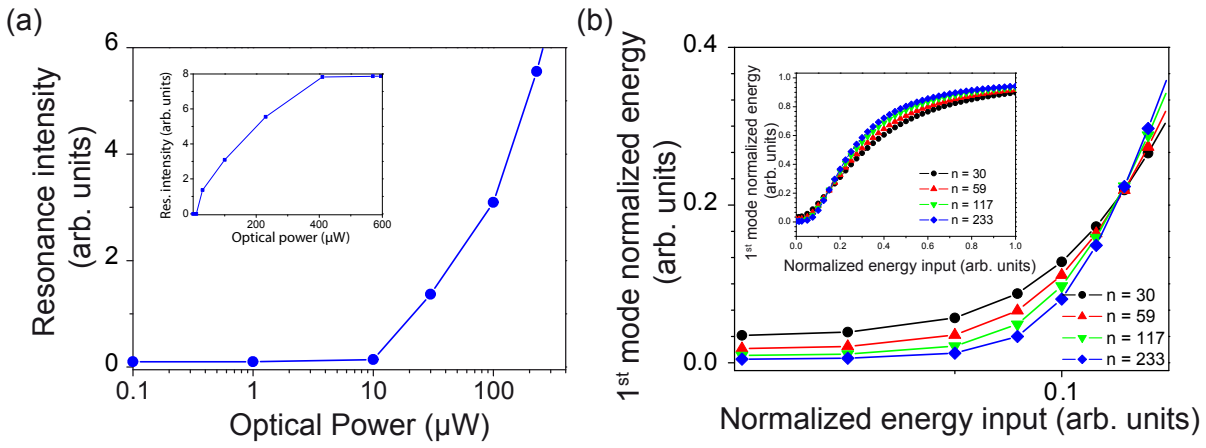


Figure 4.6 Adopted by [21]. Threshold-like behavior of collective vibrational modes. (a) Intensity of the resonant peak measured at 0.314 THz as a function of the optical laser power. (b) Normalized energy of the first mode calculated as a function of the normalized energy input. The different curves correspond to the reported numbers of normal modes of the BSA protein. Theory and experiment are in qualitative agreement.

### 4.2.5 Resonant long-range interactions between two oscillating dipole moments

Concerning the approach [22], two molecules $A$ and $B$ with dipole moments $\mu_A$ and $\mu_B$ oscillate respectively with harmonic frequencies $\omega_A$ and $\omega_B$ in a simple system. The equations of motion such for a system has the form

$$\begin{cases} \ddot{\boldsymbol{\mu}}_A + \gamma_A \dot{\boldsymbol{\mu}}_A + \omega_A^2 \boldsymbol{\mu}_A = \zeta_A \boldsymbol{E}_B(\boldsymbol{r}_A, t) + \boldsymbol{f}_A(\boldsymbol{\mu}_A, t) \\ \ddot{\boldsymbol{\mu}}_B + \gamma_B \dot{\boldsymbol{\mu}}_B + \omega_B^2 \boldsymbol{\mu}_B = \zeta_B \boldsymbol{E}_A(\boldsymbol{r}_B, t) + \boldsymbol{f}_B(\boldsymbol{\mu}_B, t). \end{cases} \tag{4.49}$$

In a dipole approximation, the interaction between two molecules is mediated by the electric field $\mathbb{E}_{A,B}(\mathbf{r}, t)$ created each oscillating dipole located at $\mathbf{r} = \mathbf{r}_{B,A}$. The coupling constants are $\zeta_i = Q_i^2/m_i, i = A, B$ where $Q_A$ and $Q_B$ are the effective charges of dipole $A$ and $B$, respectively with the effective masses $m_A$ and $m_B$. The damping coefficients $\gamma_{A,B}$ stand for the

radiation losses of the dipoles and finally the functions $\boldsymbol{f}_{A,B}$ belong to the possible anharmonic contributions for each dipole as well as the external excitations. In order for an estimation of the mean interaction energy of the dynamical equations, the frequencies of the normal modes are calculated. To this end, the harmonic and conservative system of (4.49) is written as

$$\begin{cases} \ddot{\boldsymbol{\mu}}_A + \omega_A^2 \boldsymbol{\mu}_A = \zeta_A \boldsymbol{E}_B(\boldsymbol{r}_A, t) \\ \\ \ddot{\boldsymbol{\mu}}_B + \omega_B^2 \boldsymbol{\mu}_B = \zeta_B \boldsymbol{E}_A(\boldsymbol{r}_B, t). \end{cases} \tag{4.50}$$

The normal frequencies $\omega_N$ are determined such that the solutions of above equations are $\boldsymbol{\mu}_{A,B}(t) = \boldsymbol{\mu}_{A,B} e^{i\omega_N t}$. Considering the dipole moments $A$ and $B$ oscillate at the same frequency $\omega_N$ as $\boldsymbol{\mu}_{A,B} = \boldsymbol{\mu}_{A,B}\delta(\omega - \omega_N)$, the electric field $\boldsymbol{E}_B(\boldsymbol{r}_A, t)$ created by the molecule $A$, by using the classical electrodynamics, is obtained ( the same expression is $\boldsymbol{E}_A(\boldsymbol{r}_B, t)$ created by the molecule $B$)

$$\boldsymbol{E}_B(\boldsymbol{r}_A, t) = \boldsymbol{\chi}(r, \omega)\boldsymbol{\mu}_B e^{i\omega t}, \tag{4.51}$$

in which $r = |\boldsymbol{r}_A - \boldsymbol{r}_B|$ is the intermolecular distance, and $\boldsymbol{\chi}(r, \omega)$ describes the susceptibility matrix of the electric field in the form

$$\begin{aligned} \chi_{11}(r,\omega) &= \chi_{22}(r,\omega) = -\frac{e^{\pm i\omega\sqrt{\varepsilon(\omega)}r/c}}{\varepsilon(\omega)r^3} \\ &\times \left(1 \mp \frac{i\omega\sqrt{\varepsilon(\omega)}r}{c} - \frac{\omega^2\varepsilon(\omega)r^2}{c^2}\right), \\ \chi_{33}(r,\omega) &= \frac{2e^{\pm i\omega\sqrt{\varepsilon(\omega)}r/c}}{\varepsilon(\omega)r^3}\left(1 \mp \frac{i\omega\sqrt{\varepsilon(\omega)}r}{c}\right), \\ \chi_{i\neq j}(r,\omega) &= 0. \end{aligned} \tag{4.52}$$

The sign $\pm$ is attributed to the positive or negative values of $\mathrm{Im}(\omega\sqrt{\varepsilon(\omega)})$. The matrix $\boldsymbol{\chi}(r, \omega)$ is diagonal because of setting the $z$ axis along $r$. The imaginary part of $\chi_{ii}(r, \omega)$ in (4.52) belongs to the dissipative effects due to the propagation of the electric field, but this dissipation is ignored in computation of normal frequencies and only the real part is accounted. Substituting $\boldsymbol{\mu}_{A,B}(t) = \boldsymbol{\mu}_{A,B} e^{i\omega_N t}$ in Eq. (4.51) and then Eq. (4.50) gives

$$\begin{aligned} (\omega_A^2 - \omega_N^2)\mu_{A,i} &= \zeta_A \chi'_{ii}(r, \omega_N)\mu_{B,i} \\ (\omega_B^2 - \omega_N^2)\mu_{B,i} &= \zeta_B \chi'_{ii}(r, \omega_N)\mu_{A,i}. \end{aligned} \tag{4.53}$$

Solving the above equations leads to two possible solutions for $\omega_N^2$ for each $i$ given by

$$\omega_{i,\pm}^2 = \frac{1}{2}\left\{\left(\omega_A^2+\omega_B^2\right) \pm \sqrt{\left(\omega_A^2-\omega_B^2\right)^2 + 4\zeta_A\zeta_B(\chi'_{ii}(r,\omega_{i,\pm}))^2}\right\}. \tag{4.54}$$

which are the frequencies of six uncoupled harmonic oscillators $i = 1, 2, 3$ with energies $E_{i,\pm} = \omega_{i,\pm}J_{i,\pm}$ where $J_{i,\pm}$ are the action constants defined by initial conditions of the system. Then two main possibilities are distinguished to compute interaction energy of the system containing two oscillating electric dipoles:

- In the *Non resonant case* when $\omega_A \gg \omega_B$ (or when $\omega_A \ll \omega_B$), Eq. (4.54) for all $i$, at lowest order, changes to

$$\omega_{i,\pm}^2 - \frac{1}{2}\left\{\left(\omega_A^2+\omega_B^2\right) \pm \left(\omega_A^2-\omega_B^2\right)\left(1+\frac{2\zeta_A\zeta_B(\chi'_{ii}(r,\omega_{i,\pm}))^2}{\left(\omega_A^2-\omega_B^2\right)^2}\right)\right\} \simeq 0,$$

  which results in

$$\underbrace{\omega_{i,\pm}^2 - \omega_{A,B}^2 \mp \frac{\zeta_A\zeta_B(\chi'_{ii}(r,\omega_{i,\pm}))^2}{\omega_A^2-\omega_B^2}}_{\Theta_{i,\pm}(r,\omega_{i,\pm})} = 0\ , \quad \begin{cases} \omega_A \quad \text{for} \quad \omega_{i,+}, \\ \\ \omega_B \quad \text{for} \quad \omega_{i,-}. \end{cases} \tag{4.55}$$

  Then using the Lagrange inversion theorem of complex analysis, at the first order, the frequencies of the normal modes are found

$$\omega_{i,\pm}(r) \simeq \omega_{A,B} \pm \underbrace{\frac{\zeta_A\zeta_B(\chi'_{ii}(r,\omega_{A,B})))^2}{2\omega_{A,B}\left(\omega_A^2-\omega_B^2\right)}}_{\Delta\omega_{A,B,i}(r)}. \tag{4.56}$$

  where the shift energy $\Delta\omega_{A,B,i}(r)$ is due to the interaction of two dipoles so that in absence of it, $\mu_A$ and $\mu_B$ are not interacting ($r \to \infty$). Then the total mean energy $\omega_{i,\pm}J_{i,\pm}$ is obtained

$$\begin{aligned} E_{tot} &= \sum_i E_{i,+} + E_{i,-} = \sum_i \omega_{i,+}J_{i,+} + \omega_{i,-}J_{i,-} \\ &= \underbrace{\sum_i \omega_A J_{i,+} + \omega_B J_{i,-}}_{\substack{\text{Energy of the} \\ \text{uncoupled system}}} + \underbrace{\sum_i \Delta\omega_{A,i}(r)J_{i,+} - \Delta\omega_{B,i}(r)J_{i,-}}_{\text{Interaction Energy } U(r)}. \end{aligned} \tag{4.57}$$

Concerning Eqs. (4.52) and (4.56), the interaction energy $U(r)$ scales proportionally to $\left(\chi'_{ii}(r,\omega_{A,B})\right)^2$ and consequently in a near zone limit $r \ll c/\omega_{A,B}$, it is found that $U(r) \propto \pm\left[\chi'_{ii}(r,\omega_{A,B})\right]^2 \sim \pm\frac{1}{r^6}$, being the short-range interaction energy. But at far zone limit $r \gg c/\omega_{A,B}$ the interaction oscillates with an envelop potential to $1/r^2$ due to the retardation effects.

- The *resonant case* when $\omega_A \simeq \omega_B = \omega_0$, the Eq. (4.54) is simplified to

$$\underbrace{\omega_{i,\pm}^2 - \omega_0^2 \mp \sqrt{\zeta_A\zeta_B}\chi'_{ii}(r,\omega_{i,\pm})}_{\Theta_{i,\pm}(r,\omega_{i,\pm})} = 0. \tag{4.58}$$

After the complex analysis, the frequencies of the normal modes at the lowest order in resonant case is obtained as

$$\omega_{i,\pm}(r) \simeq \omega_0 \pm \underbrace{\sqrt{\zeta_A\zeta_B}\frac{\chi'_{ii}(r,\omega_0)}{2\omega_0}}_{\Delta\omega_{0,i}(r)}, \tag{4.59}$$

where the frequency shift is proportional to $\chi'_{ii}(r,\omega_0)$. The total mean energy corresponding to the Eq. (4.59) is given by

$$E_{tot} = \underbrace{\sum_i \omega_0 J_{i,+} + \omega_0 J_{i,-}}_{\substack{\text{Energy of the}\\ \text{uncoupled system}}} + \underbrace{\sum_i \Delta\omega_{0,i}(r)\left(J_{i,+} - J_{i,-}\right)}_{\text{Interaction Energy } U(r)}. \tag{4.60}$$

Regarding the Eqs. (4.52) and (4.59) the interaction energy $U(r)$ gets a polynomial in $1/r^\alpha$ with $\alpha \leq 3$ (the dimension of physical space). Thus the long range interactions are expected when two dipoles oscillate with resonant frequencies. In the near zone limit $r \ll c/\omega_0$ the dominant contribution of interaction energy is found to be $U(r) \propto \pm\chi'_{ii}(r,\omega_{A,B}) \sim \pm\frac{1}{r^3}$ and in the far zone limits the interaction oscillates for a longer distance with a $1/r$ envelop.

All in all, it is obvious from Eq. (4.60) that when $\Delta U = 0$ ($J_{i,+} = J_{i,-} = \text{Cons.}$) the energy distributes equally among two dipoles. In other words, the situation of out-of-thermal equilibrium is necessary to activate the long-range interactions so that, for instance, $J_{3,+} > J_{3,-}$ where $J_{3,\pm}$ are the action of the longitudinal modes.

## 4.3 Resonant recognition model

Deoxyribonucleic acid or DNA is a macromolecule composed of two strands of sugars of four nucleotides coiling around each other to form a double helix carrying genetic information of any living organism represented by given sequence of four nucleotides. The nucleotides of two strands are joined to one another in a chain by covalent bonds called base pairs (A with T and C with G). This information called coding sequences specify the sequence of amino acids within proteins in a process called translation. Proteins are the main conductors within a cell, tissue or organism having biological functions considered as selective interactions of protein and its targets (other protein, DNA regulatory segment or small molecule). Resonant recognition model (RRM) [60] is a physical and mathematical approach based on the representation of the protein primary structure as a numerical sequences by assigning to each amino acid a physical parameter value relevant to the energy of delocalized electrons of each particular amino acid. The biological activity of protein having the strongest effect on the electronic distribution of the whole protein is calculated as the electron-ion interaction potential (EIIP)

$$\langle k+q|w|k\rangle = \beta_1 \sin(2\pi\beta_2\eta)/2\pi\eta \tag{4.61}$$

where $q$ is a change of momentum $k$ of the delocalized electron in the interaction with potential pseudopotential $\omega$ which is considered to be unified Coulomb potential which happens because of the Ze core and the potential component resulting from the Pauli repulsion exerted by the bound electrons. The Coulomb component in the range of small wave numbers and, at the same time, to change it by further decreasing the oscillating potential in the range of large wave numbers is assumed to be suitable for potential structure [61]. The parameters $\beta_1$, and $\beta_2$ are the parameters based on Heine-Abarenkov potential [1] and $\eta = q/2k_f$ with $q$ a wave number and $k_f$ the corresponding Fermi momentum. From (4.61) the following relation is derived

$$\lim_{q\to 0}\langle k+q|w|k\rangle = \lim_{q\to 0}\beta_1\beta_2\frac{\sin(2\pi\beta_2\eta)}{2\pi\beta_2\eta} = \beta_1\beta_2. \tag{4.62}$$

The local potential in which the Coulomb potential is included defines as

$$\lim_{q\to 0}\langle k+q|w|k\rangle = \frac{2}{3}\hbar^2 k_f^2/2m^* = \frac{2}{3}E_f, \tag{4.63}$$

[1] A model potential which is fitted to the spectroscopically measured energy levels of the free ions [62].

where $E_f$ is the Fermi energy. By comparing (4.62) and (4.63) it is obtain $\beta_1\beta_2 = \frac{2}{3}E_f$. Thus, $\beta_2$ can be found when according to Eq. (4.61) only $\beta_1$ should be fitted. Then EIIP values describing the average energy states of all valence electrons in particular amino acids calculated by

$$\langle k+q|w|k\rangle = 0.25Z\sin(\pi 1.04Z)/2\pi, \tag{4.64}$$

where

$$Z = \frac{1}{N}\sum z_i \tag{4.65}$$

in which $N$ is the total number of atoms in the amino acid and $z_i$, is the number of valence electrons of the $i$-th component of each amino acid. The whole procedure can also be applied to the DNA and RNA, and the EIIP values for 20 amino acids, as well as for 5 nucleotides are shown in Tables (4.1) and (4.2). Each amino acid or nucleotide can be represented by a unique number unrelated to its position in a sequence. By digital signal analysis method, the original numerical series are transformed to the frequency domain using the discrete Fourier transform (DFT) in order to extract information relevant to the biological function. If $X_n$ and $Y_n$ are the DFT of sequences $x(m)$ and $y(m)$, respectively, then the common spectral characteristics of these two series in order to check if they have the same biological function is studied by the cross-spectrum

$$S_n = X_n Y_n^*, \qquad n = 1, 2, ..., N/2. \tag{4.66}$$

The common frequency components of the two sequences analyzed causes peak frequencies in the amplitude cross-spectral function. The whole procedures for the sequences of basic and acidic bovine FGF's represented in Fig. (4.7).

For a group of protein sequences, the common frequency spectrum is derived by calculating the absolute values of multiple cross-spectral function coefficients $M$ as

$$|M_n| = |X1n|.|X2n|...|XMn|, \qquad n = 1, 2, ..., N/2. \tag{4.67}$$

A signal-to-noise ratio between signal intensity at the particular peak frequency and the mean value over the whole spectrum ($S/N$) is calculated to define to measure similarity between sequences analyzed. The presence of a peak frequency with a significant ($S/N$) in the multiple cross-spectral function implies that all of the analyzed sequences within the group possess one frequency component in common sharing the same biological function. The ratio of at least 20 is considered significant.

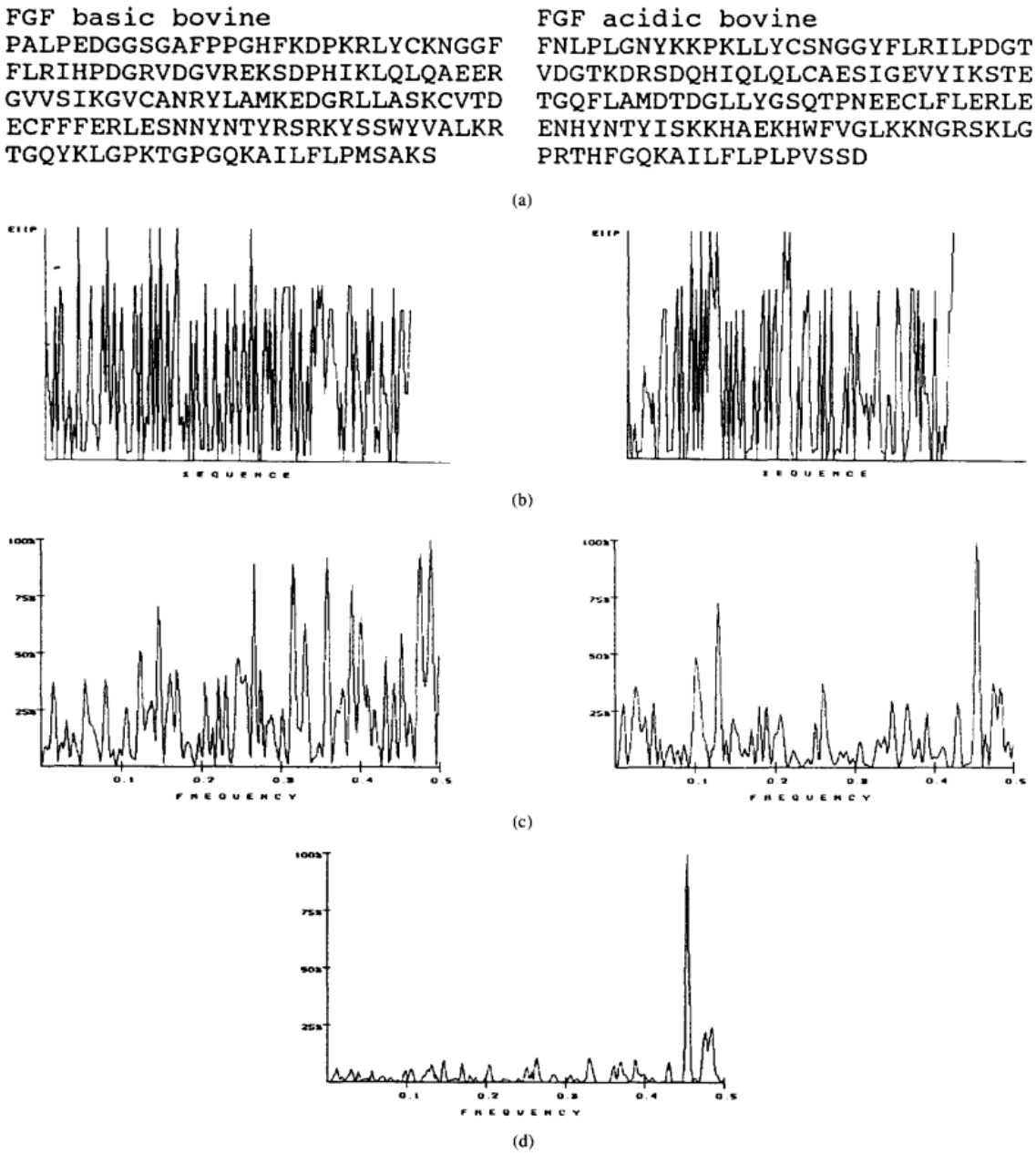


Figure 4.7 Adupted by [60]. The RRM procedure: (a) sequences of basic and acidic bovine FGF's, (b) representation of the corresponding numerical series of each amino acid with its EIIP value;(c) spectra of both basic and acidic FGF sequences; (d) cross-spectrum of the spectra presented in (c). The sharp peaks denote common frequency components. The frequencies are normalized.

Each frequency in the RRM characterizes one biological function involving interactions between proteins and their targets (other protein, DNA regulatory segment or small molecule). Each biological process within the protein structure involves energy transfer between interacting

molecules which are highly selective. Protein and their protein or DNA targets have been analyzed to understand if RRM characteristic frequencies denote a parameter which describes this selectivity between interacting molecules. Therefore, it can be postulated that RRM characteristic frequencies characterize not only general functions but also provide recognition between a particular protein and its target. This recognition is due to the fact that the matching of periodicities of the energy transfer of free electrons along the interacting proteins. Actually, it is supposed that the characteristic frequencies in the RRM model are responsible for resonant recognition between macromolecules at a distance. Consequently, these frequencies belong to oscillations of some physical field propagating probably through water dipoles. One possibility is that the field is electromagnetic in essence with a range dependent on charge velocity ( superconductive, conductive, soliton transfer, etc.). The physics behind this process is still unknown although the difference of the free electron potentials EIIP at the $N$ and $C$ terminals of the protein $W = W(COOH) - W(NH_2) = 0.13$ Ry might cause frequency $10^{13} < f < 10^{15} Hz$ that could be emitted during the electron transfer [60]. However, this is a very rough calculation and more precise estimation could only be made with biological experiments and theoretical models.

| **Nucleotide** | **EIIP Ry** | **EIIP eV** | **Nucleotide** | **EIIP Ry** | **EIIP eV** |
|---|---|---|---|---|---|
| A | 0.1260 | 1.7143 | T | 0.1335 | 1.8164 |
| G | 0.0806 | 1.0966 | C | 0.1340 | 1.8232 |

Table 4.1 Electron-Ion interaction potential (EIIP) values for nucleotides adenine (A), thymine (T), guanine (G), and cytosine (C). From Ref.[60].

| **Nucleotide** | **EIIP Ry** | **EIIP eV** | **Nucleotide** | **EIIP Ry** | **EIIP eV** |
|---|---|---|---|---|---|
| Leu | 0.0000 | 0.0000 | Tyr | 0.0516 | 0.7017 |
| Ile | 0.0000 | 0.0000 | Trp | 0.0548 | 0.7452 |
| Asn | 0.0036 | 0.0489 | Gln | 0.0761 | 1.0349 |
| Gly | 0.0050 | 0.0680 | Met | 0.0823 | 1.1192 |
| Val | 0.0057 | 0.0775 | Ser | 0.0829 | 1.1274 |
| Glu | 0.0058 | 0.0788 | Cys | 0.0829 | 1.1274 |
| Pro | 0.0198 | 0.2692 | Thr | 0.0941 | 1.2797 |
| His | 0.0242 | 0.3291 | Phe | 0.0946 | 1.2865 |
| Lys | 0.0371 | 0.5045 | Arg | 0.0959 | 1.3042 |
| Ala | 0.0373 | 0.5072 | Asp | 0.1263 | 1.7176 |

Table 4.2 Electron-Ion interaction potential (EIIP) values for nucleotides adenine (A), thymine (T), guanine (G), and cytosine (C). From Ref.[60].

# CHAPTER 5. Energy transfer to the phonons of a macromolecule through light pumping

Already we reported the recent work concerned the activation of out-of-equilibrium collective intramolecular vibrations of a model protein in (4.2.4). The relevance of this work consists in the possibility of activating long-range electrodynamic interactions between bio-macromolecules (4.2.5). The reason is that, at thermal equilibrium, a macromolecule vibrates incoherently with a broad spectrum of modes, whereas the action of an external source of energy promoting a phenomenon of phonon condensation can induce the coherent motion of the molecular subunits, so that, the resulting collective vibration can bring about a large oscillating dipole moment. Under this condition long-range and resonant (thus selective) electrodynamic forces can be activated. In turn, these electrodynamic forces could help explaining the astonishing efficiency of the impressively complex biochemical machinery at work in living cells [63], where the different actors (proteins, DNA and RNA) find their cognate partners and targets in the right place, at the right time and in the right sequence in an overcrowded environment (the cytosol). Electrodynamic resonant/selective forces are the only possible one to act at a long distance, all the others (chemical bonds, Van der Waals and electrostatic forces) are in fact either intrinsically acting at very short distances, or are screened by the freely moving small ions in the cytosol. Actually, this is a longstanding theoretical scenario [19, 64, 20] which, for several reasons, has been discarded. However, the upgrade of Fröhlich's theoretical proposition in [21, 22] and the experimental outcomes reported in [21], represent a first crucial leap forward to ascertain whether the above mentioned hypotheses can be given experimental confirmation or refutation that can be attempted with the nowadays available technology [65, 66].

In [23] we study, qualitatively and quantitatively, how the model of external energy feeding of proteins - through a high temperature heat bath - can be improved to better represent the experimental conditions realised in Ref.[21] where a laser light shines on dye-labeled proteins. This means that the external energy supply is done by an electron excitation which has to be

converted into vibrational energy of the chain of subunits (amino acids) composing a macromolecule (protein), a process lacking description in Wu-Austin Hamiltonian (4.39). This is a very fast process with respect to the phonon condensation phenomenon, therefore it is meaningful to study it separately from the latter which has already been satisfactorily understood. As we shall see, it is found that only a fraction of the initially available electron energy is released to the phonons of a biomolecule. Even an approximate estimate of this energy transfer process is very important for a better assessment of the physical conditions that are necessary to activate the intramolecular collective vibrations.

## 5.1 Definition of the model

In the subsection (4.2.4) the external source of energy driving the phonon condensation was modeled as high temperature heat bath. This was done to reformulate in a classical framework the Wu-Austin quantum model (4.2.3) leading to the original Fröhlich rate Eqs. (4.34) and (4.35). We now aim at refining this part of the model in view of a better understanding of the basic excitation mechanism that can bring a macromolecule out of thermal equilibrium. In both cases of photo-excitation and, presumably, of ionic collisions, the excitation mechanism is supposed to be mediated by the molecular electron cloud. Therefore, the model describing the phenomenon that we want to investigate is a generalization of the standard Davydov (2.2.2) and Holstein-Fröhlich models (2.2.1) and (4.2.2) to account for electron-phonon interaction [18, 35, 67, 68]. In this model we have considered only a longitudinal chain of amino acids $\alpha = 1$ of Davydov's model. According to the energy operator (2.15) as

$$\hat{H} = \hat{H}_{el} + \hat{H}_{ph} + \hat{H}_{int}, \tag{5.1}$$

the electron energy $\hat{H}_{el}$ is written as

$$\hat{H}_{el} = \sum_{n=1}^{N} \Big[ E_0 \hat{B}_n^\dagger \hat{B}_n + \epsilon \langle \hat{B}_n^\dagger \hat{B}_n \rangle \hat{B}_n^\dagger \hat{B}_n + J(\hat{B}_n^\dagger \hat{B}_{n+1} + \hat{B}_n^\dagger \hat{B}_{n-1}) \Big]. \tag{5.2}$$

The term $E_0 \hat{B}_n^\dagger \hat{B}_n$ accounts for the initial "bare" electron energy distributed on several lattice sites according to initial shape of the electron wavefunction. The electron moving from the excited fluorophore interacts on its way with almost free electrons in each amino acid, and it may just make a disturbance which will allow a next electron to continue on the trip. It would

be then more a disturbance traveling than a single electron, but the net effect will be the same of a traveling electron. Thus the term $\epsilon\langle\hat{B}_n^\dagger\hat{B}_n\rangle\hat{B}_n^\dagger\hat{B}_n$ has been introduced to take into account non-linear effects due to the interaction between the electron in motion along the chain and the electrons of the substrate of amino acids. In particular, the term takes into account effects related to the Coulombic repulsion between the traveling electron and the charges localized on the amino acids. The averaging is intended as the expectation value of $\hat{B}_n^\dagger\hat{B}_n$ on the dynamically evolving state of the system. Then the phonon energy operator is defined as

$$\hat{H}_{ph} = \frac{1}{2}\sum_n \left[\frac{\hat{p}_n^2}{M} + \Omega(\hat{u}_{n+1} - \hat{u}_n)^2 + \frac{1}{2}\mu(\hat{u}_{n+1} - \hat{u}_n)^4\right], \tag{5.3}$$

The quartic term is a correction stemming from the power series which gives the harmonic term at the lowest order expansion around the minimum of interparticle interaction potential (typically nonlinear, as is the case, for example, of the Van der Waals potential). This term is responsible for phonon-phonon interaction, absent in the harmonic approximation; the parameter $\mu$ sets the strength of the phonon-phonon coupling.

Finally, the electron-phonon interaction operator is

$$\hat{H}_{int} = \sum_n \chi(\hat{u}_{n+1} - \hat{u}_n)\hat{B}_n^\dagger\hat{B}_n. \tag{5.4}$$

## 5.2 Derivation of the dynamical equations with TDVP

In order to derive from the model Hamiltonian (5.1) the corresponding dynamical equations, we consider a simplifying ansatz about the state vectors by assuming the factorization (2.19):

$$|\psi(t)\rangle = |\Psi(t)\rangle|\Phi(t)\rangle, \tag{5.5}$$

describing an electron (2.20) given a single quantum excitation and supposed to be free to propagate along the chain of $N$ amino acids composing a protein and the phononic state (2.35). To derive the dynamical equations we resort to TDVP technic (2.3) and define a new wave function (2.54) in terms of $|\psi\rangle$ in Eq. (5.5).

Then from Eqs. (5.5), (2.20), and (2.35) we write

$$\partial_t|\psi\rangle = \left(\partial_t|\Psi\rangle\right)|\Phi\rangle + |\Psi\rangle\left(\partial_t|\Phi\rangle\right), \tag{5.6}$$

and then arrive at

$$\langle\psi|\partial_t|\psi\rangle = \sum_n \left[\dot{C}_n(t)C_n^*(t) + \frac{i}{2\hbar}\Big(\dot{\pi}_n(t)\beta_n(t) - \pi_n(t)\dot{\beta}_n(t)\Big)\right]. \tag{5.7}$$

Thus the Lagrangian (2.58) becomes

$$\begin{aligned} L \;\; = \sum_n \Big(i\hbar\dot{C}_n(t)C_n^*(t) + \frac{1}{2}\Big(\pi_n(t)\dot{\beta}_n(t) - \dot{\pi}_n(t)\beta_n(t)\Big) \\ -H(C_n, C_n^*, \beta_n, \pi_n)\Big), \end{aligned} \tag{5.8}$$

where

$$\sum_n H(C_n, C_n^*, \beta_n, \pi_n) = \langle\psi(t)|\hat{H}|\psi(t)\rangle. \tag{5.9}$$

Imposing the condition (2.59), we get

$$\begin{aligned} \delta S(t) \;\; = \;\; & \sum_n \Big\{i\hbar\Big( - \dot{C}_n^*(t)\delta C_n(t) + \dot{C}_n(t)\delta C_n^*(t)\Big) \\ + \;\; & \dot{\beta}_n(t)\delta\pi_n(t) - \dot{\pi}_n(t)\delta\beta_n(t) \\ - \;\; & (\partial_{C_n}H)\delta C_n - (\partial_{C_n^*}H)\delta C_n^* \\ - \;\; & (\partial_{\beta_n}H)\delta\beta_n - (\partial_{\pi_n}H)\delta\pi_n\Big\} = 0, \end{aligned} \tag{5.10}$$

from which it results

$$\begin{aligned} i\hbar\dot{C}_n \;\; &= \;\; \partial_{C_n^*}H \\ \dot{\beta}_n \;\; &= \;\; \partial_{\pi_n}H \\ \dot{\pi}_n \;\; &= \;\; -\partial_{\beta_n}H\ . \end{aligned} \tag{5.11}$$

The expectation value of the Hamiltonian (5.1) is

$$\begin{aligned} \langle\psi|\hat{H}|\psi\rangle \;\; = \sum_n \Big[E_0|C_n|^2 + \epsilon|C_n|^4 + J(C_n^*C_{n+1} + C_{n+1}^*C_n) \\ +\frac{1}{2}\Big(\frac{1}{M}\pi_n^2 + \Omega(\beta_{n+1} - \beta_n)^2 + \frac{1}{2}\mu(\beta_{n+1} - \beta_n)^4\Big) \\ +\chi(\beta_{n+1} - \beta_n)|C_n|^2\Big]. \end{aligned} \tag{5.12}$$

So, from Eq. (5.12) we obtain the explicit form of the dynamical equations

$$\begin{aligned} i\hbar\dot{C}_n &= \Big(E_0 + 2\epsilon|C_n|^2 + \chi(\beta_{n+1} - \beta_n)\Big)C_n + J(C_{n+1} + C_{n-1}), \\ M\ddot{\beta}_n &= \Omega(\beta_{n+1} - 2\beta_n + \beta_{n-1}) + \chi\Big(|C_n|^2 - |C_{n-1}|^2\Big) \\ &+ \mu\Big((\beta_{n+1} - \beta_n)^3 - (\beta_n - \beta_{n-1})^3\Big). \end{aligned} \tag{5.13}$$

### 5.3 Definition of the physical parameters for numerical simulations

Let us see how to make a physically reasonable choice of the coupling parameters entering the Hamiltonian. We borrow from Ref.[60, 61] the estimates of the interaction energy between an electron and each of all the 20 amino acids (reported in Table 4.2). The average value of these interaction energies is $\langle\Delta E\rangle = 0.74$ eV with a dispersion $\sigma_E = 0.47$ eV. As a first rough picture of an electron hopping across the sequence of amino acids constituting a protein we can consider the electron of energy $E_0$ moving in a periodic sequence of square potential barriers of height $V_0 = 0.74$ eV and of width $a = 4.5\mathring{A}$, the average distance between two nearest neighboring amino acids [18]. We can then weigh the electron hopping operators between neighbouring sites with the probability $P(n \to n \pm 1)$ of tunnelling from one potential well to the nearest ones. This is achieved by computing the transmission coefficient

$$T = \left[1 + \frac{V_0^2 \sinh^2 \beta a}{4E_0(V_0 - E_0)}\right]^{-1} \tag{5.14}$$

where $\beta = [2m_e(V_0 - E_0)/\hbar^2]^{1/2}$. Moreover, the coefficient of the electron hopping term in the Hamiltonian has to be a characteristic energy scale of the process, thus a natural choice is to set $J \propto \langle\Delta E\rangle T$, then, assuming that an electron is initially excited at any given point of the chain of amino acids and that it has the same probability of moving to the left or to the right, we add a factor $1/2$ so that finally we have $J = \frac{1}{2}\langle\Delta E\rangle T$. Now, assuming $E_0 = 0.19$ eV as initial value of the electron energy, we find $J = 0.0585$ eV, whereas assuming that only a fraction $\delta \in [0, 1]$ of the maximum available energy is kept by the electron, for example for $\delta = 0.5$, we find $J = 0.031$ eV. For what concerns the electron-phonon coupling constant $\chi$, we make a rough estimate of its value as $\chi = \Delta E/\Delta x = \sigma_E/\Delta x = \sigma_E/a = 0.47eV/4.5\mathring{A} \simeq 100$ pN.

In what follows, in dimensionless units, we have $\chi' = 0.81$, and $J' = 5$ with $\delta = 0.5$, while $J' = 9$ with $\delta = 1$.

By rescaling time and lengths as $t = \omega^{-1}\tau$ and $\beta_n = Lb_n$, respectively, where $L = \sqrt{\hbar\omega^{-1}M^{-1}}$, the following dimensionless dynamical equations from (6.13) are obtained

$$\begin{aligned} i\frac{dC_n}{d\tau} &= \Big[\Big(E' + 2\epsilon'|C_n|^2 + \chi'(b_{n+1} - b_n)\Big)C_n + J'(C_{n+1} + C_{n-1})\Big], \\ \frac{d^2b_n}{d\tau^2} &= \Omega'(b_{n+1} - 2b_n + b_{n-1}) + \chi'\Big(|C_n|^2 - |C_{n-1}|^2\Big) \\ &+ \mu'\Big[(b_{n+1} - b_n)^3 - (b_n - b_{n-1})^3\Big], \end{aligned} \tag{5.15}$$

and the dimensionless expression of the Hamiltonian (5.12) is

$$\begin{aligned} \langle\psi|\hat{H}|\psi\rangle = \sum_n \Big[&E'|C_n|^2 + \epsilon'|C_n|^4 + J'(C_n^*C_{n+1} + C_{n+1}^*C_n) \\ &+ \frac{1}{2}\Big(\dot{b}_n^2 + \Omega'(b_{n+1} - b_n)^2 + \frac{1}{2}\mu'(b_{n+1} - b_n)^4\Big) \\ &+ \chi'(b_{n+1} - b_n)|C_n|^2\Big], \end{aligned} \tag{5.16}$$

where

$$\begin{aligned} E' &= \frac{E_0}{\hbar\omega}; \qquad \epsilon' = \frac{\epsilon}{\hbar\omega}; \qquad J' = \frac{J}{\hbar\omega}; \\ \chi' &= \frac{\chi}{\sqrt{\hbar M\omega^3}}; \qquad \Omega' = \frac{\Omega}{M\omega^2}; \qquad \mu' = \frac{\mu\hbar}{M^2\omega^3}\ . \end{aligned} \tag{5.17}$$

In order to perform numerical integration of the dynamical equations it is useful to introduce the variables

$$q_n = \frac{C_n + C_n^*}{\sqrt{2}}, \qquad p_n = \frac{C_n - C_n^*}{i\sqrt{2}}\ , \tag{5.18}$$

so that Eqs.(5.15) become

$$\dot{q}_n = \Big[E' + \frac{\epsilon'}{2}(q_n^2 + p_n^2) + \chi'(b_{n+1} - b_n)\Big]p_n + J'(p_{n+1} + p_{n-1}), \tag{5.19}$$

$$\dot{p}_n = -\Big[E' + \frac{\epsilon'}{2}(q_n^2 + p_n^2) + \chi'(b_{n+1} - b_n)\Big]q_n + J'(q_{n+1} + q_{n-1})\Big], \tag{5.20}$$

$$\begin{aligned} \ddot{b}_n = &\Omega'(b_{n+1} - 2b_n + b_{n-1}) + \frac{\chi'}{2}\Big((q_n^2 + p_n^2) - (q_{n-1}^2 + p_{n-1}^2)\Big) \\ &+ \mu'\Big[(b_{n+1} - b_n)^3 - (b_n - b_{n-1})^3\Big]. \end{aligned} \tag{5.21}$$

By denoting with $\mathcal{B}_n[\mathbf{b}(t), \mathbf{q}(t), \mathbf{p}(t)]$ the r.h.s. of Eq. (5.21) we have

$$b_n(t + \Delta t) = 2b_n(t) - b_n(t - \Delta t) + (\Delta t)^2 \mathcal{B}_n[\mathbf{b}(t), \mathbf{q}(t), \mathbf{p}(t)] \tag{5.22}$$

which can be rewritten in the form

$$\begin{aligned} \dot{b}_n &= \pi_n \\ \dot{\pi}_n &= \mathcal{B}_n[\mathbf{b}(t), \mathbf{q}(t), \mathbf{p}(t)] \ . \end{aligned} \tag{5.23}$$

Equations (5.19) and (5.20) and the above system have been numerically integrated by combining a finite differences scheme and a leap-frog scheme as follows

$$\begin{aligned} q_n(t + \Delta t) &= q_n(t) + \Delta t \ \mathcal{Q}_n[\mathbf{b}(t), \mathbf{q}(t), \mathbf{p}(t)], \\ p_n(t + \Delta t) &= p_n(t) + \Delta t \ \mathcal{P}_n[\mathbf{b}(t), \mathbf{q}(t), \mathbf{p}(t)], \\ b_n(t + \Delta t) &= b_n(t) + \Delta t \ \pi_n(t), \\ \pi_n(t + \Delta t) &= \pi_n(t) + \Delta t \ \mathcal{B}_n[\mathbf{b}(t + \Delta t), \mathbf{q}(t + \Delta t), \mathbf{p}(t + \Delta t)]. \end{aligned} \tag{5.24}$$

where $\mathcal{Q}_n[\mathbf{b}(t), \mathbf{q}(t), \mathbf{p}(t)]$ and $\mathcal{P}_n[\mathbf{b}(t), \mathbf{q}(t), \mathbf{p}(t)$ are the r.h.s. of Eqs.(5.19) and (5.20), respectively. By using sufficiently small time steps $\Delta t$ the desired precision of energy conservation can be attained.

About the initial conditions, we aim at simulating a physical situation where each photon absorbed by a fluorophore attached to a protein releases - in the average - 0.19 eV of energy to the surrounding electron cloud. This energy is the difference between the energies of the absorbed photon of $4880\mathring{A}$ and that of the re-emitted one as fluorescent radiation of $5150\mathring{A}$. We assume, as already stated above, that the effect of a single photon excitation is to make one electron moving across the protein by tunnelling through a sequence of potential barriers. In the experiments to which we are referring [21] each protein is labelled with 5-6 fluorochromes, and a laser light is continuously shined on the labelled proteins, therefore what we are after is modelling an elementary process and assuming, in a first approximation, a property of additivity of the same elementary process. In other words, if more than one electron is activated we assume that the resulting physical effect is the sum of a single electron effect. As a consequence, the electron initial condition is assumed as (2.48) centered at the site $n = n_0$ at time $t = 0$ and the

initial velocity $v = 0$ [18] as

$$C_n(t=0) \quad = \quad \frac{1}{\sqrt{8\sigma_0}}\text{sech}\Big(\frac{n-n_0}{4\sigma_0}\Big), \tag{5.25}$$

and coming to the initial conditions of the phonon component of the system, we assume a thermalized macromolecule at room temperature, that is at $T = 310K$. At equilibrium, the energy equipartition theorem for the Hamiltonian (5.3) reads

$$\left\langle p_n \frac{\partial H_{ph}}{\partial p_n} \right\rangle = \left\langle u_n \frac{\partial H_{ph}}{\partial u_n} \right\rangle = k_B T \tag{5.26}$$

where $k_B$ is the Boltzmann constant. At thermal equilibrium, energy is equally shared among all the degrees of freedom and, in particular, between kinetic and potential energies, therefore at $t = 0$ the velocities and the displacements have been initialized with random values of zero mean and fulfilling the conditions

$$\langle |b_n(0)| \rangle_n = \sqrt{\frac{k_B T}{\hbar \omega \Omega'}}; \qquad\qquad \langle |\dot{b}_n(0)| \rangle_n = \sqrt{\frac{k_B T}{\hbar \omega}}. \tag{5.27}$$

expressed in dimensionless form. In Table 5.1 the values chosen for the physical parameters are reported. These are: the initial excitation energy $E_0$, an average value of the mass $M$ of the amino acids, the electron hopping parameter $J$, the elasticity constant $\Omega$ used in the numerical studies of Ref. [18], and the electron-phonon coupling $\chi$. In Table 5.1 also the corresponding dimensionless values of the same physical quantities are reported, these are obtained by using (5.17) and the frequency $\omega = 10^{13} s^{-1}$.

| Name | Symbol | Value | Symbol | Dimensionless value |
|---|---|---|---|---|
| Hot-point energy | $E_0$ | 0.2 eV | $E'$ | 30 |
| Average mass of amino acids | M | $1.5 \times 10^{-25}$ kg | - | - |
| Spring constant | $\Omega$ | 18.3 N/m | $\Omega'$ | 1.2 |
| Electron hopping parameter | $J$ | 0.0658 eV | $J'$ | 10 |
| Electron-phonon coupling | $\chi$ | 61-610 pN | $\chi'$ | 0.5-5 |
| Anharmonic parameter | $\mu$ | Arbitrary | $\mu'$ | 0-0.5 |
| Nonlinear parameter | $\epsilon$ | 0.00658-0.065.8 eV | $\epsilon'$ | 1-10 |

Table 5.1 Values of the parameters used in the numerical simulations. Physical versus dimensionless values are reported.

## 5.4 Numerical results

All the numerical computations have been performed using an integration time step $\Delta t = 5 \times 10^{-5}$ entailing a very good energy conservation, with typical relative error $\Delta E/E \simeq 10^{-5}$. The length of the chain is $N = 500$ rounding the number of amino acids of the protein in [21]. Figures (5.1) and (5.2) show the spatial distribution of the probability $|\psi(n,t)|^2$ of finding the moving electron at any site $n$ versus time for the electron-phonon coupling $\chi = 100$ pN and $\chi = 366$ pN, respectively. The electron is initially centered around the site $n = 250$. Figure (5.1) shows that the electron wavefunction quickly spreads over the whole substate of amino acids, a phenomenon somewhat less pronounced in Figure (5.2) and to some extent counterintuitive since the latter corresponds to a stronger electron-phonon coupling.

Figure (5.3) shows the time evolution of random initial conditions for the displacements of the underlying chain of masses modelling the chain of amino acids of a protein. The random initial displacements and velocities are generated at thermal equilibrium at 310 K, according to the prescriptions of Eq.(5.27).

Electron and phonon energies, in the following Figures (5.4)-(5.7), are computed as expectation values of each Hamiltonian in Eqs.(5.2) and (5.3) along the time evolving state vector of the system according to Eqs. (2.55) and (5.16). From the latter equation, the energies of the electron and of the phonons are then obtained, respectively. Let us remark again that by

means of the TDVP variational method out of the formally classical evolution equations we get quantum expectation values of the observables. Figure (5.4) synoptically displays the energy transfer from the electron to the phonon subsystem. The same figure also shows that the larger $\chi$ the faster this energy transfer, what is physically sound and not necessarily at odds with what reported in Figures (5.1) and (5.2) about the electron wavefunction spreading.

As is seen from the plots in Figures (5.5), the value of the phonon-phonon coupling parameter $\mu'$ does not seem crucial to control the release of the electron energy to the phonons, the process appears to be mainly driven by the electron-phonon coupling constant. In fact, for $\chi = 488$ pN the relaxation time to the oscillatory state is quick and practically independent of the value of $\mu'$. Neither at the lower value $\chi = 61$ pN significative differences in the relaxation rate are observed by varying $\mu'$, and even for $\mu' = 0$ the energy transfer takes place in both cases of $\chi = 61$ pN and $\chi = 488$ pN. There are two distinct phenomena: first, the release of the electron energy to the whole ensemble of phonons, and, second, the sharing (thermalization) among the normal modes of the energy received in the first process. The rate of the first process is controlled by the coupling constant $\chi$, and the rate of the second process is controlled by the value of $\mu'$, as is clearly shown by Figures (5.9).

Then we have checked how the phenomenology changes as a consequence of the introduction of the nonlinear coupling in the electron Hamiltonian. In Figures (5.6) and (5.7) the effects of different values of the parameter $\epsilon$ are reported, again for $\chi = 61$ pN and $\chi = 488$ pN respectively. At $\chi = 61$ pN the electron energy relaxation is much slower than for $\chi = 488$ pN. In particular, for $\epsilon = 0$ meV the electron energy appears to oscillate in a rather narrow range of values with no evident tendency of a relaxation toward a value smaller than the initial one. Whereas, for non-vanishing values of $\epsilon'$ the electron energy is clearly decaying in time with some oscillations.

Figure (5.7) confirms what has already been reported in Figure (5.5), that is, for $\chi = 488$ pN the electron energy fastly decreases in time, even in the case of $\epsilon = 0$ meV.

Let us remark that a non-vanishing value of $\epsilon$, that is, the presence of the nonlinear coupling term in the electron Hamiltonian, plays a relevant role to ensure a more efficient transfer of part of the electron energy to the phonons of the chain of amino acids. But, in any case, it is the electron-phonon coupling constant which mainly rules the energy transfer process.

For any chosen set of physical parameters, except possibly for $\epsilon = 0$, the electron always

transfers part of its energy to the phonons, and eventually this energy is equally shared among the phonons. In order to work out the typical time scales of this thermalization process we have computed the spectral entropy of the normal modes of the chain of amino acids, that is, of the phonons. For the harmonic term $H_h$ of the dimensionless Hamiltonian (5.16) we have

$$\langle\psi|\hat{H}_h|\psi\rangle = \frac{1}{2}\sum_{n=1}^{N}\Big[\dot{b}_n^2 + \Omega'(b_{n+1}-b_n)^2\Big], \tag{5.28}$$

and then, by following Ref. [29], the coordinate transformations $Q_m = S_{mn}b_n$ and $P_m = S_{mn}\dot{b}_n$, with

$$S_{mn} = \frac{1}{\sqrt{N}}\Big[\cos(\frac{2\pi}{N}mn) + \sin(\frac{2\pi}{N}mn)\Big] \quad m,n = 1,2,..,N\ , \tag{5.29}$$

transform the Hamiltonian (5.28) into

$$\tilde{H}_h = \frac{1}{2}\sum_{m=1}^{N}(P_m^2 + \Omega^{'}\omega_m^2 Q_m^2), \tag{5.30}$$

where

$$\omega_m^2 = 4\sin^2(\frac{\pi m}{N}). \tag{5.31}$$

Of course, these oscillators are the normal modes (phonons) of the system. Then a spectral entropy $S(t)$ is defined as

$$S(t) = -\sum_{m=1}^{N} p_m(t)\ln p_m(t); \qquad p_m(t) = \frac{E_m(t)}{E_T(t)} \tag{5.32}$$

where $E_T(t) = \sum_{m=1}^{N} E_m(t)$ and $E_m(t) = (P_m^2 + \Omega^{'}\omega_m^2 Q_m^2)/2$, so that the weights $p_m(t)$ are normalized. The maximum value of $S(t)$ is attained when all the $p_m(t)$ are equal to $1/N$. Thus, at equipartition, when the energy content of each normal mode is the same, entropy attains its maximum. In principle, the complete Hamiltonian for the phonon part is

$$H_{ph}(P,Q) = \frac{1}{2}\sum_{m=1}^{N}(P_m^2 + \Omega'\omega_m^2 Q_m^2) + \mu\sum_{m,n,l,i=1}^{N} D_{mnli}Q_mQ_nQ_lQ_i\,, \tag{5.33}$$

and the equipartition theorem now would read

$$\left\langle Q_n \frac{\partial H_{ph}}{\partial Q_n} \right\rangle = \left\langle \Omega' \omega_n^2 Q_n^2 + Q_n \ \mu \sum_{m,l,i=1}^{N} D_{mnli} Q_m Q_l Q_i \right\rangle = f(E) \tag{5.34}$$

with $f(E)$ a function independent of the mode. Since we have $N = 500$, for each normal mode at each time step we should compute $125 \times 10^6$ terms in the sum for a total of $62.5 \times 10^9$ terms for each value of the spectral entropy at any time, and this is computationally prohibitive. On the other hand it has been shown [29, 69] that even considering only the harmonic energies the thermalization process can be actually detected, even if at energy equipartition $S(t)$ is not exactly equal to $S_{max}$.

A normalized entropy is then defined as

$$\eta(t) = \frac{S_{max}(t) - S(t)}{S_{max}(t) - S(0)}, \tag{5.35}$$

so that when the phonon oscillators are "frozen" it is $S(t) = S(0)$ and consequently $\eta = 1$; but at equipartition, when $S(t) = S_{max}(t)$, it is $\eta = 0$. By following the time decay of $\eta$, it is thus possible to find out if and on which time scale the energy released by the electron is definitely transferred to the phonons. In Figure (5.8) $\eta(t)$ is plotted as a function of time for various values of the coupling constant $\chi$ and keeping fixed the other parameters as in the case reported in Figure (5.1). It is evident that equipartition of energy is always attained, and the time needed for this to happen is rather weakly dependent on the electron-phonon coupling constant. In fact, the equipartition rate is controlled by $\mu'$ as can be seen in Figures (5.9). The case $\mu' = 0$ is special, in the sense that the phonon-phonon coupling is indirectly made by the nonlinear electron-phonon interaction, and, in fact, the comparison between the left and right panels of Figures (5.9) shows that for $\chi' = 4$ the decay pattern of $\eta(t)$ is suggestive of some tendency to thermalization, which is apparently absent (possibly very slow) for $\chi' = 0.5$. In fact, the decay time is approximately varying between 0.5 ns and 1 ns (the unit time scale being $10^{-13}$ seconds). Importantly, the two time scales, of the electron energy release to the amino acids and of equipartition of this energy among all the normal modes of the lattice, are not equal and need not to be equal. The chaotic behavior of the particles representing the amino-acids generically prevents the reversibility of the electron energy transfer to the phonons, but then the equipartition among the phonons of the energy received from the electron depends on

the phonon-phonon coupling strength and on the degree of chaoticity of the phonon dynamics [29, 69].

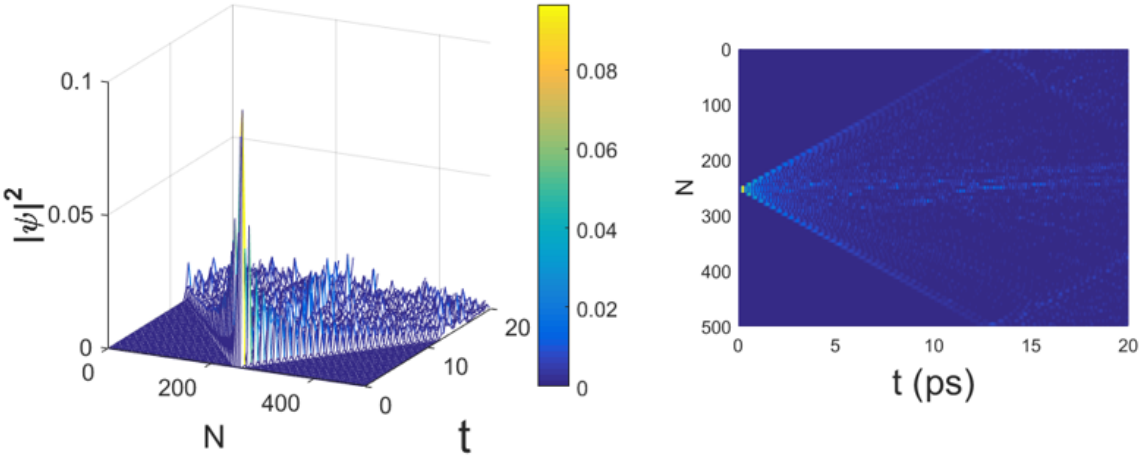


Figure 5.1 Evolution of the probability amplitude of an electron $|\psi(t)|^2$ along the chain of $N = 500$ amino acids. Initial conditions: $T = 310°$K, $E' = 30$, $J' = 10$, $\epsilon' = 5$, $\chi' = 0.8$, $\Omega' = 1.2$, $\mu' = 0.1$, corresponding to $E_0 = 0.2$ eV, $J = 0.0658$ eV, $\epsilon = 0.0329$ eV, $\chi = 100$ pN, $\Omega = 18.3$ N/m, respectively. The right figure is the above view of the left one. Time $t$ is measured in $10^{-13}$s.

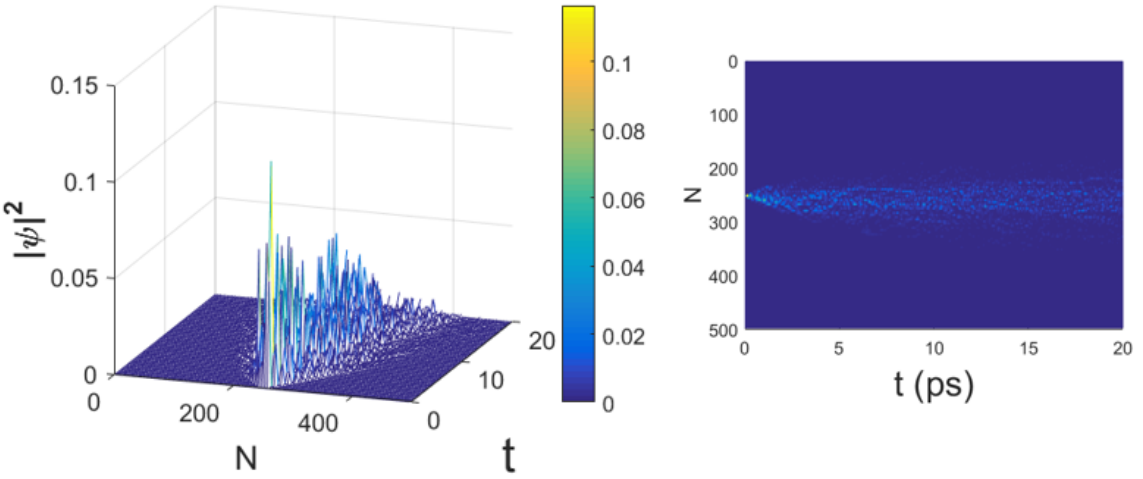


Figure 5.2 Evolution of the probability amplitude of an electron $|\psi(t)|^2$ with $N = 500$ and $\chi' = 3$ ($\chi = 366$ pN); the other parameters are the same of Fig. 5.1. Time $t$ is measured in $10^{-13}$s.

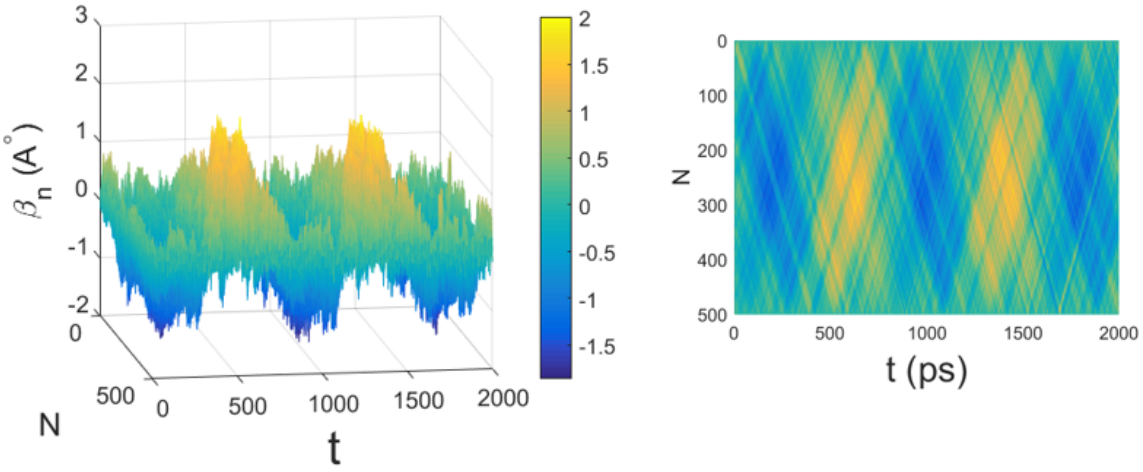


Figure 5.3 Time evolution of the average displacements along the chain of $N = 500$ amino acids. The parameter values are the same of Fig. 5.1. Time $t$ is measured in $10^{-13}$s.

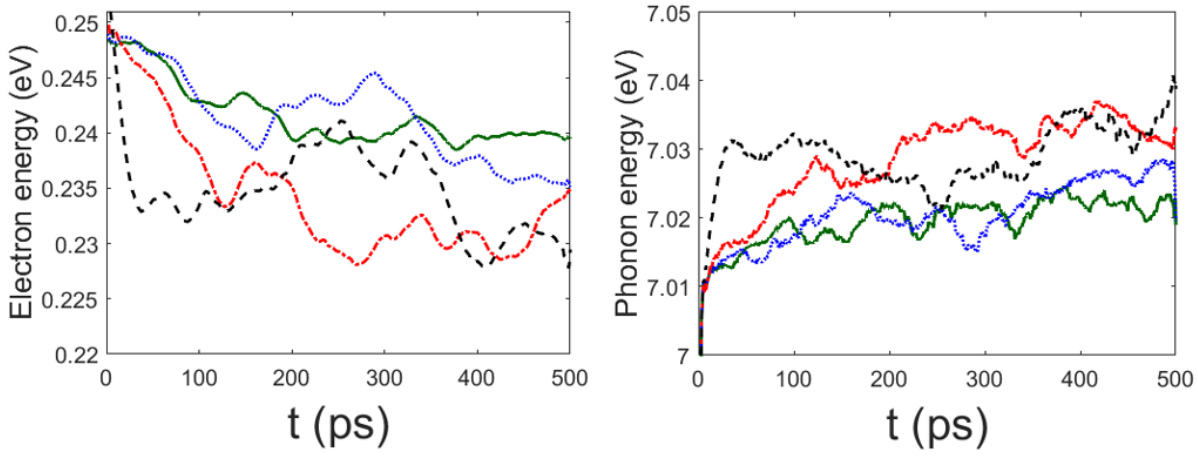


Figure 5.4 Time behavior of electron energy (left panel) and phonon energy (right panel) for $\chi' = 0.6$ ($\chi = 73.2$ pN) (green solid line), $\chi' = 0.8$ ($\chi = 100$ pN) (blue dotted line), $\chi' = 1$ ($\chi = 122$ pN) (red dot-dashed line), and $\chi' = 1.5$ ($\chi = 183$ pN) (black dashed line); the other parameters are the same of Fig. 5.1. Time $t$ is measured in $10^{-13}$s; electron energy and total phonon energy are given in eV.

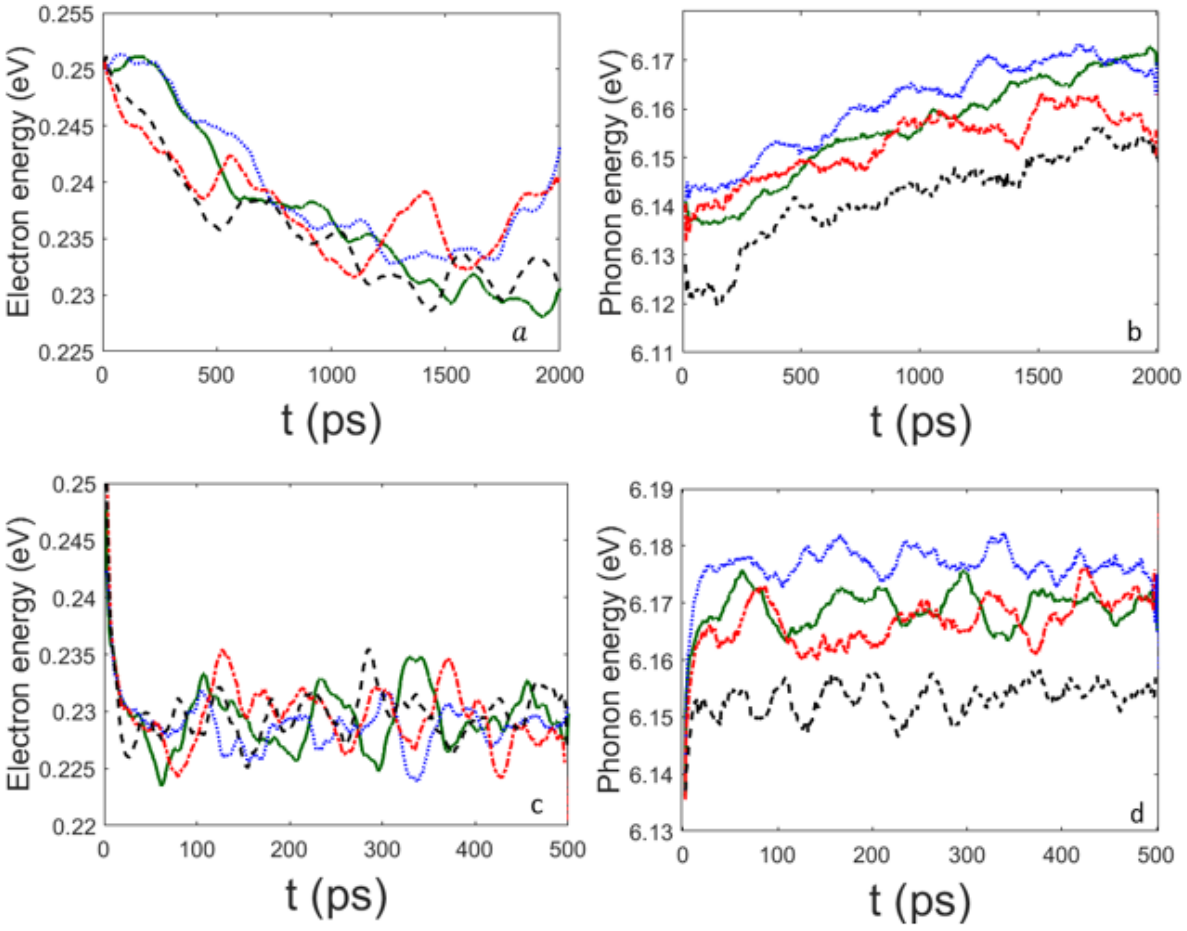


Figure 5.5 Time behavior of electron energy (left panels) and phonon energy (right panels). Upper panels refer to $\chi' = 0.5$ ($\chi = 61$ pN) and for: $\mu' = 0$ (green solid line), $\mu' = 0.1$ (blue dotted line), $\mu' = 0.3$ (red dot-dashed line), and $\mu' = 0.5$ (black dashed line). Lower panels refer to $\chi' = 4$ ($\chi = 488$ pN) and for: $\mu' = 0$ (green solid line), $\mu' = 0.1$ (blue dotted line), $\mu' = 0.3$ (red dot-dashed line), and $\mu' = 0.5$ (black dashed line). Time $t$ is measured in $10^{-13}$s; electron energy and total phonon energy are given in eV. The other parameters are the same of Fig. 5.1.

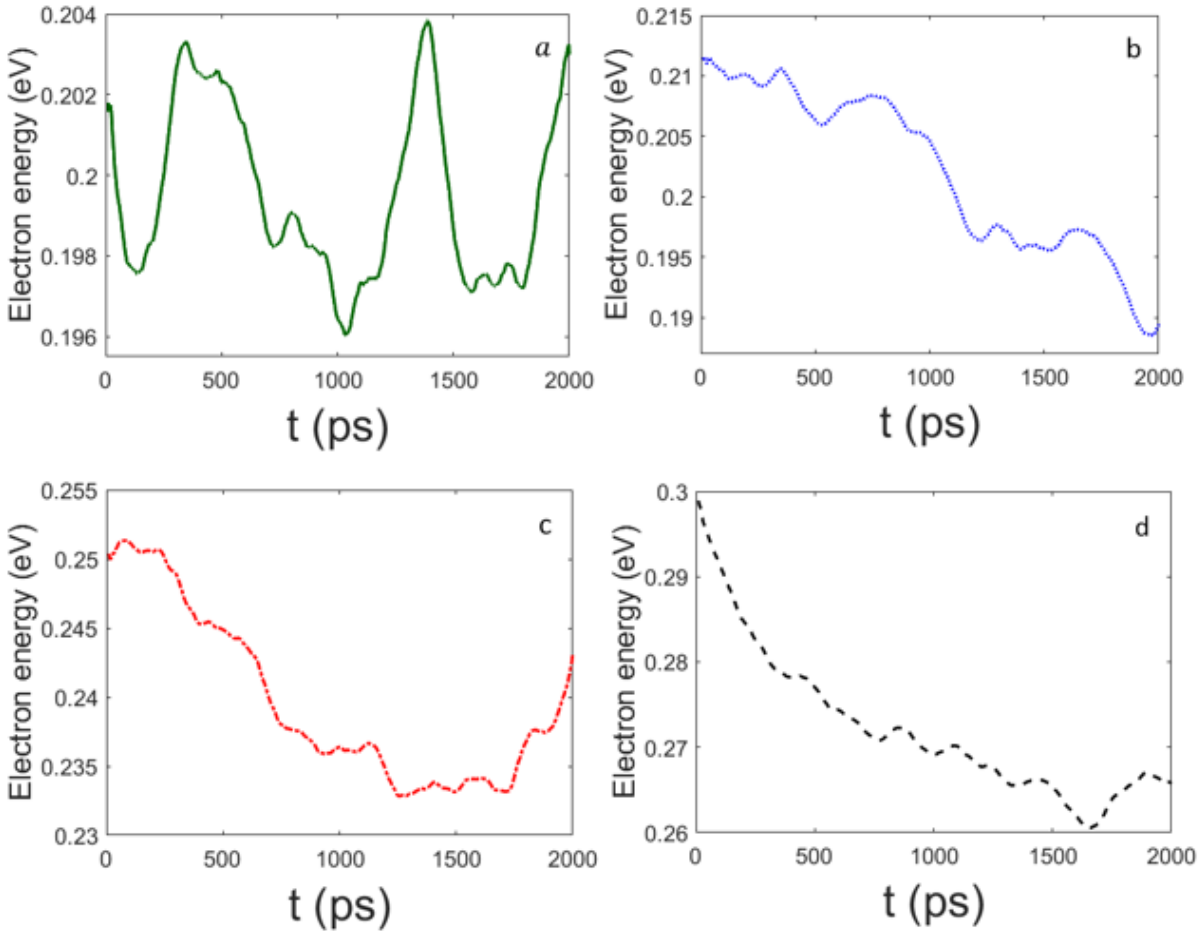


Figure 5.6 Decay of the electron energy for a) $\epsilon = 0$, b) $\epsilon' = 1$ ($\epsilon = 6.58$ meV), c) $\epsilon' = 5$ ($\epsilon = 32.9$ meV), and d) $\epsilon' = 10$ ($\epsilon = 65.8$ meV); the other parameters are the same of Fig. 5.1, but $\chi' = 0.5$ ($\chi = 61$ pN). Time $t$ is measured in $10^{-13}$s; electron energy is given in eV.

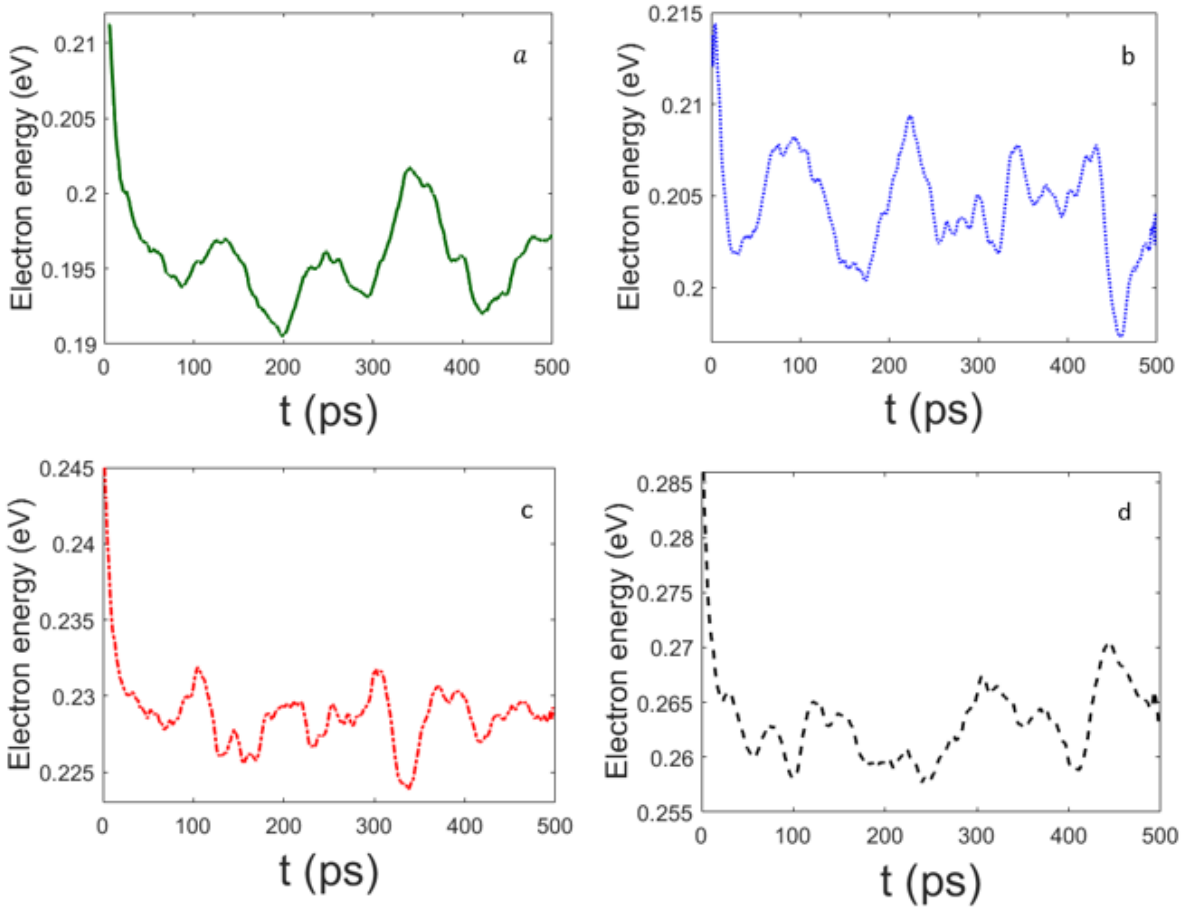


Figure 5.7 Decay of the electron energy for a) $\epsilon = 0$, b) $\epsilon' = 1$ ($\epsilon = 6.58$ meV), c) $\epsilon' = 5$ ($\epsilon = 32.9$ meV), and d) $\epsilon' = 10$ ($\epsilon = 65.8$ meV); the other parameters are the same of Fig. 5.1, but $\chi' = 4$ ($\chi = 488$ pN). Time $t$ is measured in $10^{-13}$s; electron energy is given in eV.

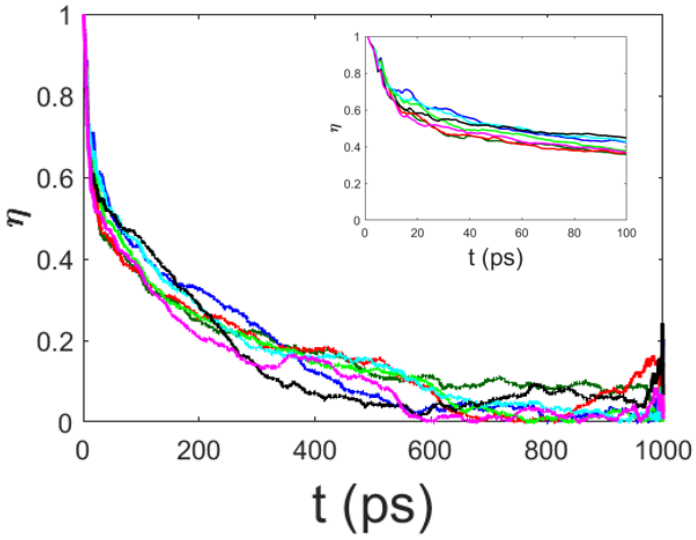


Figure 5.8 The spectral entropy $\eta$ is plotted vs time for $\chi' = 0.1$ ($\chi = 12.2$ pN) (dark green), $\chi' = 0.5$ ($\chi = 61$ pN) (dark blue), $\chi' = 1$ ($\chi = 122$ pN) (red), $\chi' = 2$ ($\chi = 244$ pN )( light green), $\chi' = 3$ ($\chi = 366$ pN) (light blue), $\chi' = 4$ ($\chi = 488$ pN) (black), and $\chi' = 5$ ($\chi = 610$ pN) (purple); the other parameters are the same of Fig. 5.1. Time $t$ is measured in $10^{-13}$s.

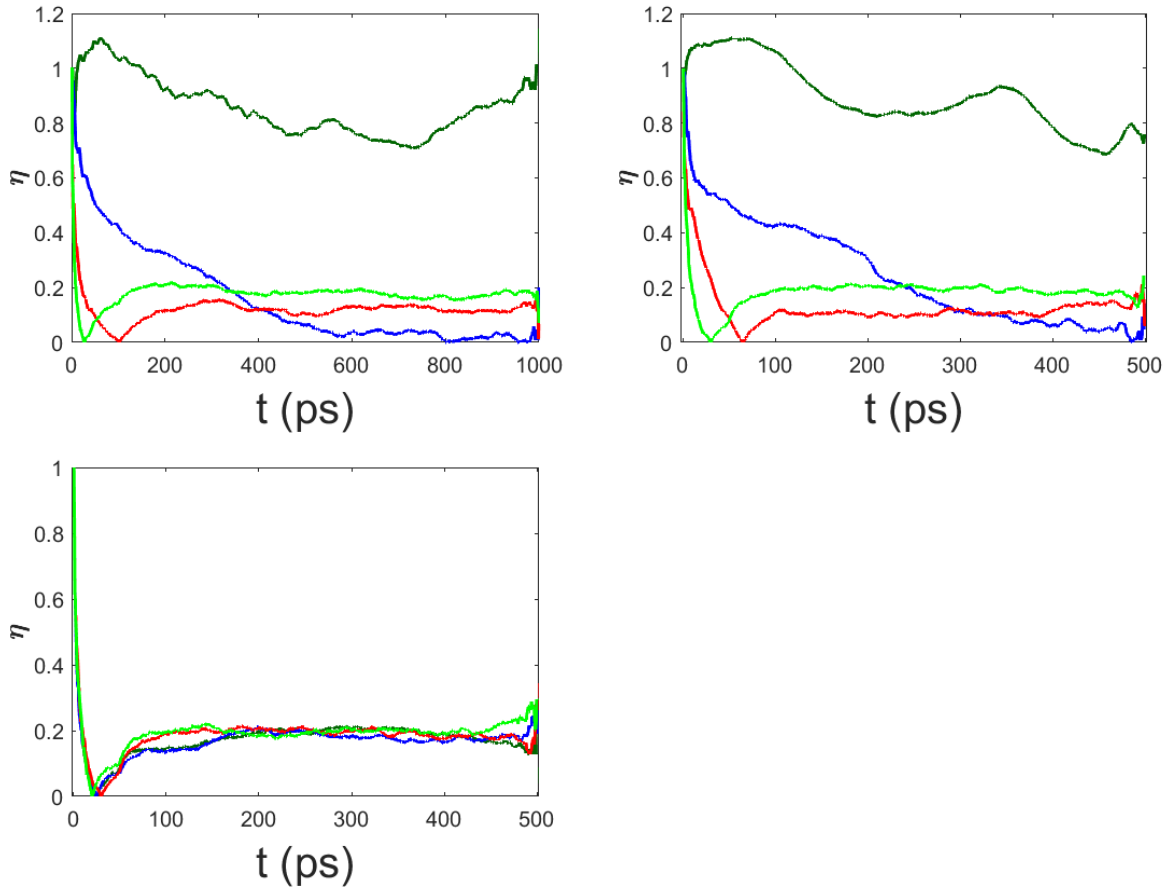


Figure 5.9 The spectral entropy $\eta$ is plotted vs time for different values of $\chi'$. Upper left panel : $\chi' = 0.5$ ($\chi = 61$ pN) and $\mu' = 0$ (dark green), $\mu' = 0.1$ (dark blue), $\mu' = 0.3$ (red), $\mu' = 0.5$ (light green). Upper right panel: $\chi' = 4$ ($\chi = 488$ pN), $\mu' = 0$ (dark green), $\mu' = 0.1$ (dark blue), $\mu' = 0.3$ (red), $\mu' = 0.5$ (light green). Lower panel: $\chi' = 4$ ($\chi = 488$ pN), $\mu' = 0.1$ and $\epsilon' = 0.$ (dark green), $\epsilon' = 1.$ (blue), $\epsilon' = 5.$ (red), $\epsilon' = 10.$ (light green).

Summarizing the physical meaning of the results reported in this chapter, we have to keep in mind that the parameter space of the system investigated here is very large, thus we have limited our investigation to a basic choice of physically meaningful parameters to tackle the fast process that we aimed at modeling, as stated in the Introduction. Then we have checked the robustness of the phenomenology so observed by changing some parameters, as is the case of the nonlinear coupling constants $\epsilon$ and $\mu$, or the electron-phonon coupling constant $\chi$. The numerical simulations of the evolution equations have shown that after having given 0.19 eV of initial excitation energy to an electron, the electron wave function spreads through the chain by

releasing to the phonons only a small fraction of the electron energy, approximately 0.02 eV. This is a somewhat unexpected result but physically interesting because it helps in understanding why exciting a collective intermolecular oscillation of the BSA protein required a very long time[21]. Of course, the contributions of several fluorophores add up, and the continuous illumination of the labeled proteins with an intense laser light allows to accumulate energy in the protein until the activation threshold of the coherent oscillation of all its atoms is reached and exceeded. The phonon part of the model tackled here has been simplified with respect to the model derived by the de-quantization of the original Fröhlich's model [19] because it is focused only on the fast mechanism of down-conversion of the energy of the photons, harvested by the protein through its fluorophore-receptors, to the internal vibrations of the chain of amino acids. Although no more than 10% of energy is dissipated by electron to phonons, in the studied regime no coherent transport of information can occur on the amino acids (as sometimes one could expect in a spin chain model [70] ) due to the fact that the electron wave function spreads over all sites.

# CHAPTER 6. Transition between Random and Periodic Electron Currents on a DNA Chain

The quotations given in Ref.[71], electron transport on DNA can be involved in the action of DNA damage response enzymes, transcription factors, or polymerase co-factors, which are relevant processes in the cell [71, 72]. For example, evidence has been given [71, 73] that a DNA base excision repair enzyme enters the DNA repair process [74, 75] through an electron transfer mechanism. Interestingly, electron transfer through damaged regions of DNA is markedly different with respect to electron transfer through healthy regions of DNA [74]. In [24] we investigate the spectral properties of an electron current generated along a segment of DNA. The reason for this study is to investigate how DNA can respond to external electromagnetic excitations and spectral properties of electron currents along DNA fragments.

## 6.1 Definition of the model and its solution

In order to describe electronic motions along a DNA fragment, and in perspective the related electrodynamic interactions, we resort to a model partly borrowed from the standard Davydov (2.2.2) and Holstein-Fröhlich models (2.2.1) and (4.2.2) that have been originally introduced to account for electron-phonon interaction. Thus, to model the electrons moving along a given DNA sequence, the following Hamiltonian operator according to the energy operator (2.15)is assumed [18, 67, 68]

$$\hat{H} = \hat{H}_{el} + \hat{H}_{ph} + \hat{H}_{int}, \tag{6.1}$$

where the electronic and phononic parts of the Hamiltonian are given by

$$\hat{H}_{el} = \sum_{n=1}^{N} \Big[ E_0 \hat{B}_n^\dagger \hat{B}_n + \epsilon \langle \hat{B}_n^\dagger \hat{B}_n \rangle \hat{B}_n^\dagger \hat{B}_n + J_n (\hat{B}_n^\dagger \hat{B}_{n+1} + \hat{B}_n^\dagger \hat{B}_{n-1}) \Big], \tag{6.2}$$

$$\hat{H}_{ph} = \frac{1}{2}\sum_n \Big[\frac{\hat{p}_n^2}{M_n} + \Omega_n(\hat{u}_{n+1} - \hat{u}_n)^2 + \frac{1}{2}\mu(\hat{u}_{n+1} - \hat{u}_n)^4\Big], \tag{6.3}$$

and the electron-phonon Hamiltonian reads as

$$\hat{H}_{int} = \sum_n \chi_n(\hat{u}_{n+1} - \hat{u}_n)\hat{B}_n^\dagger \hat{B}_n. \tag{6.4}$$

As shown in the following, the introduction of the site-dependent electron-phonon coupling constant $\chi_n$ brings about a definitely richer phenomenology with respect to the site-independent case [23]. The term $E_0\hat{B}_n^\dagger\hat{B}_n$ accounts for the initial "bare" electron energy distributed on several lattice sites according to initial shape of the electron wavefunction. The new constant $\epsilon$ is the nonlinear electron-electron coupling energy due to the interaction of the moving electron along the DNA molecule with the electrons of the substrate of nucleotides. Indeed, the nonlinear parameter $\epsilon$ accounts for the Coulomb repulsion between the traveling electron and the charges localized on the nucleotides. The site-dependent parameter $J_n$ determines the strength of the nearest neighbour coupling energies of the electron tunnelling across two neighbouring nucleotides.

The vibronic part takes into account the longitudinal displacements of the nucleotides from their equilibrium positions by the mass $M_n$ and by the site-dependent $\Omega_n$, the spring parameter of two neighbouring nucleotides. The parameter $\mu$ is the coupling constant of the nonlinear quartic term entailing the phonon-phonon interaction, of course absent in the harmonic approximation. The quartic term is introduced as a first (stable) term - beyond the harmonic approximation - in the power-law expansion around the minimum of typically nonlinear interparticle interaction potential (e.g. as is the case of Van der Waals potentials). The parameter $\chi_n$ is the site-dependent coupling parameter of the electron-lattice interaction.

Here we show how the quantum equations of motion for the Hamiltonian (6.1) can be derived using the time dependent variational principle (TDVP) in quantum mechanics (2.3). First, we work with the second of Davydovs ansatz state vectors (2.19) by assuming the factorization (2.20) describing an electron given a single quantum excitation propagating along the sequence of $N$ nucleotides composing a DNA and (2.35) of the phononic wave function:

$$|\psi(t)\rangle = |\Psi(t)\rangle|\Phi(t)\rangle; \tag{6.5}$$

According to TDVP, we introduce a new wave function(2.54)- in terms of $|\psi(t)\rangle$ in Eq. (6.5). Then from Eqs. (6.5), (2.20), and (2.35) we have

$$\partial_t|\psi\rangle = (\partial_t|\Psi\rangle)\,|\Phi\rangle + |\Psi\rangle\,(\partial_t|\Phi\rangle)\,, \tag{6.6}$$

which gives

$$\langle\psi|\partial_t|\psi\rangle = \sum_n \left[\dot{C}_n(t)C_n^*(t) + \frac{i}{2\hbar}\Big(\dot{\pi}_n(t)\beta_n(t) - \pi_n(t)\dot{\beta}_n(t)\Big)\right]. \tag{6.7}$$

Hence with the Lagrangian (2.58) we obtain

$$\begin{aligned} L \;= \sum_n \Big(& i\hbar\dot{C}_n(t)C_n^*(t) + \frac{1}{2}\Big(\pi_n(t)\dot{\beta}_n(t) - \dot{\pi}_n(t)\beta_n(t)\Big) \\ & -H(C_n, C_n^*, \beta_n, \pi_n)\Big), \end{aligned} \tag{6.8}$$

where

$$\sum_n H(C_n, C_n^*, \beta_n, \pi_n) = \langle\psi(t)|\hat{H}|\psi(t)\rangle. \tag{6.9}$$

By requiring the fulfillment of the stationary action condition of Equation (2.59) we have

$$\begin{aligned} \delta S(t) \;=\; & \sum_n \Big\{ i\hbar\Big( - \dot{C}_n^*(t)\delta C_n(t) + \dot{C}_n(t)\delta C_n^*(t)\Big) \\ & + \;\dot{\beta}_n(t)\delta\pi_n(t) - \dot{\pi}_n(t)\delta\beta_n(t) \\ & - \;(\partial_{C_n}H)\delta C_n - (\partial_{C_n^*}H)\delta C_n^* \\ & - \;(\partial_{\beta_n}H)\delta\beta_n - (\partial_{\pi_n}H)\delta\pi_n\Big\} = 0, \end{aligned} \tag{6.10}$$

and arrive at the dynamical equations

$$\begin{aligned} i\hbar\dot{C}_n &= \partial_{C_n^*}H \\ \dot{\beta}_n &= \partial_{\pi_n}H \\ \dot{\pi}_n &= -\partial_{\beta_n}H\ . \end{aligned} \tag{6.11}$$

The expectation value of the Hamiltonian is

$$\begin{aligned}\langle\psi|\hat{H}|\psi\rangle &= \sum_n \Big[E_0|C_n|^2 + \epsilon|C_n|^4 + J_n(C_n^* C_{n+1} + C_{n+1}^* C_n) \\ &+\frac{1}{2}\Big(\frac{1}{M_n}\pi_n^2 + \Omega_n(\beta_{n+1}-\beta_n)^2 + \frac{1}{2}\mu(\beta_{n+1}-\beta_n)^4\Big) \\ &+\chi_n(\beta_{n+1}-\beta_n)|C_n|^2\Big]. \end{aligned} \tag{6.12}$$

Thus, from (6.11) and (6.12), we find the following explicit form of the equations of motion

$$\begin{aligned} i\hbar\dot{C}_n &= \Big(E_0 + 2\epsilon|C_n|^2 + \chi_n(\beta_{n+1}-\beta_n)\Big)C_n + J_n C_{n+1} + J_{n-1}C_{n-1}, \\ M_n\ddot{\beta}_n &= \Omega_n\beta_{n+1} + \Omega_{n-1}\beta_{n-1} - \Omega_{n-1}\beta_n - \Omega_n\beta_n + \chi_n|C_n|^2 - \chi_{n-1}|C_{n-1}|^2 \\ &+ \mu\Big((\beta_{n+1}-\beta_n)^3 - (\beta_n-\beta_{n-1})^3\Big). \end{aligned} \tag{6.13}$$

## 6.2 Physical parameters

In order to choose meaningful physical coupling parameters of the Hamiltonian, we borrow from Ref.[60, 61] the values of the interaction energy between an electron and each of all the 4 nucleotides (reported in Table (4.1)). We assume that the moving electron - of initial energy $E_0$ - moves along the sequence of nucleotides constituting a given segment of DNA by tunneling across square potential barriers of variable height and of width $a = 3.4\mathring{A}$, the average distance between two nearest neighbouring nucleotides [18]. We introduce the transmission coefficients $T_{n,n+1}$ from the probability $P(n \to n \pm 1)$ of tunneling from one potential well to the nearest one in order to set the electron hopping terms $J_n$ in (6.2)

$$T_{n,n+1} = \left[1 + \frac{E_{n+1}^2 \sinh^2(\beta_{n+1}a)}{4E_0(E_{n+1}-E_0)}\right]^{-1} \tag{6.14}$$

where $\beta_{n+1} = [2m_e(E_{n+1}-E_0)/\hbar^2]^{1/2}$, $m_e$ is the mass of electron and $E_{n+1}$ are the interaction energies between the moving electron and the local nucleotide. Then we assume

$$J_n = E_0 T_{n,n+1}. \tag{6.15}$$

For the interaction Hamiltonian (6.4) we can roughly estimate the electron-phonon coupling parameter $\chi_n$ as

$$\chi_n = dE/dx = \frac{E_{n+1} - E_n}{a}. \tag{6.16}$$

Numerical simulations are performed by adopting dimensionless physical parameters in the dimensionless expressions of the Hamiltonian (6.12) and of the dynamical equations (6.13). These are found, similar to (5.17), by rescaling time and lengths as $t = \omega^{-1}\tau$ and $\beta_n = Lb_n$, respectively, where $L = \sqrt{\hbar\omega^{-1}M_n^{-1}}$. The outcomes are

$$\begin{aligned}\langle\psi|\hat{H}|\psi\rangle = \sum_n \Big[ & E'|C_n|^2 + \epsilon'|C_n|^4 + J'_n(C_n^* C_{n+1} + C_{n+1}^* C_n) \\ & + \frac{1}{2}\Big(\dot{b}_n^2 + \Omega'_n(b_{n+1} - b_n)^2 + \frac{1}{2}\mu'(b_{n+1} - b_n)^4\Big) \\ & + \chi'_n(b_{n+1} - b_n)|C_n|^2\Big],\end{aligned} \tag{6.17}$$

and

$$\begin{aligned} i\frac{dC_n}{d\tau} &= \Big(E' + 2\epsilon'|C_n|^2 + \chi'_n(b_{n+1} - b_n)\Big)C_n + J'_n C_{n+1} + J'_{n-1}C_{n-1}, \\ \frac{d^2 b_n}{d\tau^2} &= \Omega'_n b_{n+1} + \Omega'_{n-1}b_{n-1} - \Omega'_{n-1}b_n - \Omega'_n b_n + \chi'_n|C_n|^2 - \chi'_{n-1}|C_{n-1}|^2 \\ &+ \mu'\Big[(b_{n+1} - b_n)^3 - (b_n - b_{n-1})^3\Big], \end{aligned} \tag{6.18}$$

where

$$\begin{aligned} E' &= \frac{E_0}{\hbar\omega}; \qquad \epsilon' = \frac{\epsilon}{\hbar\omega}; \qquad J'_n = \frac{J_n}{\hbar\omega}; \\ \chi'_n &= \frac{\chi_n}{\sqrt{\hbar M_n\omega^3}}; \qquad \Omega'_n = \frac{\Omega_n}{M_n\omega^2}; \qquad \mu' = \frac{\mu\hbar}{M_n^2\omega^3}\ . \end{aligned} \tag{6.19}$$

In our simulations we resort to the known sound speed $V = a(\Omega_n/M_n)^{1/2}$ on DNA; we borrow the value $V = 1.69$ km/s from [76], and take it as an average constant (neglecting small local variations due to the different masses of the nucleotides). Thus we obtain the constant dimensionless parameter $\Omega' = V^2/a^2\omega^2$ from (6.19). In re-writing the dynamical equations we

introduce the variables

$$q_n = \frac{C_n + C_n^*}{\sqrt{2}}, \qquad p_n = \frac{C_n - C_n^*}{i\sqrt{2}} \ , \tag{6.20}$$

so that Eqs.(6.18) become

$$\dot{q}_n = \Big[E' + \frac{\epsilon'}{2}(q_n^2 + p_n^2) + \chi'(b_{n+1} - b_n)\Big]p_n + J'_n p_{n+1} + J'_{n-1} p_{n-1}, \tag{6.21}$$

$$\dot{p}_n = -\Big[E' + \frac{\epsilon'}{2}(q_n^2 + p_n^2) + \chi'(b_{n+1} - b_n)\Big]q_n + J'_n q_{n+1} + J'_{n-1} q_{n-1}\Big], \tag{6.22}$$

$$\begin{aligned}\ddot{b}_n &= \Omega'(b_{n+1} + b_{n-1} - 2b_n) + \frac{1}{2}\Big(\chi'_n(q_n^2 + p_n^2) - \chi'_{n-1}(q_{n-1}^2 + p_{n-1}^2)\Big) \\ &\quad + \mu'\Big[(b_{n+1} - b_n)^3 - (b_n - b_{n-1})^3\Big] \\ &= \mathcal{B}_n[\mathbf{b}(t), \mathbf{q}(t), \mathbf{p}(t)] \ .\end{aligned} \tag{6.23}$$

where the equation for $\ddot{b}_n$ can be also written as

$$\begin{aligned}\dot{b}_n &= \pi_n \\ \dot{\pi}_n &= \mathcal{B}_n[\mathbf{b}(t), \mathbf{q}(t), \mathbf{p}(t)] \ .\end{aligned} \tag{6.24}$$

Finally, by combining a leap-frog scheme for (6.24) and a finite differences scheme for $\dot{q}_n$ and $\dot{p}_n$, equations (6.21)-(6.23) are rewritten in a form suitable for numerical solution, that is

$$\begin{aligned}q_n(t + \Delta t) &= q_n(t) + \Delta t \ \mathcal{Q}_n[\mathbf{b}(t), \mathbf{q}(t), \mathbf{p}(t)], \\ p_n(t + \Delta t) &= p_n(t) + \Delta t \ \mathcal{P}_n[\mathbf{b}(t), \mathbf{q}(t), \mathbf{p}(t), \\ b_n(t + \Delta t) &= b_n(t) + \Delta t \ \pi_n(t), \\ \pi_n(t + \Delta t) &= \pi_n(t) + \Delta t \ \mathcal{B}_n[\mathbf{b}(t + \Delta t), \mathbf{q}(t + \Delta t), \mathbf{p}(t + \Delta t)],\end{aligned} \tag{6.25}$$

where $\mathcal{Q}_n[\mathbf{b}(t), \mathbf{q}(t), \mathbf{p}(t)]$ and $\mathcal{P}_n[\mathbf{b}(t), \mathbf{q}(t), \mathbf{p}](t)$ are the r.h.s. of Eqs.(6.21) and (6.22), respectively. The integration scheme for $b_n(t)$ and $\pi_n(t)$ is a symplectic one, meaning that all the Poincaré invariants of the associated Hamiltonian flow are conserved, among these invariants there is energy. The simple leap-frog scheme cannot be applied to the equations for $\dot{q}_n(t)$ and $\dot{p}_n(t)$ because the r.h.s. of the equations for $\dot{q}_n(t)$ explicitly depend on $q_n(t)$ and $b_n(t)$, therefore

the first two equations in (6.25) are integrated with an Euler predictor-corrector to give

$$\begin{aligned}
q_n^{(0)}(t+\Delta t) &= q_n(t) + \Delta t\ \mathcal{Q}_n[\mathbf{b}(t), \mathbf{q}(t), \mathbf{p}(t)], \\
p_n^{(0)}(t+\Delta t) &= p_n(t) + \Delta t\ \mathcal{P}_n[\mathbf{b}(t), \mathbf{q}(t), \mathbf{p}(t)], \\
q_n^{(1)}(t+\Delta t) &= q_n(t) + \frac{\Delta t}{2}\left\{\mathcal{Q}_n[\mathbf{b}(t), \mathbf{q}(t), \mathbf{p}(t)] + \mathcal{Q}_n[\mathbf{b}(t), \mathbf{q}^{(0)}(t+\Delta t), \mathbf{p}^{(0)}(t+\Delta t)]\right\}, \\
p_n^{(1)}(t+\Delta t) &= p_n(t) + \frac{\Delta t}{2}\left\{\mathcal{P}_n[\mathbf{b}(t), \mathbf{q}(t), \mathbf{p}(t)] + \mathcal{P}_n[\mathbf{b}(t), \mathbf{q}^{(0)}(t+\Delta t)), \mathbf{p}^{(0)}(t+\Delta t)]\right\}, \\
b_n(t+\Delta t) &= b_n(t) + \Delta t\ \pi_n(t), \\
\pi_n(t+\Delta t) &= \pi_n(t) + \Delta t\ \mathcal{B}_n[\mathbf{b}(t+\Delta t), \mathbf{q}^{(1)}(t+\Delta t), \mathbf{p}^{(1)}(t+\Delta t)],
\end{aligned} \tag{6.26}$$

so that, thanks to fact that half of the set of the dynamical equations (6.25) is integrated by means of a symplectic algorithm, and half of the equations are integrated by means of the Euler predictor-corrector, it turns out that by adopting sufficiently small integration time steps $\Delta t$ the total energy is very well conserved without any drift, just with zero-mean fluctuations around a given value fixed by the initial conditions. Regarding initial conditions, independently of the specific excitation mechanism, we assume an electron wave function described by the amplitudes (2.48) centered at the excitation site $n = n_0$ and distributed at time $t = 0$ with initial velocity $v = 0$ as [18]

$$C_n(t=0) = \frac{1}{\sqrt{8\sigma_0}}\mathrm{sech}\Big(\frac{n-n_0}{4\sigma_0}\Big). \tag{6.27}$$

Regarding the initial conditions of the phonon part of the system, we assume the same condition of (5.26) so that the components of the DNA fragment under consideration are initially thermalized at the room temperature $T = 310K$, therefore

$$\langle|b_n(0)|\rangle_n = \sqrt{\frac{k_B T}{\hbar\omega\Omega'}}; \qquad\qquad \langle|\dot{b}_n(0)|\rangle_n = \sqrt{\frac{k_B T}{\hbar\omega}}. \tag{6.28}$$

expressed in dimensionless form. Periodic boundary conditions have been used for the both electron and phonon parts of the system.

## 6.3 Numerical results

In numerical simulations, we have adopted an integration time step $\Delta t = 5 \times 10^{-6}$ (dimensionless units) entailing a very good energy conservation with typical fluctuations of relative amplitude $\Delta E/E \simeq 10^{-6}$.

In what follows, we report the results obtained for two sequences of $N = 66$ and $N = 398$ nucleotides, respectively, for different initial electron energies $E_0$, and for initial excitation sites $n_0$ entering the initial wavefunction shape (6.27).

The physical quantity of interest in what follows is the Fourier spectrum of the electron current activated on a segment of DNA. The average electron current is derived from the standard probability current $j(x_i, t)$ associated with the wave function $|\psi(t)\rangle$ in (2.20) with probability amplitude (6.27), which, in the discretized version along the chain of nucleotides and thus ready for its numerical computation, reads as

$$\begin{aligned} j(x_i,t) &= \frac{e\hbar}{2m_e i}\Big(\Psi^*(x_i,t)\frac{\Psi(x_{i+1},t)-\psi(x_{i-1},t)}{2a} \\ &- \Psi(x_i,t)\frac{\Psi^*(x_{i+1},t)-\Psi^*(x_{i-1},t)}{2a}\Big), \end{aligned} \tag{6.29}$$

and hence the average current

$$i_{av}(t) = \frac{1}{l}\int_0^l j(x,t)dx = \frac{1}{Na}\sum_{i=1}^{N} j(x_i,t)a \ . \tag{6.30}$$

In Figures 6.1 - 6.4 the outcomes are reported of the simulations performed for a DNA sequence coding for a subunit of the human haemoglobin molecule (HBB) consisting of $N = 398$ nucleotides ( See Appendix A). Figures 6.1 and 6.2 display the behaviour of the system when $E_0 = 0.658$ eV and for $n_0 = N/2$ and $n_0 = N/3$, respectively. Remarkably, the mean electron current is alternate in what it takes positive and negative values, however, the corresponding Fourier power spectra appear very different according to the initial excitation site. In fact, for $n_0 = N/3$ it is well evident that the spectrum $|\tilde{i}(\nu)|^2$ is peaked around the frequency $\nu \simeq 5$ THz, whereas for $n_0 = N/2$ the spectrum appears much broader and noisy.

Then, by comparing the results obtained keeping the initial excitation around the site $n_0 = N/3$ but increasing the energy to $E_0 = 0.79$ eV, an interesting and to some extent surprising result is found: the power spectrum of the current gets sharper and peaked around $\nu \simeq 44$ THz,

a much higher frequency indeed. This is shown in Figure 6.3.

On the other hand, with the initial excitation again localized around the site $n_0 = N/2$ and with a lower initial activation energy, $E_0 = 0.46$ eV, Figure 6.4 shows that the electron wave function quickly spreads over the whole chain of nucleotides and the electron current power spectrum broadens with respect to that one found for $E_0 = 0.658$ eV in Figure (6.1). Of course, the parameter space of the system is very large and thus its systematic investigation is practically unfeasible. Nevertheless, the above reported results outline the existence of a richer phenomenology with respect to the excitation of just Davydov electro-solitons. This could be of interest in view of modelling specific processes involving electrodynamic interactions of DNA with other biomolecules or with external electromagnetic fields.

Panels (b) of the different figures show the time evolution of random initial conditions for the displacements of the underlying sequences of masses modelling nucleotides of the DNA. According to the prescriptions of Eq. (6.28), the random initial displacements and velocities are made at thermal equilibrium at $310^\circ$ K.

In Figures 6.5 - 6.8 the results are reported of numerical simulations obtained for a shorter sequence of $N = 66$ nucleotides [77] (See Appendix B). These results confirm the richness of the phenomenology previously observed for the longer DNA sequence. The spatial distribution of the probability $|\Psi(x,t)|^2$ in Fig. 6.5 where $E_0 = 0.2$ eV and $n_0 = N/3$ seems completely frozen in time even though some low amplitude ripple exists which entail a non-vanishing electron current; the power spectrum $|\tilde{i}(\nu)|^2$ shows some peaks concentrated in the frequency interval $5-10$ THz. By increasing the initial excitation energy of the electron at 0.6 eV, and keeping the excitation centered at the same site $n_0 = N/3$, we can see in Figure 6.6 a quick and complete spreading of the electron wave function $|\Psi(x,t)|^2$ and, correspondingly, a broad and noisy power spectrum of the electron current. A further increase of the electron excitation energy at $E_0 = 0.9$ eV, with the initial wavefunction centered at the site $n_0 = N/2$, brings about a well evident ripple of $|\Psi(x,t)|^2$ around its initial peak, as it can be seen in Figure (6.7)a. The associated electron current power spectrum turns out to be extremely peaked around 2.5 THz. Then, keeping the initial electron energy at $E_0 = 0.9$ eV but displacing the initial excitation around the site $n_0 = 2N/3$ it is observed that the peak value of the electron wavefunction decreases much faster than in the previous case ($n_0 = N/2$) and also the power spectrum of the current is very different from the previous case, displaying a broad and noisy pattern, as can be seen in

Figure (6.8).

A complementary characterization of the electron current power spectra can be performed by means of spectral entropy. This is defined *à la* Shannon as follows

$$S(t) = -\sum_{m=1}^{M/2} w_m(t) \ln w_m(t); \qquad w_m(t) = \frac{E_m(t)}{E_T(t)} \tag{6.31}$$

the weights $w_m(t)$ are normalized by

$$E_T(t) = \sum_{m=1}^{M/2} E_m(t); \qquad E_m(t) = \nu_m^2 |\tilde{i}(\nu_m)|^2 \tag{6.32}$$

where $\tilde{i}(\nu_m)$ indicates the Fourier transform of the electron current. The frequencies are $\nu_m = m/T = m/(M\Delta T)$ where $T$ is the length of time window which is Fourier analyzed, $\Delta T$ is a sampling time such that $T = M\Delta T$. As the input signals are real numbers and the Fourier spectra are computed through DFT algorithm we ignore the mirror part of the spectra thus ignoring the second half of the FFT. Then the spectral entropy is normalized to give

$$\eta(t) = \frac{S_{max}(t) - S(t)}{S_{max}(t)} \tag{6.33}$$

so that it is $\eta = 1$ when the power spectrum of the electron current is monochromatic, and $\eta = 0$ for a flat spectrum such that $S(t) = S_{max}(t)$. Figure 6.9 shows the normalized entropy $\eta$ of the electrons versus the initial energy $E_0$. In panel (a) $\eta$ versus $E_0$ is reported for the longer DNA segment under different initial conditions: for $n_0 = N/2$ the normalized entropy $\eta$ takes values approximately in the interval $0.1 - 0.15$ meaning that the corresponding power spectra are broad and noisy; for initial excitation site $n_0 = N/3$ it is found $\eta = 0.45$ at $E_0 = 0.79$ eV and we recover what has been already displayed by Figure 6.3, that is, the power spectrum is narrow in frequency; intermediate values of $\eta$ are found when the excitation site is $n_0 = 2N/3$ at energies $E_0 = 0.66, 0.79, 0.9$ eV.

In panel (b) $\eta$ versus $E_0$ is reported for the shorter DNA segment and synoptically shows the nontrivial appearance of some kind of, loosely speaking, "resonances" in what $\eta$ displays some bumps in its $E_0$-pattern which correspond to a significant narrowing of the electron current spectra, and thus to a less noisy and more coherent behaviour of the electron current.

The novelty of the model investigated in this chapter concerns the introduction of site de-

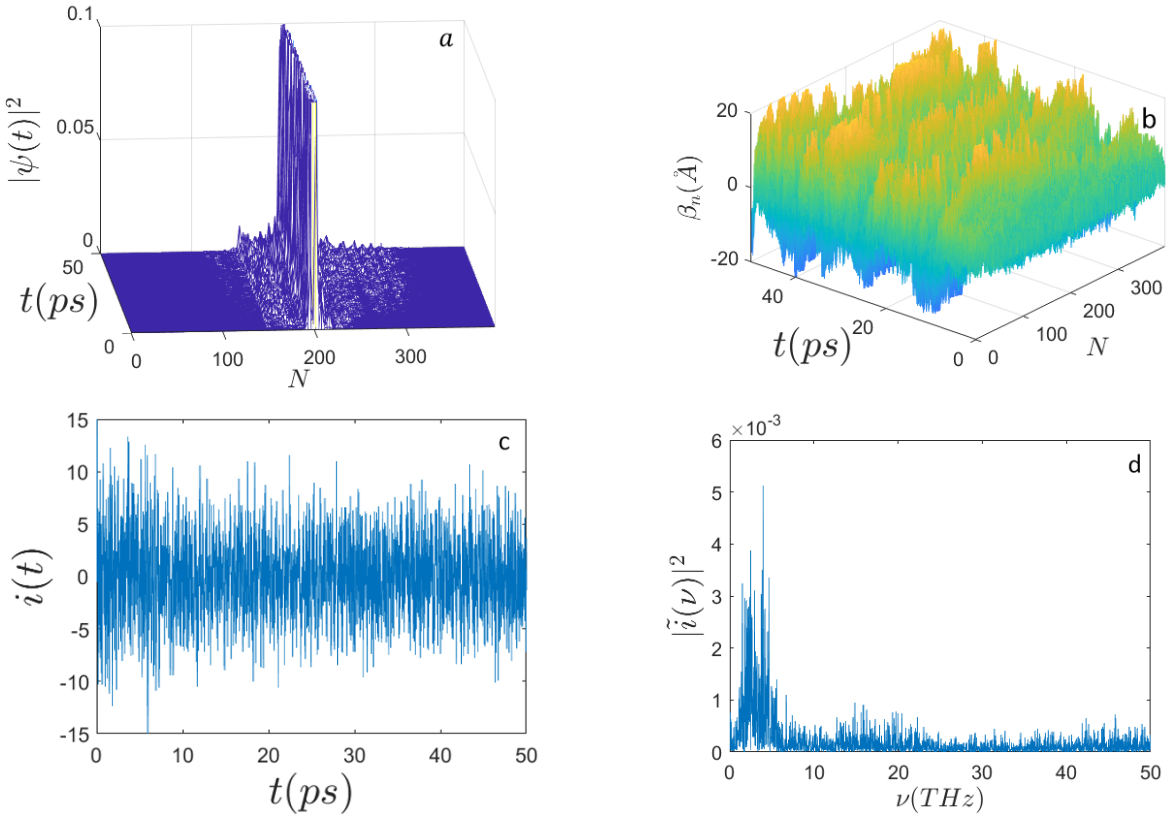


Figure 6.1 Time evolution of: a) the electron probability amplitude $|\Psi(t)|^2$; b) the average displacements $\beta_n(\AA)$; c) the electron current $i(t)$ (expressed in $\mu$biot); d) the frequency spectrum $|\tilde{i}(\nu)|^2$ along the sequence of $N = 398$ nucleotides. Initial conditions: $T = 310^{\circ}$K, $n_0 = N/2$, $E' = 100$, $\epsilon' = 5$, $\Omega' = 0.25$, $\mu' = 0.5$, $\sigma_0 = 0.1$, and the site-dependent parameters $J'_n$, and $\chi'_n$ corresponding to $E_0 = 0.658$ eV, $\epsilon = 0.0329$ eV, $\Omega_n = V^2 M_n/a^2$, $J_n$, and $\chi_n$ in Eqs. (6.15) and (6.16), respectively. Initial electron excitation peaked around the site $n_0 = N/2$.

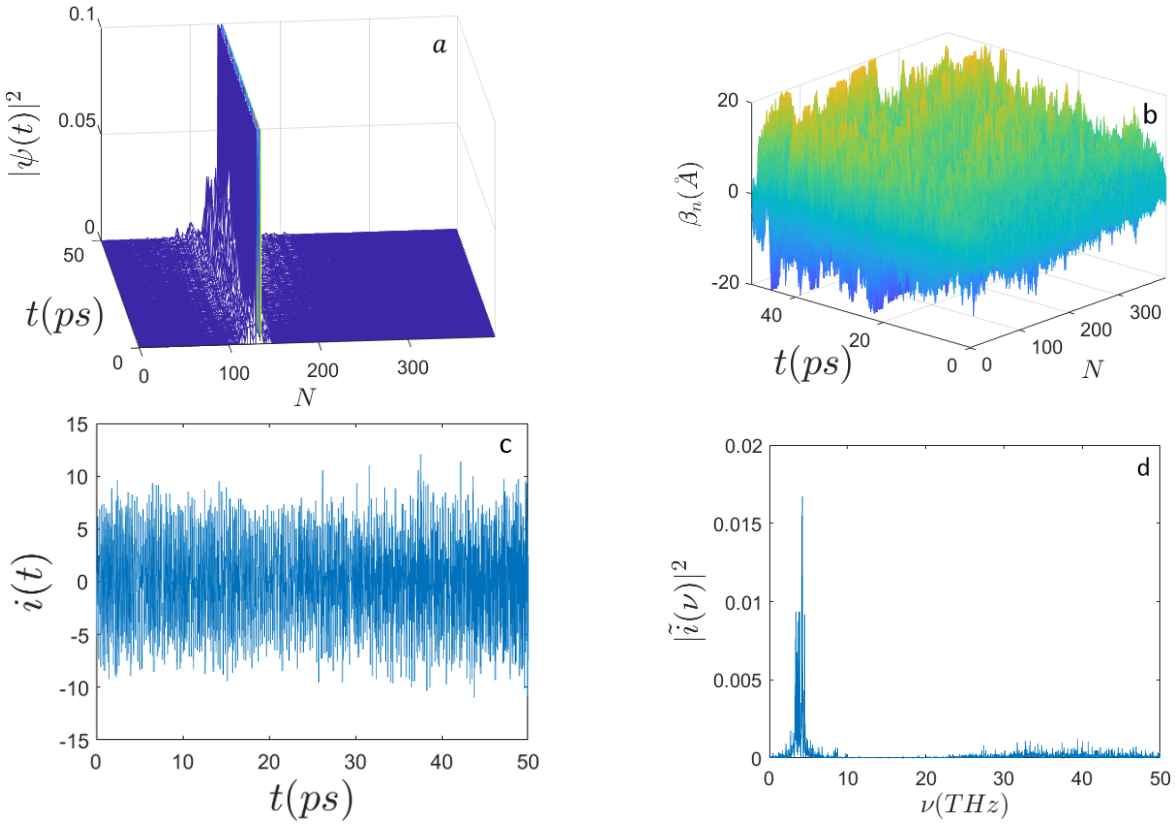


Figure 6.2 Time evolution of: a) the electron probability amplitude $|\Psi(t)|^2$; b) the average displacements $\beta_n(\mathring{A})$; c) the electron current $i(t)$ (expressed in $\mu$biot); d) the frequency spectrum $|\tilde{i}(\nu)|^2$ along the sequence of $N = 398$ nucleotides. Initial conditions and parameters are the same of Fig. 6.1 but the initial electron excitation is peaked around the site $n_0 = N/3$.

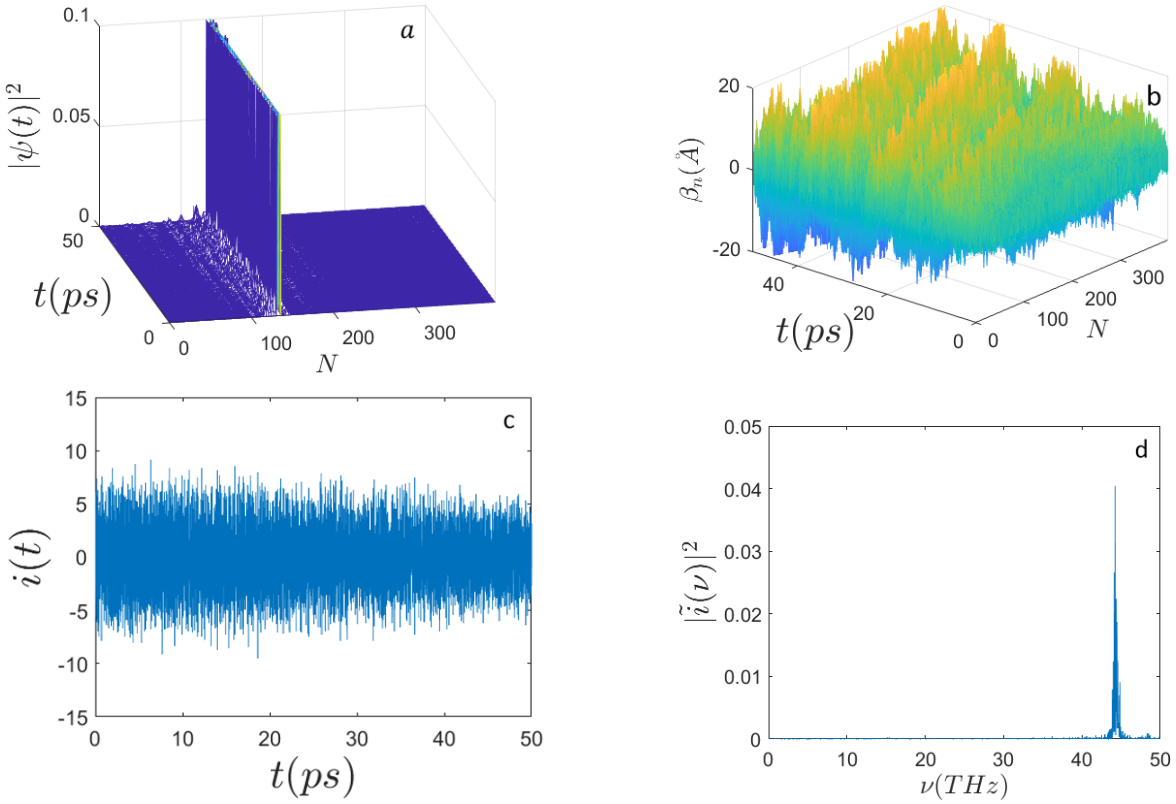


Figure 6.3 Time evolution of: a) the electron probability amplitude $|\Psi(t)|^2$; b) the average displacements $\beta_n(\mathring{A})$; c) the electron current $i(t)$ (expressed in $\mu$biot); d) the frequency spectrum $|\tilde{i}(\nu)|^2$ along the sequence of $N = 398$ nucleotides, with the initial condition $E_0 = 0.79$ eV ($E' = 120$) and the initial electron excitation peaked around the site $n_0 = N/3$. The other parameters are the same of Fig. 6.1.

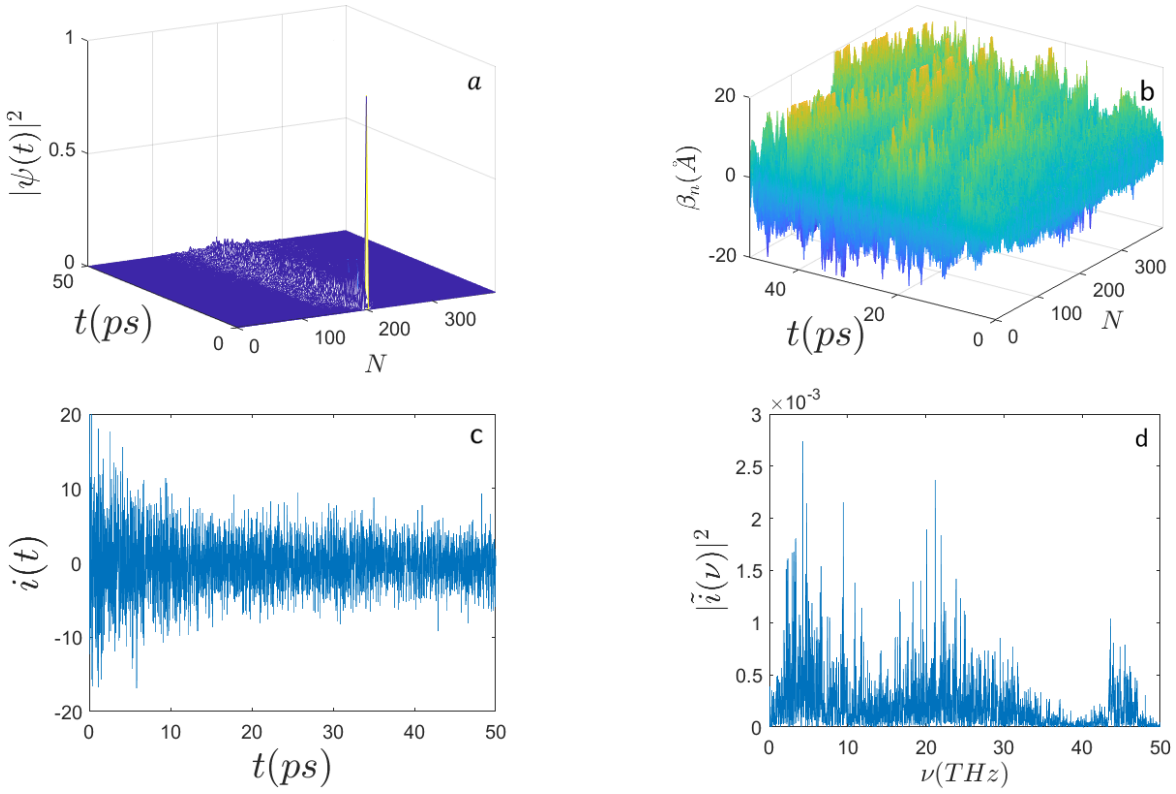


Figure 6.4 Time evolution of: a) the electron probability amplitude $|\Psi(t)|^2$; b) the average displacements $\beta_n(\mathring{A})$; c) the electron current $i(t)$ (expressed in $\mu$biot); d) the frequency spectrum $|\tilde{i}(\nu)|^2$ along the sequence of $N = 398$ nucleotides with the initial condition $E_0 = 0.46$ eV ($E' = 70$). The initial electron excitation is peaked around the site $n_0 = N/2$. The other parameters are the same of Fig. 6.1.

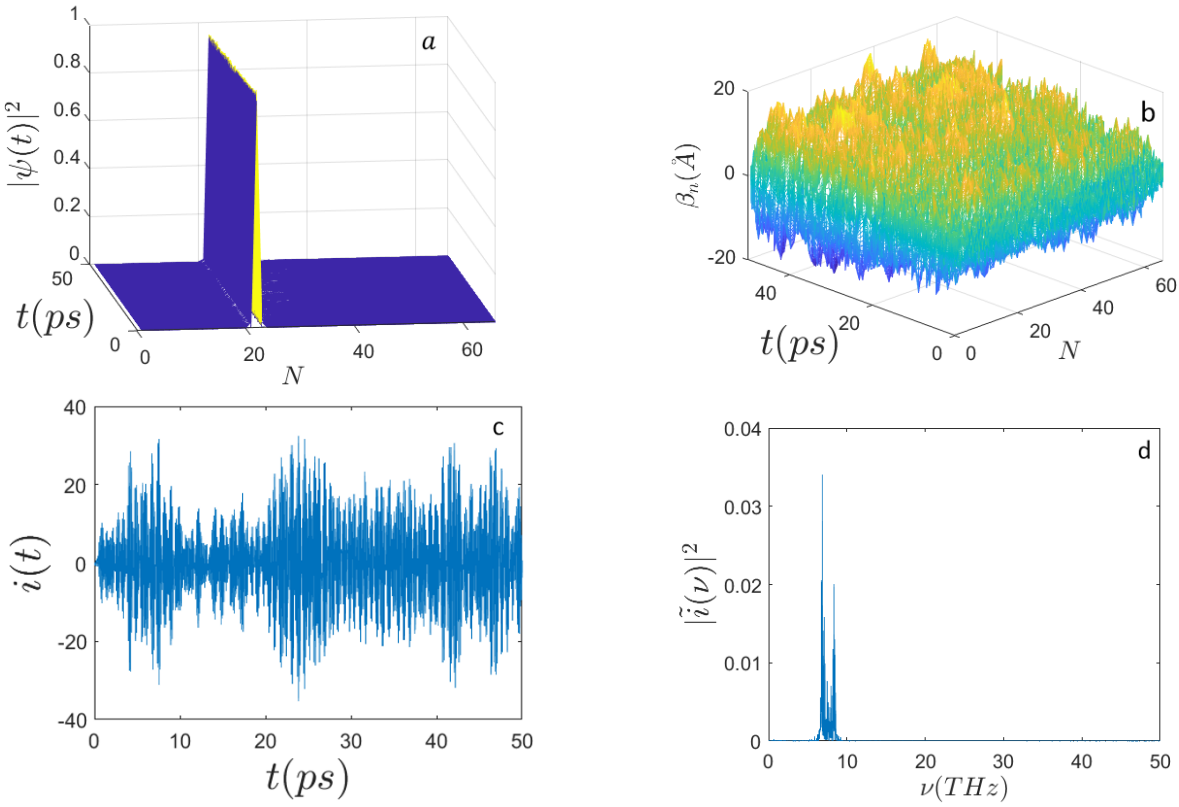


Figure 6.5 Time evolution of: a) the electron probability amplitude $|\Psi(t)|^2$; b) the average displacements $\beta_n(\AA)$; c) the electron current $i(t)$ (expressed in $\mu$biot); d) the frequency spectrum $|\tilde{i}(\nu)|^2$ along the sequence of $N = 66$ nucleotides with the initial conditions $E_0 = 0.2$ eV ($E' = 30$) and the initial electron excitation peaked around the site $n_0 = N/3$. The other parameters are the same of Fig.6.1.

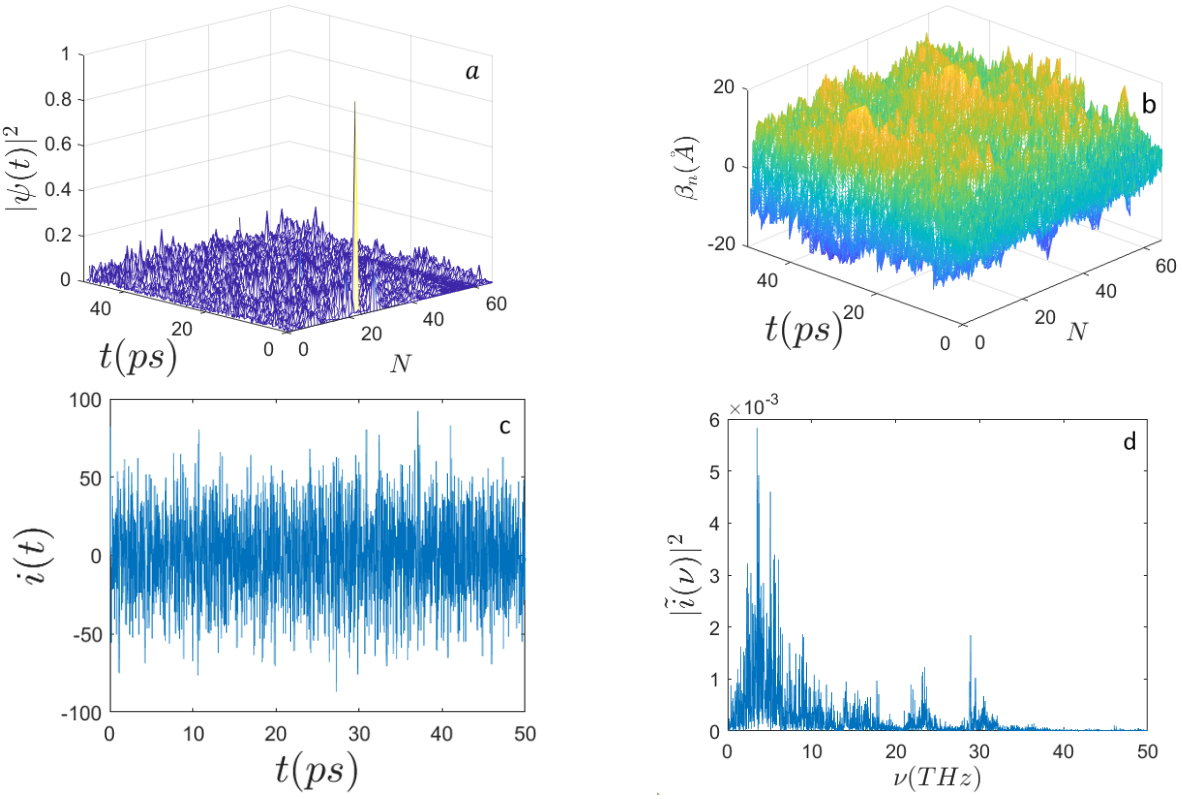


Figure 6.6 Time evolution of: a) the electron probability amplitude $|\Psi(t)|^2$; b) the average displacements $\beta_n(\mathring{A})$; c) the electron current $i(t)$ (expressed in $\mu$biot); d) the frequency spectrum $|\tilde{i}(\nu)|^2$ along the sequence of $N = 66$ nucleotides with the initial conditions $E_0 = 0.79$ eV ($E' = 120$) and the initial electron excitation peaked around the site $n_0 = N/3$. The other parameters are the same of Fig. 6.1.

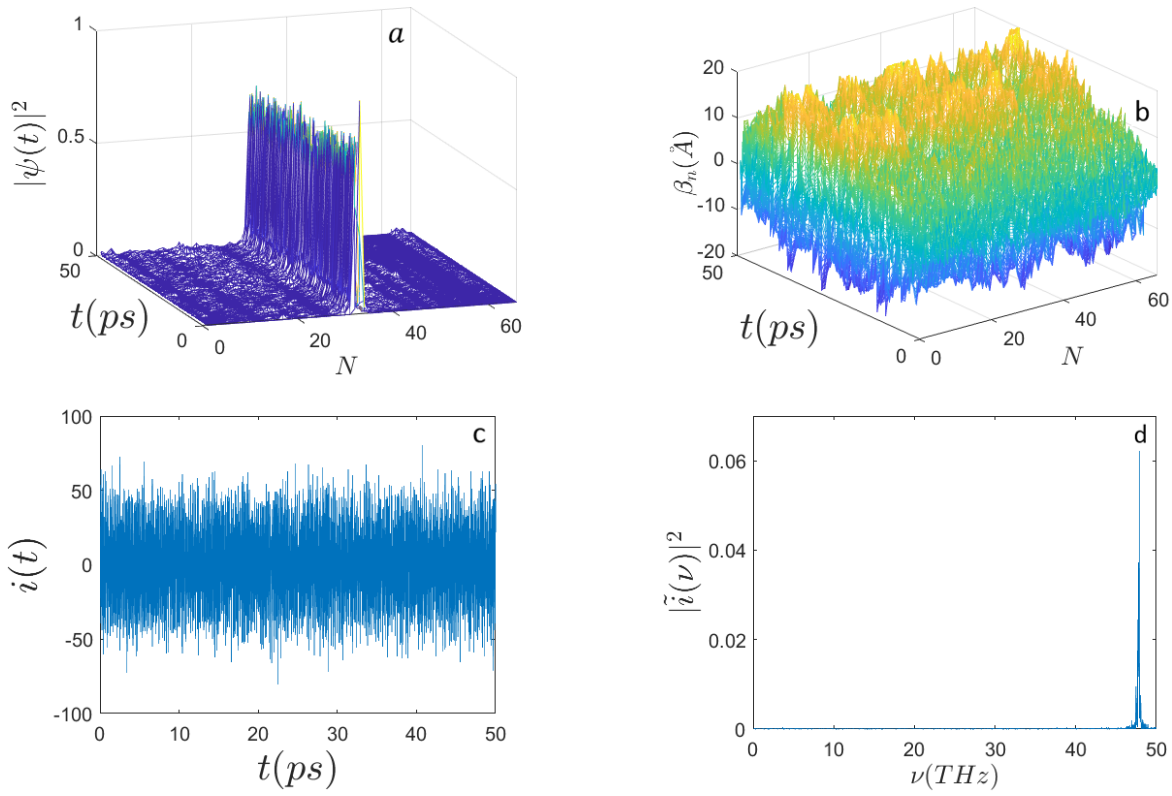


Figure 6.7 Time evolution of: a) the electron probability amplitude $|\Psi(t)|^2$; b) the average displacements $\beta_n(\AA)$; c) the electron current $i(t)$ (expressed in $\mu$biot); d) the frequency spectrum $|\tilde{i}(\nu)|^2$ along the sequence of $N = 66$ nucleotides with the initial conditions $E_0 = 0.79$ eV ($E' = 120$) and the initial electron excitation peaked around the site $n_0 = N/2$. The other parameters are the same of Fig. 6.1.

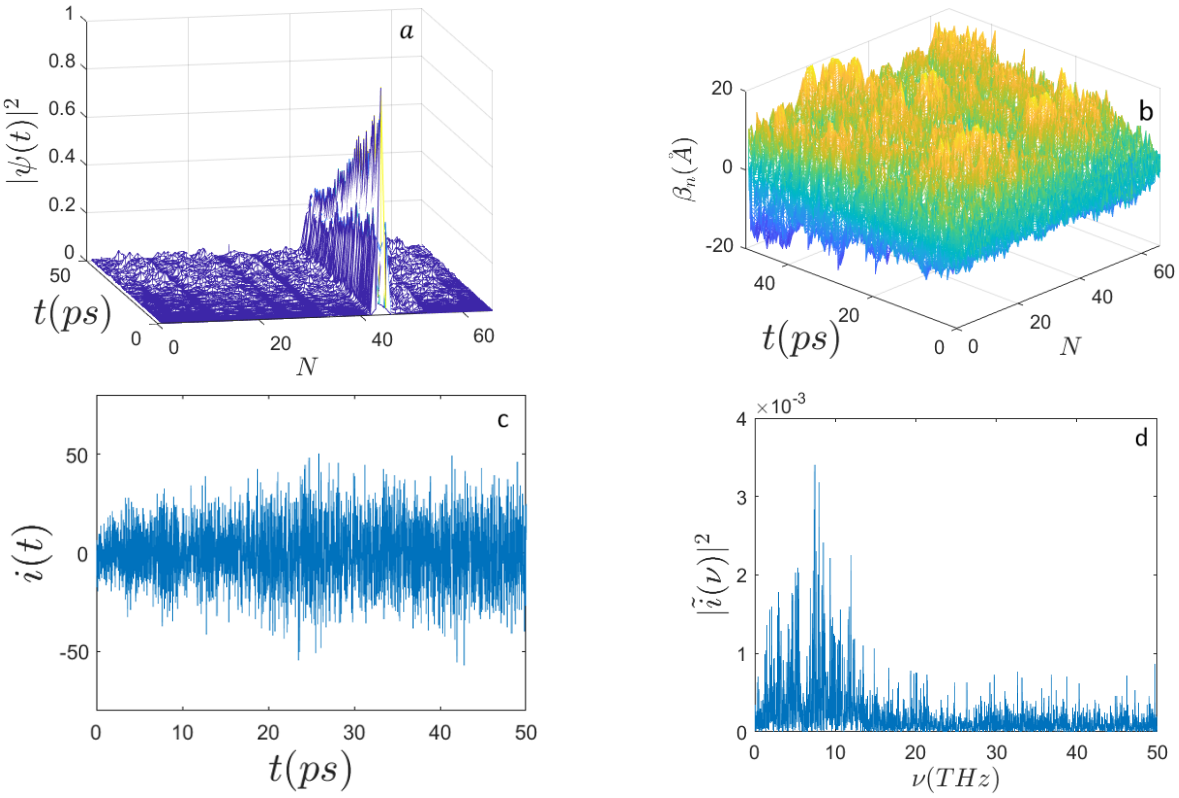


Figure 6.8 Time evolution of: a) the electron probability amplitude $|\Psi(t)|^2$; b) the average displacements $\beta_n(\AA)$; c) the electron current $i(t)$ (expressed in $\mu$biot); d) the frequency spectrum $|\tilde{i}(\nu)|^2$ along the sequence of $N = 66$ nucleotides with the initial conditions $E_0 = 0.9$ eV ($E' = 136.7$) and the initial electron excitation peaked around the site $n_0 = 2N/3$. The other parameters are the same of Fig. 6.1.

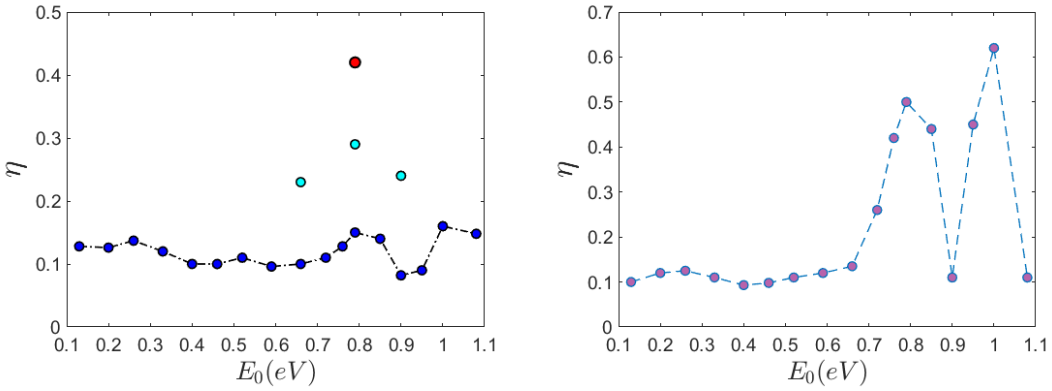


Figure 6.9 The normalized spectral entropy $\eta$ versus the initial energy $E_0$ for a DNA protein. The parameters are the same of those reported for Fig. 6.1. The left panel refers to $N = 398$ bp where the dark blue circles correspond to the initial electron excitation peaked around the site $n_0 = N/2$, the light blue circles correspond to $n_0 = N/3$, and the red circle correspond to $n_0 = 2N/3$. The right panel refers to $N = 66$ bp and the initial electron excitation is peaked around the site $n_0 = N/2$.

pendent electron-phonon coupling constants. The sequence of values of these coupling constants follows the sequence of nucleotides along a given DNA segment. Also the sequence of probabilities of electron jumping from one site to the next one depends on the specific sequence of nucleotides. In so doing a rich phenomenology is found. Instead of observing the propagation of a standard Davydov electro-soliton, depending on the initial excitation energy, we have observed localized periodic motions of the electrons - giving rise to a narrow frequency spectrum of the electron current - or, depending on the initial excitation site, to more extended motions associated with a broad noisy frequency spectrum. In both cases, the relevant spectral range belongs to the THz frequency domain. A qualitatively similar phenomenology has been found by tackling two different DNA molecules, a subunit of the haemoglobin molecule (HBB) and an oligonucleotide with a specific recognition site of a restriction enzyme. Our findings suggest that the activation of periodic currents on specific sites could be at the origin of attractive forces between the DNA and a specific effector (transcription factor, enhancer, inhibitor, and so on). The prospective developments of the this work thus concern a new investigation/explanation of the physical grounds of the RRM explained in section (4.3) by looking for co-resonances in the current frequency spectra of biochemical reaction partners. Moreover, electromagnetic signaling from electronic currents flowing along a DNA strand, and DNA response to externally applied electromagnetic fields could be further investigated in the light of the approach proposed in the present work.

# CHAPTER 7. Electrodynamic forces driving DNA-enzyme interaction at a large distance

In the previous chapter, the interesting phenomenon concerned the narrow frequency spectrum of the electron current flowing along DNA has impressed us to see if we can find a physical concept behind RRM (4.3). To this end, we have firstly applied the digital signal analysis method RRM to the interacting DNA with EcoRI restriction endonuclease enzyme, which cleaves DNA into two fragments at or near specific subsequence of DNA known as restriction/recognition sites. The two strands of 66 bp DNA sequences with cleavage sites on the sequence as well as EcoRI enzyme (276 residues) are presented in Appendix C. The outcome of this RRM is surprising with very well peak co-resonance frequency spectrum shown in Fig. (7.1) indicating resonant energy transfer between interacting macromolecules. These interactions are highly selective and this selectivity is relevant to their biological function. It is also checked and found that, indeed, both DNA strands have the same frequency distribution.

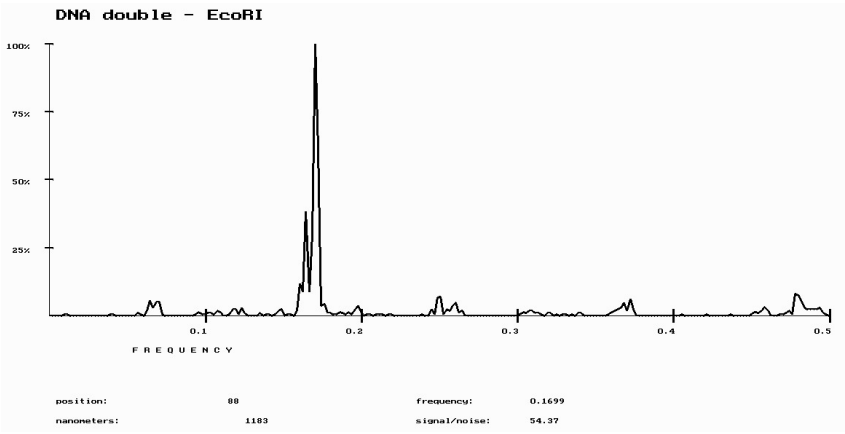


Figure 7.1 Digital RRM displays the cross spectrum frequency of the DNA-EcoRI interactions with the specific restriction sites.

It is predicted that these energies might be electrodynamic in nature. Within a quantum mechanical framework, an electron transfer along some- essentially one dimensional - substrate

is described by means of the probability current $j(x,t)$ of the electron wave function $\psi(t)$ as

$$j(x,t) = \frac{e\hbar}{2m_e i}\Big(\psi^*\nabla\psi - \psi\nabla\psi^*\Big) \tag{7.1}$$

which, according to the D'Alambert equation $\partial^\mu\partial_\mu\vec{A}(t) = \mu_0 e\vec{j}(x,t)$, can generate an electromagnetic field of components

$$\begin{aligned}\vec{E}(t) &= -\frac{\partial\vec{A}(t)}{\partial t}\\ \vec{B}(t) &= \vec{\nabla}\times\vec{A}(t)\ .\end{aligned} \tag{7.2}$$

Then, the effect of the currents flowing along two macromolecules DNA and EcoRI enzyme (1 and 2, respectively) can be that of generating an intermolecular force of electrodynamic kind given by the formula

$$\vec{F}_{12}(t) = -\frac{i_1(t)i_2(t)}{c^2}\oint\oint\frac{(d\vec{l}_1\cdot d\vec{l}_2)\vec{x}_{12}}{|\vec{x}_{12}|^3} \tag{7.3}$$

where the double integral is a geometric form factor, and the currents $i_{1,2}(t)$ are given by the mean values

$$i_{1,2}(t) = \frac{1}{l_{1,2}}\int_0^{l_{1,2}} dx\vec{j}_{1,2}(x,t) \tag{7.4}$$

where $l_{1,2}$ stand for the linearized lengths of molecules 1 and 2, respectively. According to the spectral properties of these currents, and in particular in case of presence of co-resonances in their cross frequency spectrum $\tilde{i}_1^*(\omega)\tilde{i}_2(\omega)$, the interaction force in Eq. (7.3) could attain a strength of possible relevance in a biological context. Another possibility to activate these selective interactions might be also due to water-mediated correlations in DNA-Enzyme interactions reported in [47].

Moreover, another dramatic phenomenology found by RRM is the specificity of the cleavage 6 bp ( restriction sites). In other words, the RRM shows that the sharp co-resonance weakens by substituting some base-pairs recognized by EcoRI, displayed in Fig. (7.2).

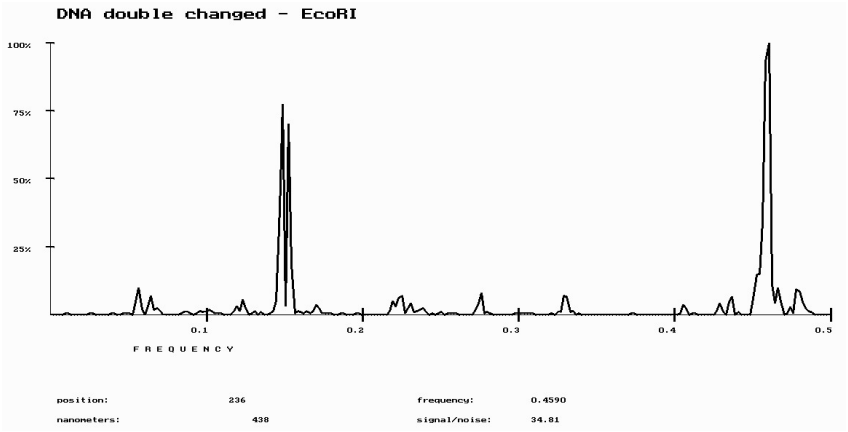


Figure 7.2 Digital RRM displays the cross spectrum frequency of the DNA-EcoRI interactions with the 6 bp as restriction sites are changed.

The aim of this chapter is an effort to explain, theoretically, the logic behind this digital RRM of the DNA-EcoRI enzyme interactions in biochemical reactions.

## 7.1 Definition of the model and its solution

In the previous chapter we found a rich phenomenology of intermolecular interactions of DNA molecules under the action of an external source of energy. Depending on the initial electron excitation site and excitation energy, we saw the concentrated periodic motions of the electrons arising a well-peaked frequency spectrum of the electron current to the motions with a spread noisy frequency spectrum. This motivated us strongly to interpret RRM with the aid of an explicit modeling of the electronic motions along the backbones of interacting DNA-protein biomolecules. To this end we use, separately for both EcoRI and DNA strand containing the CTTAAG cleavage site, the same model Hamiltonian introduced in the previous chapter (6.1) resulting in the equation of the motion (6.13) which is

$$\begin{aligned} i\hbar\dot{C}_n &= \Big(E_0 + 2\epsilon|C_n|^2 + \chi_n(\beta_{n+1} - \beta_n)\Big)C_n + J_nC_{n+1} + J_{n-1}C_{n-1}, \\ M_n\ddot{\beta}_n &= \Omega_n\beta_{n+1} + \Omega_{n-1}\beta_{n-1} - \Omega_{n-1}\beta_n - \Omega_n\beta_n + \chi_n|C_n|^2 - \chi_{n-1}|C_{n-1}|^2 \\ &+ \mu\Big((\beta_{n+1} - \beta_n)^3 - (\beta_n - \beta_{n-1})^3\Big). \end{aligned} \tag{7.5}$$

Here, for the sequence of EcoRI amino acids or DNA nucleotides, the parameter $E_0$ implies the initial bare excitation energy of the electron moving along the chain and the parameter $J_n$ is

site-dependent tunneling term of electron across two nearest neighboring sites. $M_n$ is the mass of the $n$-th amino acid/nucleotide and the coupling term $\Omega_n$ denotes the site-dependent spring parameter of two neighboring sites. The parameter $\chi_n$ is also the electron-phonon coupling dependent of the $n$-th site.

## 7.2 Physical parameters for the numerical computations

We need to determine the physical and authentic values of the coupling parameters of the Hamiltonian to do our numerical simulations. In so doing, we borrow the quantities from Ref.[60, 61] of the potential interaction energies between an electron and each of all the amino acids reported in Table (4.1) as well as the potential energies of the interaction between an electron with each of four nucleotides presented in Table (4.2). The electron in motion with the initial energy $E_0$, during its route, experiences a periodic sequence of square potential barriers of different height and of the same width $a$ -the average distance between two nearest neighboring sites- by tunneling across the chain of amino acids constituting a protein or the sequence of nucleotides composing DNA. Such a distance is $a = 4.5A^\circ$ and $a = 3.4A^\circ$ respectively in EcoRI enzyme and DNA fragment. Then separately for EcoRI enzyme and DNA, we can estimate roughly the electron tunneling term as $J_n = E_0 T_{n,n+1}$ by introducing the transmission coefficient $T_{n,n+1}$ from the probability $P(n \to n \pm 1)$ of tunneling from one potential barrier to the nearest one as follows

- Case 1: $E_0 < E_{n+1}$

$$T_{n,n+1} = \left[1 + \frac{E_{n+1}^2 \sinh^2(\beta_{n+1} a)}{4E_0(E_{n+1} - E_0)}\right]^{-1}, \tag{7.6}$$

  where $\beta_{n+1} = [2m_e(E_{n+1} - E_0)/\hbar^2]^{1/2}$.

- Case 2: $E_0 > E_{n+1}$

$$T_{n,n+1} = \left[1 + \frac{E_{n+1}^2 \sin^2(\beta_{n+1} a)}{4E_0(E_0 - E_{n+1})}\right]^{-1}, \tag{7.7}$$

in which $\beta_{n+1} = [2m_e(E_0 - E_{n+1})/\hbar^2]^{1/2}$. Moreover, we set the same site-dependent electron-phonon coupling (6.16), i.e. $\chi_n = dE/dx = (E_{n+1} - E_n)/a$.

Then we consider the same dimensionless Hamiltonian (6.17) and equations of the motion (6.18) and do the same numerical integration (6.25) and (6.26). The sound speed of amino acids is $V \sim 4$ Km/s from [18, 78] and of nucleotides is $V = 1.69$ Km/s from [76] (neglecting small

local variations due to the different masses of the amino acids or the nucleotides). We apply different analyzes for computing the spring parameter in our simulations. First, we consider the known speed of sound $V = a(\Omega_n/M_n)^{1/2}$ leading to the constant dimensionless parameter $\Omega' = V^2/a^2\omega^2$ from (6.19) where $\Omega' = 0.79$ for amino acids and $\Omega' = 0.25$ for nucleotides. Second, from [18] we borrow the spring constant of amino acids $\Omega = 18.3$ N/m giving us from (6.19) the site-dependent dimensionless $\Omega'_n = 1.83/m_n$. Third, we assume the average spring constant $\Omega = V^2\langle M\rangle/a^2$- in which $\langle M\rangle$ is the average masses of the nucleotides- and acquire the dimensionless site-dependent parameter $\Omega'_n = 0.48/m_n$ for nucleotides. The expression $m_n$ represents the dimensionless mass of amino acids and nucleotides.

To define the initial conditions of the system, we also assume the same condition (6.27) where electron is initially excited at $t = 0$ in the site $n = n_0$ with velocity $v = 0$ and same prescription (6.28) showing thermalization of macromolecules at room temperature $T = 310^\circ$ K.

## 7.3 Results

We have used an integration time step $\Delta t = 5 \times 10^{-6}$ to work out our numerical simulations with a very good energy conservation and the typical relative error $\Delta E/E = 10^{-6}$. The following analyses have reported the spectral properties of electron currents in the interaction of a DNA fragment of $N = 66$ nucleotides and an EcoRI restriction enzyme of $N = 276$ amino acids for the different initial activation energies of electron $E_0$, the various initial excitation sites of electron $n_0$ of the amplitude probability (6.27) and the distinct forms of the spring term $\Omega_n$. We study the Fourier spectrum of the electron current activated on a segment of DNA and also DNA-interacting enzyme, separately and, from now on, use the index 1 and 2 for all the terms of DNA and EcoRI, respectively. Resorting to the standard probability current $j(x_i, t)$ in (6.29), the average electron current flowing, respectively, along the DNA fragment and EcoRI enzyme macromolecules in (7.4), in a discretized version for the numerical estimation, is found

$$\begin{aligned} i_{1,2}(t) &= \frac{e\hbar}{2N_{1,2}a_{1,2}m_e i} \\ &\times \sum_{j=1}^{N_{1,2}} \Big( \Psi^*_{1,2}(x_j,t)\frac{\Psi_{1,2}(x_{j+1},t) - \Psi_{1,2}(x_{j-1},t)}{2} \\ &- \Psi_{1,2}(x_j,t)\frac{\Psi^*_{1,2}(x_{j+1},t) - \Psi^*_{1,2}(x_{j-1},t)}{2}\Big), \end{aligned} \tag{7.8}$$

where $i_{1,2}$ are the currents flowing along the DNA fragment and EcoRI enzyme macromolecules, respectively. In Figures. (7.3),(7.4),(7.5), and (7.6), we have plotted the cross Fourier spectrum of the currents $\tilde{i}_1^*(\nu)\tilde{i}_2(\nu)$ of DNA containing the sites CTTAAG recognized by the enzyme EcoRI and studied whether they are specific sites, which has a fundamental role in the DNA-protein interaction. Fig. (7.3) shows the behavior of the system when the excited electron of DNA biomolecule has the initial energy $E_{1,0} = 0.72$ eV centered in the excitation site $n_{1,0} = N/2$ while in the restriction enzyme, the initial energy of electron excitation is $E_{2,0} = 0.2$ eV localized at $n_{2,0} = N/3$. Besides, as we discussed already in section (7.2), we consider the dimensionless expressions of the site-dependent phononic spring $\Omega'_{1,n} = 0.48/m_n$ for the nucleotides and the constant term $\Omega'_2 = 0.79$ for the amino acids. In panel (a) we see very interesting phenomenon of well co-resonance around 20 THz by considering the specific CTTAAG restriction sites in almost analogue with the peak found by RRM of Fig. (7.1). Another significant finding shown in panel (b) is that the cross spectrum becomes completely spread when the recognition sites are randomly chosen AGCTTA. Moreover, in panel (c) when we exchange just one nucleotide of the restriction sites with its own complementary as CATAAG, the co-resonancy undergoes a little alterations and becomes almost broad by changing two nucleotides of the recognition sites in the form of GTTAAC presented in panel (d). In Fig. (7.4) we assume the same initial and physical condition of Fig. (7.3) and evaluate the cross frequency spectrum with other substitution of the restriction sites where the panel $a$ is the same in both figures. Here in panel (b), we can also see the broadness completely of the spectrum by considering the random recognition sites TCATGA and destroying the co-resonance spectrum by changing the only one nucleotide as CTTAAC in panel (c) and substituting two nucleotides as CATATG in panel (d). The panel (c) of Fig. (7.3) exhibits more wideness in comparison with the panel (c) of Fig. (7.4) because of the energy differences of the chosen nucleotides supposed to be recognized by EcoRI ( see Table (4.1)).

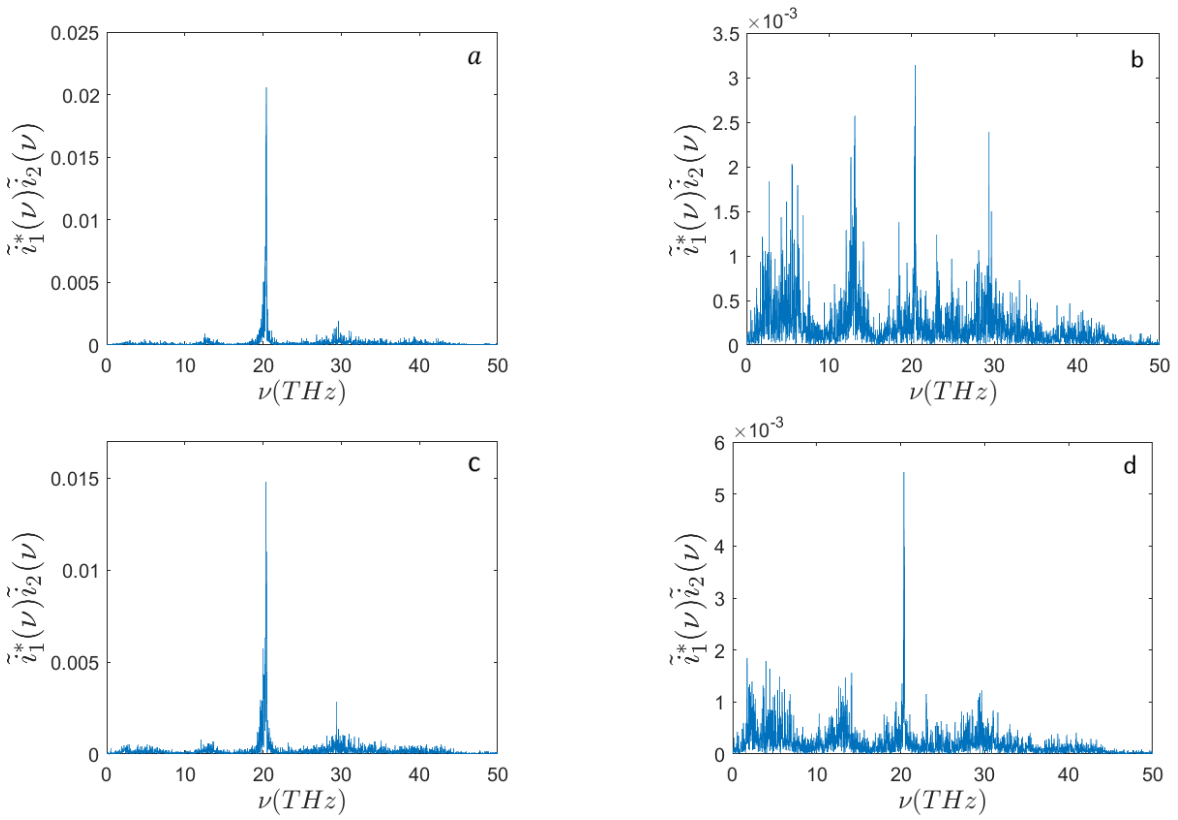


Figure 7.3 The cross frequency spectrum of the interaction between DNA strand with $N_1 = 66$ nucleotides and the EcoRI enzyme with $N_2 = 276$ amino acids for the initial conditions: $T = 310^\circ K$, $N_{0,1} = N/2$, $N_{0,2} = N/3$, $E'_{1,0} = 110$, $E'_{2,0} = 30$, $\epsilon'_1 = \epsilon'_2 = 5$, $\mu'_1 = \mu'_2 = 0.5$, $\Omega'_2 = 0.79$ and site-dependent parameters $\Omega_{1,n} = 0.48/m_n$, $J'_{1,n}$, $J'_{2,n}$, $\chi'_{1,n}$ and $\chi'_{2,n}$ corresponding to $E_{0,1} = 0.72$ eV, $E_{0,2} = 0.2$ eV, $\epsilon_1 = \epsilon_2 = 0.0329$ eV, $\mu_1 = \mu_2 = 0.5$, $\Omega_{2,n} = V^2\langle M\rangle/a^2$, $\Omega_{1,n} = V^2 M_n/a^2$, $J_{1,n}$, $J_{2,n}$, $\chi_{1,n}$ and $\chi_{2,n}$ regarding to the Equations (7.6) and (7.7); and $\sigma_{1,0} = \sigma_{2,0} = 0.1$. a) DNA containing the specific CTTAAG recognition sites, b) randomized restriction sites AGCTTA, c) exchanging only one nucleotide with its complementary CATAAG, d) exchanging two nucleotides with their complementaries GTTAAC. The frequency $\omega$ is measured in $10^{13}\mathrm{s}^{-1}$.

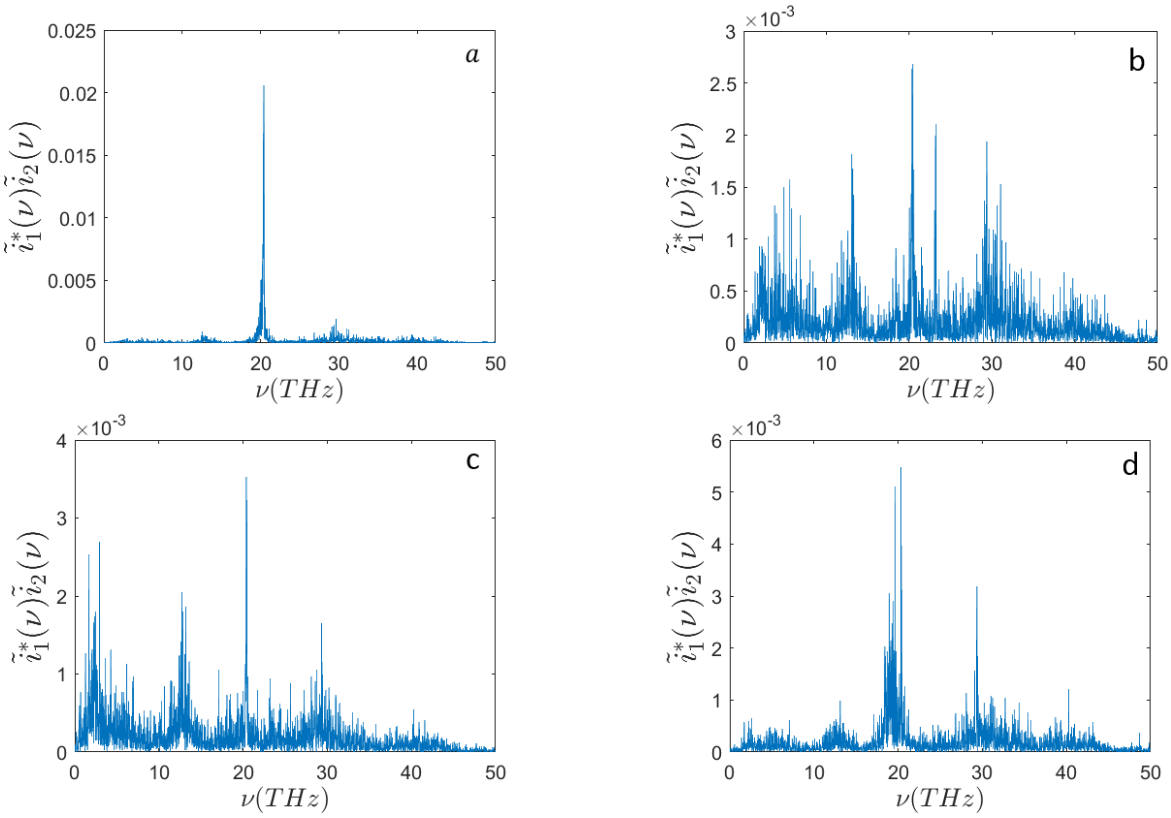


Figure 7.4 The cross frequency spectrum of the DNA-EcoRI interaction. Initial conditions and parameters are the same as those for Fig. (7.3). a) DNA containing the specific CTTAAG recognition sites (the same plot of the panel (a) in Fig. (7.3)), b) The randomized restriction sites TCATGA, c) exchanging only one nucleotide with its complementary CTTAAC, d) exchanging two nucleotides with their complementaries CATATG. The frequency $\omega$ is measured in $10^{13}\mathrm{s}^{-1}$.

In Figure (7.5) the results are reported as numerical simulations obtained for the different initial conditions which confirm well the robustness of the phenomenology previously seen in Figures (7.3) and (7.4). Here we assume the initial electronic activation energy $E_{1,0} = 0.85$ eV posited in the site $n_{1,0} = N/2$ in DNA macromolecule and the ones in the DNA-interacting enzyme $E_{2,0} = 0.85$ eV located in $n_{2,0} = N/3$. Also, the dimensionless parameter of the spring parameter in DNA fragment is assumed constant $\Omega_1' = 0.25$ and in EcoRI enzyme is considered site-dependent $\Omega_{2,n}' = 1.83/m_n$. The sharp peak of co-resonant spectrum of the DNA-EcoRI interaction with the characteristic site restriction sites CTTAAG depicted in panel $(a)$ happens around 29 THz broad entirely by choosing the randomized recognition sites

TCATGA exhibited in panel (b). It is clear in panel (c) that the sharp frequency spectrum ramifies very little by exchanging only one nucleotide of the sites, cleaved by EcoRI, with its complementary as CTTATG and destroys a bit more when two nucleotides are exchanged with their complementary sites as CTATAG seen in panel (d). Fig. (7.6) shows the same initial condition of (7.5) but with the different substitution of recognition sites. The panel (a) of two figures are the same. Taking the randomized sites AGATCT in the panel (b) of Fig. (7.6), broads the co-resonance spectrum while changing one nucleotide considered as CATAAG in panel (c) do not get spread. Finally, substituting two sites as CATAAC in panel (d) broads well.

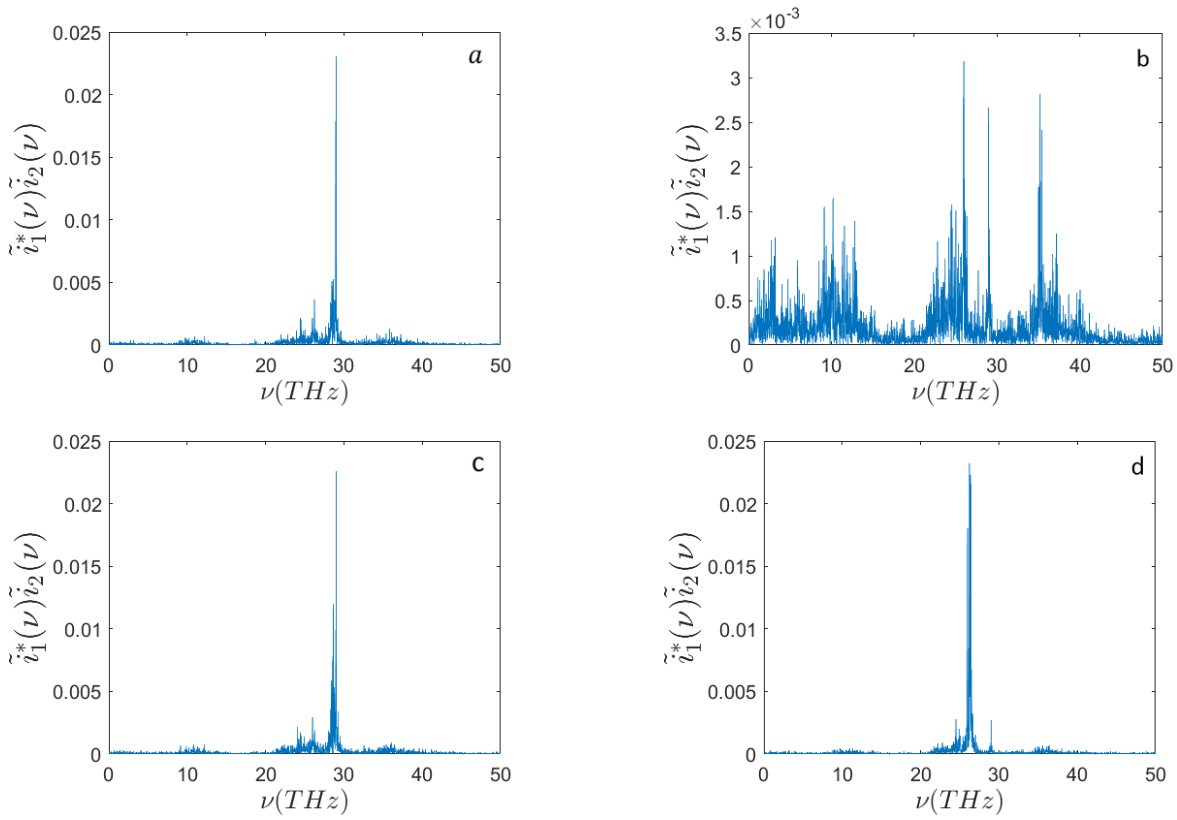


Figure 7.5 The cross frequency spectrum of the interaction between DNA strand with $N_1 = 66$ nucleotides and the EcoRI enzyme with $N_2 = 276$ amino acids for the initial conditions: $N_{0,1} = N/2$, $N_{0,2} = N/3$, $E'_{1,0} = E'_{2,0} = 129.17$, $\Omega'_{1,n} = 0.25$, $\Omega'_{2,n} = 1.83/m_n$ corresponding to $E_{1,0} = E_{2,0} = 0.85$ eV, $\Omega_{1,n} = V^2 M_n/a^2$ and $\Omega_2 = 18.3$ N/m. The other parameters are the same as Figure (7.3); a) DNA containing the specific recognition sites CTTAAG, b) randomized restriction sites TCATGA, c) exchanging only one nucleotide with its complementary site CTTATG, d) exchanging two nucleotides with their complementaries CTATAG. The frequency $\omega$ is measured in $10^{13}\mathrm{s}^{-1}$.

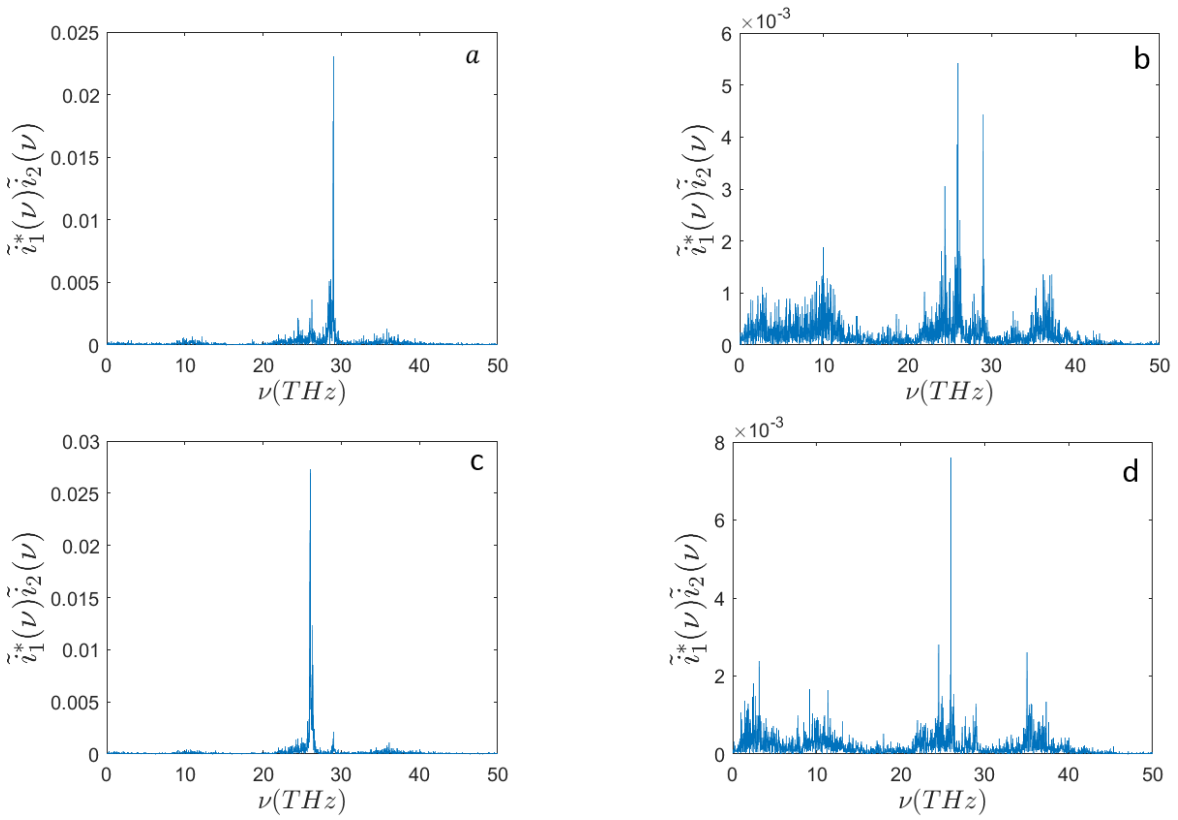


Figure 7.6 The cross frequency spectrum of the DNA-EcoRI interaction. Initial conditions and parameters are the same as those for Fig. (7.5). a) DNA containing the specific recognition sites CTTAAG (the same plot of the panel (a) in Fig. (7.5)), b) randomized restriction sites AGATCT, c) exchanging only one nucleotide with its complementary site CATAAG, d) exchanging two nucleotides with their complementaries CATAAC. The frequency $\omega$ is measured in $10^{13}\mathrm{s}^{-1}$.

## 7.4 Water-mediated correlations at long range in DNA-enzyme interactions

As we mentioned in the introduction of this chapter, the above noticeable sharp co-resonance of frequency spectrum might be resulted from the EDFs calculated by (7.3) using (7.8); however, our calculations are found to be very small values. Nevertheless, we can resort to the dynamic polarization which develops in the water field and mediates long-range correlation between DNA and enzyme [47]. A dipole wave field mediates the molecular interaction between DNA and enzyme in water due to the electric dipoles in the molecular interaction under study (see Fig. 7.7). Such a field results from the coupled dipoles of the aromatic ring structures in DNA and in enzyme. in the quantum field theory (QFT) formalism it is shown that these

electric dipole networks exhibit characteristic collective mode frequencies and that the dynamic time-average polarization vanishes in the water just if one or both fields of DNA and enzyme are absent.

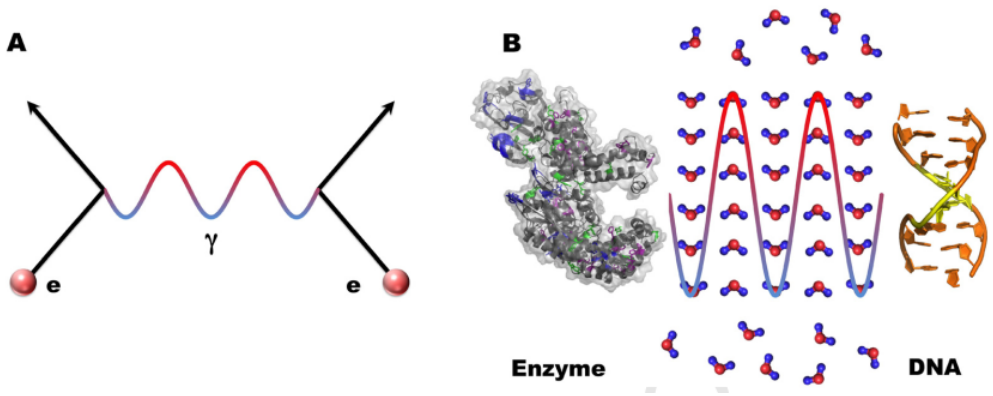


Figure 7.7 Adopted by [47]. Mediating wave fields or quanta in subatomic and biological physics. (A) Electron-electron correlations are mediated by photons in quantum field theory.(B) Analogously, long-range correlation in the molecular water field between DNA and enzyme may be mediated by dipole waves. Note that theses are schematic rendering, neither drawn to scale nor respective of the actual orientations of water molecules.

Intriguing connections exist between the model presented in this chapter, which describe electronic motions along a given DNA sequence, and the coordinated electronic fluctuations that arise from van der Waals many-body dispersion forces [47, 79, 80, 81] in a variety of molecular contexts. Specifically, productive insights have emerged from attempts to unify atomistic, continuum, and mean-field treatments in the quantum electronic behaviors of DNA and proteins in water [47, 81, 82, 83, 84]. Even in the presence of thermally turbulent aqueous environments, it has been shown that these collective electronic dispersion correlations can persist at several nanometers from the protein-water interface, and these correlations are energetically relevant for protein folding processes at the microsecond scale [83], and likely for even longer times *in vivo*.

Kurian and coworkers [47, 79] have additionally shown that

- such collective electronic modes are suitably fine-tuned for the synchronized catalysis of two phosphodiester bonds ($\sim 0.46$ eV);

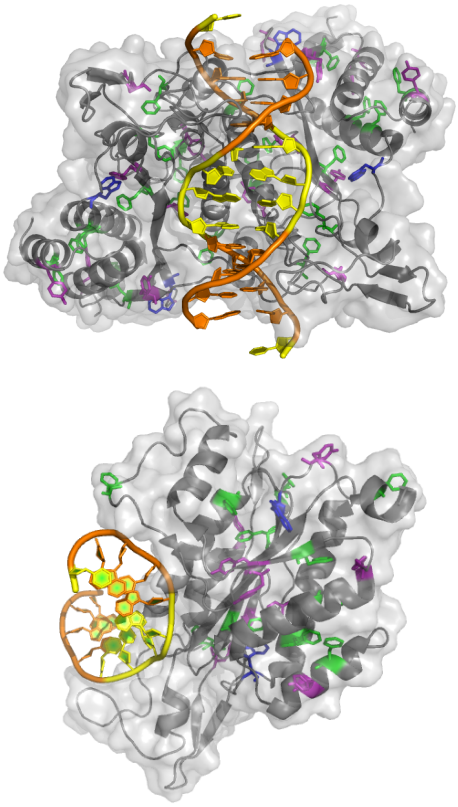

Figure 7.8 Aromatic network in *Eco*RI-DNA complex. Tryptophan (blue), tyrosine (purple), and phenylalanine (green) form correlated electronic dispersion networks in *Eco*RI, shown here in the top panel bound to its double-stranded DNA substrate, with adenine-thymine (yellow) and cytosine-guanine (orange) base pairs highlighted. Other amino acids (gray) are displayed in the context of their secondary structures within the enzyme, and in the bottom panel only one of the two *Eco*RI dimers is shown for clarity, to showcase the $\pi - \pi$ stacking of the DNA bases. Image of *Eco*RI (PDB ID: 1CKQ) at 1.85 Å resolution created with PyMOL and adapted from [47].

- the palindromic mirror symmetry of the double-stranded DNA target sequence recognized by the enzyme (see Figure 7.8) allows for conservation of parity in the symmetric, site-specific cleavage of both DNA strands;

- by considering the radiative field created by the collective electronic fluctuation modes in the DNA target sequence, a nonvanishing polarization emerges spontaneously in the orientational correlations of the water dipole network;

- the strength of the coupling $\Omega$ between the radiative field and the water molecular rotational levels scales with the water density $\rho$ as $\Omega \propto \sqrt{\rho}$, thus varying with temperature and pressure;

- the spontaneous breakdown of phase symmetry generates a field pattern (in the so-called "limit cycle" regime) that preserves gauge invariance by the dynamical emergence of coherence between the matter field (DNA, water, enzyme) and the electromagnetic field (radiative field from DNA, water, enzyme);

- the resulting interaction energy is between $\sim 0.1 - 1$ eV, populating bands in the infrared spectrum between $0 < \nu < 1000\,\mathrm{cm}^{-1}$, which overlaps with the energy scale of the collective electronic fluctuation modes in the DNA target sequence and in the enzyme but remains distinct from the more energetic intramolecular vibrations and purely electronic transitions of water;

- the interaction between the emergent water polarization field and the enzyme radiative field can be written in the form of a Jaynes-Cummings-like Hamiltonian $\mathcal{H}$ that scales with the number of water molecules $N$ as $\mathcal{H} \propto \hbar\Gamma\sqrt{N}$, which for sufficiently large $N$—consider the number of water molecules in a domain encompassed by the infrared wavelengths above ($\sim 10 - 100\,\mu$m)—provides a protective gap against thermalization ($k_B T \approx 0.02$ eV at physiological temperatures) for these long-range correlations; and

- the collective electronic fluctuation modes in the $0.1 - 1$ eV range do not couple to the rotational quantum transitions of individual water molecules (meV scale), bur rather to the emergent polarization modes present in the collective dipole network, with peak maxima for liquid water completely within this range.

Chiral sum frequency generation spectroscopy experiments [85] have demonstrated the existence of a chiral water superstructure surrounding DNA under ambient conditions, thereby confirming that the chiral structure of DNA can be imprinted electrodynamically on the surrounding solvent. These experiments have also shown that some sequence-specific fine structure persists in this chiral spine of hydration, providing a mediating context for DNA target sequence recognition by the enzyme.

In this chapter, we have shown a co-resonance in the frequency spectra of the electronic currents moving on the DNA and on the enzyme, respectively, in the interacting system DNA-EcoRI. Another intriguing result is the disappearance of this co-resonance when the subsequence of nucleotides- which is recognized by the enzyme to cleave the DNA- is randomized. These

interesting outcomes are similar to the findings of RRM, meaning that our suggestive modified electron-phonon interacting model by considering site-dependent electron tunneling term and site-dependent electron-phonon coupling may be a justification behind RRM. Then due to the nature of long-range correlations between DNA and enzyme in water, in QFT formalism, we can calculate the intermolecular forces of DNA-EcoRI interaction. This job is under investigation.

# CHAPTER 8. Conclusions

We have studied generalization of Davydov's model with a second quantization Hamiltonian for investigating quantum energy and information transfer of a single excitation electron in electron-phonon interactions in biochemical reactions. This work has been motivated by lack of a physical concept behind RRM predicting the selective DNA-protein interactions relevant to their biological functions in biochemical reactions. There are theoretical and experimental evidence of long-range electrodynamic interactions taking place between biomolecules so that deterministic and selective forces acting at a long distance could accelerate the encounter between cognate partners of biochemical reactions. There are theoretical prediction that the electrodynamic potential due to selective interactions at long distances is proportional to $r^{-6}$ if the electric dipoles of the molecules vibrate out of resonance, but in the resonant condition is proportional to $r^{-3}$.

Referred to the Davydovs model [18], we have started considering a biomolecule as a spin network (without environment/phonons) with N atoms ($n \in \{0, ..., N-1\}$ ) and three channels recognized by $\alpha = 1, 2, 3$, and studying the electronic information transfer in this network. Of course, this phenomenon is strongly dependent on the initial conditions assumed for electron. In so doing, by assuming an initial condition for the electron, we have evaluated the behavior of ITF and found the attainability of maximum fidelity between two spins happens just for the lattice with no more than two atoms. However, we were curious if we could find analytical attainability for the system with $N$ atoms by changing the initial conditions of electron. we have studied numerically ITF of our system and found for both cases, ITF is higher when the input and the output nodes are in the same channel $\alpha$ or in the same molecule $n$. For $N$ even ITF is high around 0.9 whereas this amount is about 0.5 when $N$ is odd. This is because for $N$ even, when the input and the output nodes are in the same channel, ITF is higher when these nodes are diametrically opposed. For N odd such reasoning can not be applied and so ITF is lower. Another conclusion is that the larger $J/L$ ( the proportion of the coupling between molecules

to the couping between channels), the higher ITF for the transfers on the same channel and equivalently, the smaller $J/L$ the higher ITF for the transmissions on the other channels at the first short time after interaction.

Then, moving on to a more realistic model we have studied [23] we have studied electron energy transfer in biomolecules resulting in the interesting phenomenologies through light pumping. In the first case, we have focused on a protein by modifying the Davydov's model as presence of nonlinear terms in both the electron and phonon sectors in the Hamiltonian. This study was motivated by the problem left open in recent work [21] and activation of phonon condensation. We have shown the energy transfer from electronic excitation into phonon excitation is the logic behind quantum Bose-like Fröhlich condensation. More investigation has indicated the faster this energy transfer happens with the larger electron-phonon coupling constant. Also the nonlinear electron-electron term has shown effective role for decaying of electron energy. Moreover, we have seen the dispersion of electron probability amplitude everywhere throughout the molecular chain even in room temperature whereas that was observed in enough high temperature in Davidov's soliton.

Inspiring from the previous model, we have assumed the electron tunneling term and electron-phonon coupling parameters dependent on the site in a DNA (see [24]). The values of this sequence are relevant to the energy of the delocalized electron of each particular nucleotides. Our motivation to do this work was the investigation the spectral properties of an electron moving along a DNA fragment. To this end, we have considered two different sequences, one haemoglobin molecule (HBB) with a long sequence (398bp) and oligonucleotide with a shorter sequence (66bp). Then with respect of our previous model, by doing Fourier frequency spectra of the electronic current concerned RRM, we have observed the quantum currents have the both localized periodic behavior resulting in a sharp peak of Fourier frequency spectrum or random motions giving rise to a broad frequency spectrum. This interesting outcomes concerned the narrow frequency spectrum could be an explanation for the selective EDfs in biochemical reactions.

Motivated by the intriguing outcomes mentioned above in a DNA, by the digital signal analysis method (RRM) we have obtained the co-resonances of the oligonucleotide (66 bp) and a restriction enzyme EcoRI (276 amino acids), which recognizes and binds to a subsequence

of DNA and cleaves it,and found very good results with very well peak frequency spectrum. This has motivated us to provide a physical explanation of the phenomenological RRM by our electron-phonon interacting model. In so doing, we have studied the quantum co-resonance phenomenon suggested by RRM of the electronic currents along the oligonucleotide and EcoRI where, surprisingly our findings, concerned the different initial electronic excitation conditions, have shown a sharp peak of DFT similar to the outcomes of digital RRM. Moreover, we have chosen the random substitution of the 6 base pairs recognized by EcoRI and seen the peak of co-spectrum disappears. This indicates also very interesting quantum phenomenology of the specificity of the cleavage 6 bp sequence.

All in all, in this thesis work we have studied the information and energy transfer in biomolecules. We could present the physical explanation behind quantum phonon condensation by releasing the electron energy to the phonons activating long-range, resonant and selective EDFs in biomolecules. Moreover, we have provided a physical model describing RRM anticipating that this might open many new research lines to extend what we have here reported to other biochemical reactions in biological systems. The prospective application of this thesis work may understand the action of EMFs on uncontrolled mitosis in cancer cells due to the fact that there is a vast literature about healing effects of EMFs on cancer cells but no theoretical explanation is available [86, 87] and could possibly give perspective toward the development of quantum information protocols for driven, non-equilibrium model biosystems. Moreover, more developments could be inspiring full quantum investigations of the energy and information transfer efficiency of excited electrons in the biomolecules antennas subsequently transferred to a reaction center and studying the geometry and curvature of biomolecules which could help scientists to improve their knowledge of quantum technologies in life science and quantum information devices operating in the biomolecules [88, 89].

## A. Gene sequence (398 bp) coding for one of the $\beta$ subunits of the haemoglobin molecule (HBB)

CGGCTGTCATCACTTAGACCTCACCCTGTGGAGCCACACCCTAGGGTT
GGCCAATCTACTCCCAGGAGCAGGG AGGGCAGGAGCCAGGGCTGGGCATAAA
AGTCAGGGCAGAGCCATCTATTGCTTACATTTGCTTCTGACACAACTGTGTTCACT
AGCAACCTCAAACAGACACCATGGTGCATCTGACTCCTGTGGAGAAGTCTGCCGT
TACTGCCCTGTGGGGCAAGGTGAACGTGGATGAAGTTGGTGGTGAGGCCCTGGG
CAGGTTGGTATCAAGGTTACAAGACAGGTTTAAGGAGACCAATAGAAACTGGGCAT
GTGGAGACAGAGAAGACTCTTGGGTTTCTGATAGGCACTGACTCTCTCTGCCTATT
GGTCTATTTTCCCACCCTTAG

## B. Sequence of an oligonucleotide (66 bp) containing a cleavage subsequence of the EcoRI enzyme

TACCGATTACTGGCTCTTATCCCTAGGCTTAAGTTATAACCATGGATGCCCGAAA
CGCGAGCATAG

## C. Chain of amino acids of the EcoRI enzyme

SNKKQSNRLTEQHKLSQGVIGIFGDYAKAHDLAVGEVSKLVKKALSNEYPQLS
FRYRDSIKKTEINEALKKIDPDLGGTLFVSNSSIKPDGGIVEVKDDYGEWRVV
LVAEAKHQGKDIINIRNGLLVGKRGDQDLMAAGNAIERSHKNISEIANFMLSE
SHFPYVLFLEGSNFLTENISITRPDGRVVNLEYNSGILNRLDRLTAANYGMPI
NSNLCINKFVNHKDKSIMLQAASIYTQGDGREWDSKIMFEIMFDISTTSLRVL
GRDLFEQLTSK

### C.1 DNA strands and restriction sites recognized by EcoRI

## Bibliography

[1] T. Ichimura, and M. Nuriya, *Symposium report: understanding biological systems with quantum science and technology*, Biophysical reviews **12**, 287-289 (2020).

[2] P. Ball, *Physics of life: The dawn of quantum biology* Nature News **474**, 272-274 (2011).

[3] M. Mohseni, P. Rebentrost, S. Lloyd, and A. Aspuru-Guzik, *Environment-assisted quantum walks in energy transfer of photosynthetic complexes*, J. Chem. Phys. **129**, 174106 (2008).

[4] F. Caruso, A. W. Chin, A. Datta, S. F. Huelga and M. B. Plenio, *Entanglement and entangling power of the dynamics in light-harvesting complexes*, Phys. Rev. A **81**, 062346 (2010).

[5] S. G. Engel, T. R. Calhoun, E. L. Read, T-K Ahn, T. Mancal, Y-C Cheng, R. E. Blankenship and G. R. Fleming, *Evidence for wavelike energy transfer through quantum coherence in photosynthetic systems*, Nature **446**, 782-786 (2007).

[6] M. B. Plenio and S. F. Huelga, *Dephasing-assisted transport: quantum networks and biomolecules. New Journal of Physics*, **10**, 113019 (2008).

[7] E. M. Gauger, E. Rieper, J. J. Morton, S. C. Benjamin and V. Vedral, *Sustained quantum coherence and entanglement in the avian compass*, Phys. rev. lett. **106**, 040503 (2011).

[8] C. J. Murphy, M. A. Arkin, Y. Jenkins, N. D. Ghatlia, S. Bossman, N. J. Turro, and J. K. Barton, *Long-range photoinduced electron transfer through a DNA helix*, Science **262**, 1025 - 1029 (1993).

[9] Y. A. Berlin, A. L. Burin, and M. A. Ratner, *On the long-range charge transfer in DNA*, J. Phys. Chem. **104**, 443 - 445 (2000).

[10] C. Wan, T. Fiebig, O. Schiemann, J. K. Barton, and A. H. Zewail, *Femtosecond direct observation of charge transfer between bases in DNA*, Proc. Natl. Acad. Sci. USA **97**, 14052 - 14055 (2000).

[11] S. Delaney, and J. K. Barton, *Long-range DNA charge transport*, J. Org. Chem. **68**, 6475 - 6483 (2003).

[12] H. Fröhlich, H. Pelzer and S. Zienau, *Properties of slow electrons in polar materials. The London, Edinburgh, and Dublin Philosophical Magazine and Journal of Science*, **41**, 221-242 (1950).

[13] T. D. Lee, F. E. Low, and D. Pines, *The motion of slow electrons in a polar crystal*, Physical Review **90**, 297 (1953).

[14] T. Holstein, *Studies of polaron motion: Part I. The molecular-crystal model*, Annals of physics **8**, 325-342 (1959).

[15] F. Marsiglio, *Pairing and charge-density-wave correlations in the Holstein model at half-filling* Phys. Rev. B **42**, 2416 (1990).

[16] A. S. Davydov, *Solitons in molecular systems*, Springer-Science+Business Media, B.V. (1985).

[17] A. S. *Davydov Solitons in molecular systems*, Physica Scripta **20**, 387 (1979).

[18] A. Scott, *Davydov's soliton*, Physics Reports **217**, 1-67 (1992).

[19] H. Fröhlich, *Long-range coherence and energy storage in biological systems*, Int. J. Quantum Chem. **2**, 641-649 (1968).

[20] Fröhlich, *Long-range coherence in biological systems*, Riv. Nuovo Cimento **7**, 399-418 (1977).

[21] I. Nardecchia, J. Torres, M. Lechelon, V. Giliberti, M. Ortolani, P. Nouvel, M. Gori, Y. Meriguet, I. Donato, J. Preto, L. Varani, J. Sturgis, and M. Pettini, *Out-of-Equilibrium Collective Oscillation as Phonon Condensation in a Model Protein*, Phys. Rev. X **8**, 031061 (2018).

[22] J. Preto, M. Pettini, and J. A. Tuszynski, *Possible Role of Electrodynamic Interactions in Long-Distance Biomolecular Recognition*, Phys. Rev. E **91**, 052710 (2015).

[23] E. Faraji, R. Franzosi, S. Mancini and M. Pettini, *Energy transfer to the phonons of a macromolecule through light pumping*, Scientific Reports **11** 1-14 (2021).

[24] E. Faraji, R. Franzosi, S. Mancini and M. Pettini, *Transition between random and periodic electron currents on a DNA chain*, Int. J. Mol. Sci. **22**, 7361 (2021).

[25] M. A. Nielsen and I. L. Chuang. *Quantum computation and quantum information*, Cambridge University Press, Cambridge (2010).

[26] D. Hennig, *Mobile polaron solutions and nonlinear electron transfer in helical protein models*, Phys. Rev. E **64**, 041908 (2001).

[27] L. D. Landau, *Electron motion in crystal lattices*, Phys. Z. Sowjet. **3**, 664 (1933).

[28] S. Pekar, *Local quantum states of electrons in an ideal ion crystal*, Journ. of Phys. USSR **10**, 341 (1946).

[29] M. Pettini and M. Landolfi, *Relaxation properties and ergodicity breaking in nonlinear Hamiltonian dynamics*, Phys. Rev. A **41**, 768 (1990).

[30] A. S. Davydov, *The theory of contraction of proteins under their excitation*, J. theor. Biol. **38** 559-569 (1973).

[31] A. S. Davydov, *Solitons and energy transfer along protein molecules*, J. theor. Biol. **66** 379-387 (1977).

[32] D. D. Georgiev, and J. F. Glazebrook. *On the quantum dynamics of Davydov solitons in protein -helices*, Physica A **517**, 257-269 (2019).

[33] P. Kramer, *A review of the time-dependent variational principle*, J. Phys.: Conf. Series **99**, 012009 (2008).

[34] D. A. Lidar, *Lecture notes on the theory of open quantum systems*, arXiv:1902.00967 (2019).

[35] A. S. Davydov, *The role of solitons in the energy and electron transfer in one-dimensional molecular systems*, Physica D: Nonlinear Phenomena **3**, 1-22 (1981).

[36] S. Bose, *Quantum communication through spin chain dynamics: an introductory overview*, Contemporary Physics **48**, 13-30 (2007).

[37] M. Rafiee, C. Lupo and S. Mancini, *Noise to lubricate qubit transfer in a spin network*, Phys. Rev. A **88**, 032325 (2013).

[38] R. Jozsa, *Fidelity for mixed quantum states*, Journal of modern optics **41**, 2315-2323 (1994).

[39] E. Jonckheere, F. C. Langbein and S. G. Schirmer, *Information transfer fidelity in spin networks and ring-based quantum routers*, Quantum Inf. Process. **14**, 4751-4785 (2015).

[40] B. J. Olson, S. W. Shaw, C. Shi, C. Pierre and R. G. Parker, *Circulant matrices and their application to vibration analysis*, Applied Mechanics Reviews **66**, 040803 (2014).

[41] M. J. Grill, W. A. Wall, and C. Meier. *A computational model for molecular interactions between curved slender fibers undergoing large 3D deformations with a focus on electrostatic, van der Waals, and repulsive steric forces*, Int. J. Numer. Methods Eng. **121**, 22852330 (2020).

[42] P. J. W. Debye., *Molekularkrafte und ihre elektrische deutung*, Hirzel, (1921).

[43] R. Eisenschitz, and F. London. *ber das Verhltnis der van der Waalsschen Krfte zu den homopolaren Bindungskrften*, Zeitschrift fr Physik **60**, 491-527 (1930).

[44] F. London, *The general theory of molecular forces*, Trans. Faraday Soc., **33** 8b-26, (1937).

[45] H. B. Casimir, and D. Polder, *The influence of retardation on the London-van der Waals forces*, Phys. Rev. *73*, 360 (1948).

[46] P. Debye, Peter, and E. Hckel, *De la theorie des electrolytes. I. abaissement du point de congelation et phenomenes associes*, Physikalische Zeitschrift **24**, 185-206 (1923).

[47] P. Kurian, A. Capolupo, T.J.A. Craddock, G. Vitiello, *Water-mediated correlations in DNA-enzyme interactions*, Phys. Lett. A **382**, 33 - 43, (2018).

[48] J. R. de Xammar Oro, G. Ruderman, J. R. Grigera and F. Vericatg, *Threshold frequency for the ionic screening of electric fields in electrolyte solutions*, J. Chem. Soc. Faraday Trans. **88**, 699-703, (1992).

[49] J. D. Jackson. *Classical Electrodynamics, 3rd Ed*, American Journal of Physics **67** 841 (1999).

[50] W. J. Ellison, *Permittivity of pure water, at standard atmospheric pressure, over the frequency range 0-25 THz and the temperature range 0-100 C*○, J. Phys. Chem. Ref. Data **36**, 1-18 (2007).

[51] M. J. Stephen, *FirstOrder Dispersion Forces*, J. Chem. Phys. **40**, 669-673 (1964).

[52] A. D. McLachlan, *Resonance transfer of molecular excitation energy*, Mol. Phys. **8**, 409-423 (1964).

[53] P. C. Painter, L. E. Mosher, and C. Rhoads, *Lowfrequency modes in the Raman spectra of proteins*, Biopolymers **21**, 1469-1472 (1982).

[54] K. C. Chou, *Low-frequency motions in protein molecules. Beta-sheet and beta-barrel*, Biophys. J. **48**, 289-297 (1985).

[55] P.C. Painter, L.E. Mosher, and C. Rhoads, *Lowfrequency modes in the raman spectrum of DNA*, Biopolymers **20**, 243 (1981).

[56] H. Fröhlich, *The extraordinary dielectric properties of biological materials and the action of enzymes*, PNAS *72*, 4211-4215 (1975).

[57] A. Markelz, S. Whitmire, J. Hillebrecht and R. Birge, *THz time domain spectroscopy of biomolecular conformational modes*, PPhys. Med. Biol., **47**, 3797 (2002).

[58] T. M. Wu and S. Austin, *Bose condensation in biosystems*, Phys. Lett. A **64**, 151-152 (1977).

[59] T. M. Wu and S. Austin, *Bose-Einstein Condensation in Biological Systems*, J. Theor. Biol. **71**, 209 (1978).

[60] I. Cosic, *Macromolecular Bioactivity: Is It Resonant Interaction Between Macromolecules? - Theory and Applications*, IEEE Transact. on Biomed. Engineering **41**, 1101 (1994); I. Cosic, *The Resonant Recognition Model of Macromolecular Bioactivity: Theory and Applications*, Birkhauser Verlag, Basel, (1997).

[61] V. Veljkovic and I. Slavic, *General model of pseudopotentials*, Phys. Rev. Lett. **29**,105 - 108 (1972).

[62] V. Heine, V., and I. V. Abarenkov, *A new method for the electronic structure of metals*, Philosophical Magazine **9**, 451-465 (1964).

[63] L. Bonetta, *Interactome under construction*, Nature **468**, 851-852 (2010).

[64] Fröhlich, *Selective long range dispersion forces between large systems*, Physics Letters A **39**, 153-154 (1972).

[65] I. Nardecchia, L. Spinelli, J. Preto, M. Gori, E. Floriani, S. Jaeger, P. Ferrier, and M. Pettini, *Experimental detection of long-distance interactions between biomolecules through their diffusion behavior: Numerical study*, Phys. Rev. E **90**, 022703 (2014).

[66] I. Nardecchia, M. Lechelon, M. Gori, I. Donato, J. Preto, E. Floriani, S. Jaeger, S. Mailfert, D. Marguet, P. Ferrier, and M. Pettini, *Detection of long-range electrostatic interactions between charged molecules by means of fluorescence correlation spectroscopy*, Phys. Rev. E **96**, 022403 (2017).

[67] H. Fröhlich, *Electrons in lattice fields*, Adv. Phys. **3**, 325 - 361 (1954).

[68] T. Holstein, *Studies of polaron motion: Part I. The molecular-crystal model* , Ann. Phys. (USA) **8**, 343 - 389 (1959).

[69] R. Livi, M. Pettini, S. Ruffo, M. Sparpaglione, and A. Vulpiani, *Equipartition threshold in nonlinear large Hamiltonian systems: The Fermi-Pasta-Ulam model*, Phys. Rev. A **31**, 1039 (1985).

[70] A. Bayat, D. Burgarth, S. Mancini, and S. Bose, *Memory effects in spin-chain channels for information transmission*, Phys. Rev. **A** 77, 050306(R) (2008).

[71] D. Klotsa, R.A. Römer, and M. S. Turner, *Electronic Transport in DNA*, Biophys. J. **89**, 2187 (2005).

[72] Alberts, B., D. Bray, J. Lewis, M. Raff, K. Roberts, and J. Watson, *Molecular Biology of the Cell*, (Garland, New York, 1994).

[73] E. Boon, A. Livingston, N. Chmiel, S. David, and J. Barton, *DNA-mediated charge transport for DNA repair*, Proc. Natl. Acad. Sci. USA. **100**, 12543 - 12547 (2003).

[74] P. ONeil, and E. M. Fielden, *Primary free radical processes in DNA*, Adv. Radiat. Biol. **17**, 53-120 (1993).

[75] J. Retel, B. Hoebee, J. E. F. Braun, J. T. Lutgerink, E. Van der Akker, H. Wanamarta, H. Joenjie, and M. V. M. Lafleur, *Mutational specificity of oxidative DNA damage*, Mutat. Res. **299**, 165 (1993).

[76] M. B. Hakim, S. M. Lindsay, and J. Powell, *The speed of sound in DNA*, Biopolymers: Original Research on Biomolecules, **23**, 1185 (1984).

[77] U. Ketterling, A. Koltermann, P. Schwille, and M. Eigen, *Real-time enzyme kinetics monitored by dual-color fluorescence cross-correlation spectroscopy*, Proc. Natl. Acad. Sci. USA **95**, 14161420 (1998).

[78] L. Cruzeiro, J. Halding, P. L. Christiansen, , O. Skovgaard, O. and A. C. Scott, *Temperature effects on the Davydov soliton*, Phys. Rev. A **37**, 880 (1988).

[79] P. Kurian, G. Dunston and J. Lindesay, *How Quantum Entanglement in DNA Synchronizes Double-Strand Breakage by Type II Restriction Endonucleases*, Journal of Theoretical Biology, **391**, 102-112 (2016).

[80] J. Hermann, D. Alf and A. Tkatchenko, *Nanoscale $\pi - \pi$ Stacked Molecules Are Bound by Collective Charge Fluctuations*, Nature Communications **8**, 14052 (2017).

[81] M. Gori, M. Sthr, A. Tkatchenko and P. Kurian, *Many-body dispersion interactions among fragments in molecular complexes*, In preparation (2021).

[82] P. Kurian, *Chirality-Energy Conversion Induced by Static Magnetic Effects on Free Electrons in Quantum Field Theory*, J. Phys. Commun., **2** (2018).

[83] M. Sthr, A. Tkatchenko, *Quantum Mechanics of Proteins in Explicit Water: The Role of Plasmon-like Solute-Solvent Interactions*, Science Advances **5** (2019).

[84] P. Kurian, *Relativistic Treatment of the Energy Shifts Caused by Static Electromagnetic Effects on Free Electrons*, In submission (2021).

[85] McDermott, M. L.; Vanselous, H.; Corcelli, S. A.; Petersen, P. B. DNA's Chiral Spine of Hydration. ACS Central Science 2017, 3 (7), 708-714. https://doi.org/10.1021/acscentsci.7b00100.

[86] E. D. Kirson, V. Dbaly, F. Tovarys, J. Vymazal, J. F. Soustiel, A. Itzhaki, D. Mordechovich, S. Steinberg-Shapira, Z. Gurvich, R. Schneiderman, Y. Wasserman, M. Salzberg, B. Ryffel, D. Goldsher, E. Dekel and Y. Palti, *Alternating electric fields arrest cell proliferation in animal tumor models and human brain tumors*, PNAS **104**, 10152-10157 (2007).

[87] R. Sarimov, E. Markova, F. Johansson, D. Jenssen, and I. Belyaev1, *Exposure to ELF magnetic field tuned to Zn inhibits growth of cancer cells*, Bioelectromagnetics **26**, 631-638 (2005).

[88] S. Hameroff, *Quantum walks in brain microtubules -A biomolecular basis for quantum cognition?*, Topics in cognitive science **6**, 91-97 (2014).

[89] S. Hameroff, *How quantum brain biology can rescue conscious free will*, Frontiers in integrative neuroscience **6**, 93 (2012).